Evaluation of transport properties of cement-based materials subjected to water attack using non-destructive integrated CT-XRD method

非破壊 CT-XRD 連成法を用いた水の作用を受けたセメント系材料の輸送特性の評価

Yingyao Tan

Laboratory of Environmental Material Engineering
Division of Field Engineering for the Environment
Graduate School of Engineering
Hokkaido University
Sapporo, Japan

March 2024

DEDICATION

To
The author’s beloved family

ACKNOWLEDGEMENTS

My sincere and hearty thanks and appreciations go firstly to my supervisor, Prof. Takafumi Sugiyama, for his kindness, illuminating guidance and profound knowledge. Without his professional suggestions and constant guidance throughout my Ph. D course, this research could not have been completed. It has been a great privilege and joy to study under his guidance and supervision, which I will treasure in my whole life.

I am very grateful to members of supervising committee: Prof. Takashi Matsumoto, Prof. Kohe Nagai and Associate Prof. Katsufumi Hashimoto. Their invaluable suggestions and critical comments are crucial for improving this work.

I would like to acknowledge SPring-8, a large synchrotron radiation facility, for providing the synchrotron CT-XRD hardware that allows me to use its world leading equipment. In SPring-8, I received selfless support from other researchers. Please allow me to express my sincere gratitude to Dr. Takashi Hitomi (Obayashi Corp), Assistant Prof. of Tokyo University of Science Hayato Takahashi, Dr. Kentaro Kajiwara (Japan Synchrotron Radiation Research Institute), and their research groups for the support of the measurements in SPring-8.

Assistance from research teammates in the laboratory was extremely important to this research. Thanks to Anna Tomo, Yota Narita and Junxiao Liu, for their assistance in the experiment. May the short time of experimenting together bring eternal friendship.

To all students and staff of the Environmental Material Engineering Laboratory, Hokkaido University, thanks for your friendly and supportive atmosphere, which helped me to carry out this research in a pleasant working environment.

My thanks also goes to the Japanese Ministry of Education, Culture, Sports, Science and Technology, who provided scholarship (MEXT) during my Ph. D course. Thanks to this fund, my life in Ph. D course went smooth and could focus on study without pressure.

Finally, my warm gratitude goes to my family and friends. Love, support, and sacrifices from my parents have encouraged and guided me overcome difficulties. May they live long and healthily. The promise I made with my grandma when I was a child has always guided me towards the distance until here. May she rest in peace. The joy my friends brought to me comfort me a lot. May our friendship never end. Thank you for my girlfriend. For her absence, I can focus on my research.

ABSTRACT

Concrete is used in underground radioactive waste disposal facilities due to its stable chemical properties to fulfill the requirement of structural stability. However, these facilities are inevitably in contact with ground water for a long time, which brings the danger of concrete structure being damaged by leaching. Leaching refers to the process by which soluble compounds in the cement hydrated system are dissolved and carried away by water. This process can increase the porosity and permeability of the concrete, making it more susceptible to further leaching and the ingress of harmful substances. Therefore, it is of great significance to analyze the transport properties of concrete under the impact of long-term leaching deterioration. However, as a heterogeneous material, the different phases in concrete, including aggregates, bulk cement paste, the interfacial transition zone (ITZ) and pores, have different responses to the leaching process, which together form the picture of the leaching process of concrete. This response is firstly reflected in the change in transport of substances in different phase, that is, the change in transport properties. Although research efforts have been made on evaluating leaching deterioration in the past, quantitative analysis on transport properties considering the alteration of different phases from the microscopic point of view is still needed.

This research aims to study the alteration of cement-based materials under leaching from a microscopic perspective using non-destructive integrated CT-XRD method. Integrated CT-XRD technique using synchrotron radiation X-ray source can provide high-precision three-dimensional geometric information and phase distribution information of specimen non-destructively and simultaneously. The addition of random walk algorithm to the CT image analysis made it possible to quantify transport properties of different phases in concrete. Among them, ITZ is difficult to quantify due to its irregular and tiny geometric shape. To solve this problem, a reconstructed method of CT images in adjacent aggregate region was originally proposed, which made the transport properties analysis on ITZ possible.

In the experiments, a series of natural leaching tests under different conditions were conducted. The dissolution front of portlandite was identified, enabling to separate the leached region and non-leached region in the specimen after the leaching tests. Then, transport properties of different regions were analyzed, and corresponding diffusion coefficients of calcium ions were calculated including in the ITZ. It is found that the diffusion coefficient of calcium ion in the leached region was about 50 times larger than that of the non-leached region, while it was about 10 times larger in ITZ as compared with the non-leached region. In this way, this study successfully provided the changing diffusion coefficients in altered specimens due to leaching. The obtained results were verified by simulating with the SiTraM2D software. Using the quantitative transport properties obtained from CT-XRD method and random walk algorithm, the dissolution of portlandites in concrete after 10 years immersion was predicted. Results showed that the dissolution front ranged from 6.2 to 7.2 mm deep inward the concrete, indicating non negligible effect of ITZ. In addition, it was implied that the diffusion of Sr^{2+} ion was influenced by the carbonation as well as the portlandite dissolution.

TABLE OF CONTENTS

DEDICATION i
ACKNOWLEDGEMENTS ii
ABSTRACT iii
TABLE OF CONTENTS iv
LIST OF TABLES vii
LIST OF FIGURES viii

CHAPTER 1 INTRODUCTION 1
1.1 BACKGROUND 1
1.2 REVIEW OF RELEVANT KNOWLEDGE 3
1.2.1 Leaching process in hydrated cement paste 3
1.2.2 Characteristics of interface transition zone (ITZ) 8
1.2.3 Carbonation process 9
1.2.4 Analysis methods on cement hydrated system 10
1.3 RESEARCH OBJECTIVES 13
1.4 STRUCTURE OF THIS THESIS 14
CHAPTER 2 EXPERIMENT AND MEASUREMENT 16
2.1 GENERAL 16
2.2 SPECIMEN PREPARATION 16
2.2.1 Proportion and labeling 16
2.2.2 Molding, demolding, curing, and storing 17
2.3 LEACHING AND CARBONATION TEST 18
2.3.1 Solvent preparation 18
2.3.2 Carbonation process 19
2.3.3 Leaching process 19
2.3.4 Test procedures, overview of specimens and measurements 20
2.4 NON-DESTRUCTIVE INTEGRATED CT-XRD METHOD 21
2.4.1 Basic introduction of facility 21

2.4.2 CT measurement and image processing 23
2.4.3 Synchromatic XRD measurement and crystal phase analysis 27
2.5 OTHER MEASUREMENT METHODS 31
2.6 SUMMARY 33
CHAPTER 3 METHODOLOGY OF IMAGE PROCESSING AND RANDOM WALK SIUMULATION 34
3.1 GENERAL 34
3.2 EXTRACTION OF PORE STRUCTURE FROM CT IMAGES STACK 34
3.2.1 Images stack and ROI 34
3.2.2 Binary process 36
3.2.3 Pore cluster and labeling process 37
3.2.4 Expansion 39
3.3 TORTUOSITY CALCULATION BY RANDOM WALK ALGORITHM 40
3.4 SUMMARY 45
CHAPTER 4 STUDY OF ALTERATION OF CEMENT HYDRATED SYSTEM AND THE ROLE OF ITZ 46
4.1 GENERAL 46
4.2 EXPERIMENTAL RESULTS 46
4.2.1 CT images of each kind of specimen 46
4.2.2 Phase transition under leaching in different solvent and carbonation 51
4.2.3 Released calcium amount from specimen 60
4.3 TRANSPORT PROPERTY OF LEACHED REGION, NON-LEACHED REGION AND ITZ 64
4.3.1 Effect of ITZ on dissolution front 65
4.3.2 Image reconstruction and segmentation 67
4.3.3 Quantitative analysis of diffusion coefficient in non-carbonated specimen 71
4.3.4 Effect of carbonation on transport properties 74
4.4 SUMMARY 76
CHAPTER 5 APPLICATION OF IMAGE ANALYSIS DATA TO TRANSPORT PREDECTION 78
5.1 GENERAL 78
5.2 SIMULTANEOUS ION TRANSPORT MODEL 78

5.2.1 Diffusion of multiple ions 78
5.2.2 Pore structure and liquid-solid inter-reaction 79
5.2.3 Integrated description of SiTraM 81
5.3 EVALUATION OF CEMENT-BASED MATERIALS UNDER LEACHING 82
5.3.1 Modeling of experimental specimens 82
5.3.2 Modeling of concrete under 10 years leaching 89
5.4 STRONTIUM ION DIFFUSING IN CONCRETE DURING LEACHING 93
5.5 SUMMARY 96
CHAPTER 6 CONCLUSIONS 98
6.1 GENERAL CONCLUSION 98
6.2 RECOMMENDATIONS FOR FURTHER RESEARCH 99
6.2.1 More algorithms applicable in CT image data 99
6.2.2 Expansion and improvement of evaluated method 99
6.2.3 Alteration of concrete with supplementary cementitious material (SCM) subject to leaching 100

REFERENCE 101
Appendix A: INTERFERENCE CAUSED BY FIXED METHOD 112
Appendix B: IMPROVEMENTS OF IMAGE QUALITY 115

LIST OF TABLES

Table 1-1 Chemical formulas of components

Table 1-2 Formulas of carbonation process

Table 1-3 Volume change after transition of portlandite

Table 2-1 Chemical composition of cement

Table 2-2 Proportion of different water to cement ratio

Table 2-3 Meaning of labeling

Table 2-4 Labeling examples

Table 2-5 Ion composition in modulated seawater [100]

Table 2-6 Overview of specimens

Table 2-7 Position relationship among units in each series of measurement (mm)

Table 2-8 Detailed information of the CT measurements in this research

Table 4-1 Computed result of Ca2+ ion diffusion coefficient (cm2/s)

Table 4-2 Comparison of Ca2+ ion diffusion coefficients in previous studies

Table 5-1 Properties of intact hydrated cement paste

Table 5-2 Transport properties of sound cement paste and ITZ region

Table 5-3 Parameter selection of sound hydrated cement paste and ITZ region

Table 5-4 Parameter selection of intact mortar and ITZ region

Table 5-5 Evaluation of dissolution front (days, mm)

LIST OF FIGURES

Figure 1-1 Structure of this thesis

Figure 2-1 Schematic diagram of specimens

Figure 2-2 Container for accelerated carbonation test

Figure 2-3 Size of one specimen and bottle

Figure 2-4 Test procedures of specimens

Figure 2-5 Equipment for non-destructive integrated CT-XRD method

Figure 2-6 Schematic diagram of the system for non-destructive integrated CT-XRD method

Figure 2-7 Generation of sinogram

Figure 2-8 Reconstruction process and stack of reconstructed images

Figure 2-9 Data form of reconstructed image (32 - bit)

Figure 2-10 Histogram and conversion of 32 - bit image to 8 - bit image

Figure 2-11 Data form of reconstructed image (8 - bit)

Figure 2-12 Detected region in XRD measurement

Figure 2-13 Intensity-Energy relationship (detected pattern)

Figure 2-14 Transformation from energy scale to 2θ angle scale

Figure 2-15 XRD detected pattern after transferring into 2θ angle scale.

Figure 2-16 Solvent exchange and ICP-OES measurement

Figure 2-17 Powder XRD measurement and TG-DTA measurement

Figure 3-1 CT image of 5N0d specimen (layer 0720)

Figure 3-2 Extraction of VOI (200 × 200 × 200 voxels)

Figure 3-3 Gray scale value histogram of VOI and corresponding porosity curve

Figure 3-4 Three-dimensional effect diagram of binary image

Figure 3-5 Isolated pore in extracted pore structure (2D, layer 0720)

Figure 3-6 Division of pore cluster in two dimensions

Figure 3-7 Pore cluster labeling process and extraction of largest pore cluster in three dimensions

Figure 3-8 Schematic diagram of expanding ROI by flipping

Figure 3-9 Expanded pore structure in three dimensions

Figure 3-10 Flow diagram of random walk simulation

Figure 3-11 Trajectory of single walker in free space (M = 10000)

Figure 3-12 Euclidean distance and shortest path in lattice

Figure 3-13 Trajectory of walkers ($N = 100$, M = 10000)

Figure 3-14 MSD of walkers at different steps for free space and pore structure

Figure 4-1 Test procedure of non-carbonated plain specimens leaching in pure water

Figure 4-2 CT image of specimens with w/c=0.6, under pure water leaching

Figure 4-3 CT image of specimens with w/c=0.5, under pure water leaching
Figure 4-4 Test procedure of single aggregate containing specimens
Figure 4-5 CT image of 5LN20c and 5LN80c specimens
Figure 4-6 Test procedure of carbonated specimens
Figure 4-7 CT image of carbonated specimens with w/c = 0.6
Figure 4-8 Test produce of specimens leaching in modulated seawater
Figure 4-9 CT image of 5LN20c specimen (layer: 0720)
Figure 4-10 Line profile of labeled line a - b
Figure 4-11 XRD data of 5LN20c specimen
Figure 4-12 Dissolution front for non-carbonated specimen after 60 days leaching (6N60d specimen)
Figure 4-13 CT-XRD result of 6N0d specimen
Figure 4-14 CT-XRD result of 6C0d specimen
Figure 4-15 Powder XRD data of specimens with or without carbonation before leaching test (6N0d and 6C0d)
Figure 4-16 CT-XRD result of non-carbonated specimen after 21 days seawater immersion (S6N21d)
Figure 4-17 CT-XRD result of non-carbonated specimen after 147 days seawater immersion (S6N147d)
Figure 4-18 Powder XRD result of S6N147d specimen
Figure 4-19 TG-DTA curve of specimen without leaching (6N0d)
Figure 4-20 TG-DTA curve of specimen after 21 days leaching in seawater (S6N21d)
Figure 4-21 Image at the edge of S6N147d
Figure 4-22 XRD data of non-carbonated specimen after 147 days seawater immersion (S6N147d) (point 1)
Figure 4-23 Dissolution front of 6N60d specimen
Figure 4-24 Dissolution fronts of specimens with different leaching period
Figure 4-25 Equivalent depth of dissolution front of non-carbonated specimen with different leaching periods
Figure 4-26 Equivalent dissolution front in 3 dimensions
Figure 4-27 Accumulated released calcium per volume with different leaching periods
Figure 4-28 Accumulated released calcium per volume after 120 days of leaching period
Figure 4-29 CT-XRD result for 6C120d
Figure 4-30 Dissolution front of different slices of 5LN20c
Figure 4-31 Dissolution front of different slices of 5LN80c
Figure 4-32 Schematic of reconstruction in one single slice
Figure 4-33 Extraction of strip ROI
Figure 4-34 Extraction of aggregate part in strip ROI
Figure 4-35 Reconstruction of selected ROI and VOI
Figure 4-36 Segmentation of sub-VOIs
Figure 4-37 Striped ROIs selection of 5LN20c and 5LN80c
Figure 4-38 Output of MSD-time relationship in an extended sub-VOI

Figure 4-39 Computed diffusion coefficient of Ca2+ ion in each specimen
Figure 4-40 CT image and VOIs selection of 6N0d, 6C0d and 6C120d
Figure 4-41 VOI A in 6C0d and corresponding pore structure
Figure 4-42 Diffusion coefficient of VOIs in 6C120d
Figure 4-43 Diffusion coefficient comparison between 6C0d and 6C120d
Figure 5-1 Dissolution equilibrium of hydrated cement paste (portlandite and C-S-H gel system)
Figure 5-2 Discretization and modelling of diffusion in one dimension
Figure 5-3 Simultaneous ion transport model (SiTraM)
Figure 5-4 Discretization and modelling of plain cement paste under leaching
Figure 5-5 Sampling on 5N0d specimen and corresponding porosity
Figure 5-6 Simulation result of portlandite concentration in solid phase for 5N and 6N specimens
Figure 5-7 Comparison of dissolution front depth between simulation and CT images
Figure 5-8 CT image of 6LN60d
Figure 5-9 Extraction of VOIs
Figure 5-10 Extraction of pore structure and preforming random walk simulation
Figure 5-11 Discretization of 6LN60d
Figure 5-12 Comparison of dissolution front of portlandite in simulation and actual experiment
Figure 5-13 Discretization of concrete section
Figure 5-14 Result of portlandite concentration in solid phase at different leaching period in concrete
Figure 5-15 Progress of dissolution front near aggregate
Figure 5-16 Progress of dissolution front in bulk mortar and under effect of ITZ
Figure 5-17 Modeling of leaching and strontium ion diffusion occurring simultaneously
Figure 5-18 $1/\tau$-ρ relationship from Random walk simulation
Figure 5-19 Schematic diagram of calculation
Figure 5-20 Concentration of Sr^{2+} ion after 10 years exposure

CHAPTER 1 INTRODUCTION

1.1 BACKGROUND

Concrete is fundamental materials for construction all over the world. It is estimated that the present consumption of concrete in the world is around 14 billion cubic meters in 2020, which the secondary massive resource consumed by human civilization after water [1]. Because of its low cost, high plasticity and well durability, cement-based materials will still be the most widely used construction materials in human society in the foreseeable future. Huge number and various types of concrete structures serve differently in various places in human society, which makes the deterioration of concrete under different environments unavoidable research topic.

Deterioration of concrete closely related to concrete's functions and exposed environment. An extreme use case for concrete is structure of underground disposal for nuclear waste. Nuclear power supplies over 14% of the world's electricity requirements, which is strategically and quantitatively an important contributor to global electricity generation capacity. While providing low-carbon, huge amount and sustainable energy, nuclear power also produces a small amount of longer-lived radioactive waste. Besides, since nuclear energy was applied, there have been several major accidents, like Three Mile Island accident (1979), Chernobyl disaster (1986) and Fukushima disaster (2011), in which large amount of radioactive substance was generated. In addition, activities such as radiotherapy in medical institutions and flaw detection in the industrial sector also continue to produce radioactive waste. All these radioactive substances require careful management. Underground storage in disposal until radioactive material decays below safety requirements is currently the most widely accepted treatment method [2]. Depending on the half-life of different radioactive elements, these disposals can be used for hundreds to thousands of years. Concrete materials used in disposal structure has special requirements for its durability in face of underground environment and super-long design life.

Water attack of concrete is assumed to rarely become an issue for structure in general use. However, it's an important phenomenon for underground nuclear waste disposal due to the existence of ground water seepage and the long service life of the structure. Water attack can impact the structural integrity of the disposal facility, which can erode containment barriers or liners and compromise the facility's ability to isolate waste from the surrounding environment. This can result in the escape of hazardous materials. During hundreds or even over one thousands of years of service life, ground water will continuously remove the components inside concrete, resulting porosity increase and decomposition of concrete [3][4][5]. This process is generally summarized as leaching process of concrete. When concrete materials no longer meet the permeability designed requirements of disposal under the deterioration of leaching, the radioactive waste inside disposal will be at risk of leakage.

Hydrated cement paste in concrete dissolves more easily than aggregate, which makes leaching deterioration happens in hydrated cement paste. Hydrated cement paste degradation by leaching can be divided into two parts: 1) Dissolution process of hydrated cement constituents into pore solution; and 2) Diffusion process of the species

in pore solution to external environments [6]. Physicochemical reaction speed of dissolution is higher than diffusion, which makes speed of leaching process generally control by diffusion process [7]. Dissolution, diffusion, pore structure and permeability of concrete are interrelated and affect each other in leaching process. The dissolution of components from hydrated cement paste into pore solutions and their diffusion from pore solutions to the external environment continuously increases the porosity and permeability of hardened cement, which in turn affects the diffusion and dissolution process. Dissolution of hydrated cement paste is depending on the relative solubility of each hydrate. The portlandite (CH) contained in cement paste is the first mineral to be completely dissolved, then followed by the progressive decalcification of C-S-H gel over time [8][9]. Leaching of cement-based materials is a time-consuming process, and thus many previous studies have used acids to accelerate the process to shorten the research cycle [10][11]. However, it inevitably changes the leaching behavior, so natural leaching test is still indispensable.

As a heterogeneous material, the multi-phase characteristics of concrete itself also affect the leaching process. According to the difference in chemical and physical properties, concrete materials are first divided into aggregate phase and phase of bulk cement paste. With the deepening of research, the transition region between bulk cement paste and aggregate surface is divided into the third phase, that is the interface transition zone (ITZ). The importance of the ITZ in concrete has long been known by researchers. Due to the presence of aggregate surfaces, the packing of grains is disrupted to give a zone of higher porosity and smaller grains in the zone close to the aggregate. Because of the way it is formed, the ITZ is not a definite zone, but a region of transition. Its effective thickness varies with the microstructural feature being studied and during the course of hydration. Due to its more porous structure, ITZ plays an important role in the failure process of concrete and has been the focus of research in the past. On the other hand, due to its small-scale characteristic, it has always been a difficulty in research. The effect of ITZ on mechanical property of concrete had been widely studied [12][13]. Some researchers have further analyzed the impact of ITZ on overall mechanical properties under leaching [14]. However, effect of ITZ on leaching and assessment of structural durability based on this remains little study. Aggregates in concrete generally do not participate in the leaching process, but the ITZ formed between aggregates and hydrated cement has relatedly higher porosity and permeability, which can affect the leaching process. Due to the porous structure of ITZ, transport path along the ITZ may be formed in the long-term leaching process of concrete, which will accelerate the leaching deterioration towards to the interior of concrete and lead to failure of the disposal.

Under the continuous interaction with the surrounding strata, the composition of groundwater will greatly differ from pure water. Besides, in the process of handling nuclear accidents, seawater is sometimes injected into reactor as a means of cooling the core. The above situation shows that the leaching process of concrete does not always occur in pure water, and ions components in leachate also need to be considered [15]. On the other hand, the leaching process is also affected by the high temperature due to geothermal heat geothermal heat [16].

Traditionally, carbonation is considered as a problem that long-term service concrete must face [17][18]. Generally, the reaction of gaseous carbon dioxide with calcium-bearing phase in concrete infrastructure components is known to cause a lowing of alkalinity, leading to depassivation and corrosion of rebars. However,

in recent years, carbonation of plain concrete has been considered as an effective method to reduce carbon dioxide emissions in the cement industry [19][20][21]. In the future, carbonated cement-based materials are likely to appear more widely in various engineering constructure, which require us to conduct research on leaching behavior of carbonated cement-based materials. In the leaching process of concrete, the role of carbonation is not negative [22][23]. The effect of carbonation on the leaching process is an interesting and worthwhile question. On the one hand, carbonization will transform the components with high solubility in concrete into low-solubility components; on the other hand, the carbonation can reduce the porosity of concrete to a certain extent and reduce its permeability.

1.2 REVIEW OF RELEVANT KNOWLEDGE

1.2.1 Leaching process in hydrated cement paste

(1) Composition of hydrated Portland cement paste

Portland cement is the most widely used binding material in concrete. It is the key ingredient in concrete, mortar, and other construction applications. Portland cement is produced by pulverizing clinkers consisting essentially of crystalline hydraulic calcium silicates, and a small amount of one or more forms of calcium sulfate and up to 5% limestones as an abrasive addition. The clinker contains four mineral phases: tricalcium silicate ($(CaO)_3 \cdot (SiO_2)$, C_3S), dicalcium silicates ($(CaO)_2 \cdot (SiO_2)$, C_2S), tricalcium aluminate ($(CaO)_3 \cdot (Al_2O_3)$, C_3A) and ferrite ($(CaO)_4 \cdot (Al_2O_3) \cdot (Fe_2O_3)$, C_4AF). After clinkers are cooled down, gypsum ($CaSO_4 \cdot 2H_2O$) is added, and mixed then sent to final grinding process. The product after grinding is Portland cement. For ordinary Portland cement (OPC), gypsum content is about 3 to 4 %. The main purpose of adding gypsum in the cement is to slow down the hydration process of cement once it is mixed with water. When the water is added into cement, it starts reacting with tricalcium aluminate and hardened quickly. The reaction time of this process is very less, which doesn't allow time for transporting and placing. With the presence of gypsum in the system, water and C_3A reacts with gypsum and together form ettringite ($(CaO)_3 \cdot (Al_2O_3) \cdot (CaSO_4)_3 \cdot 32H_2O$, AFt) instead. Fine-grained crystals of ettringite forms a coating on C_3A particles. These crystals are too small to fill the gaps between the particles of cement but hinder the progress of hydration to the interior of C_3A particles. The cement mixture therefore remains plastic and workable macroscopically. Cement hydration is a long-term process that can last for years. As hydration continues, the composition of hydrated cement paste is constantly changing. Table 1-1 shows the chemical formulas in hydration.

Table 1-1 Chemical formulas of components

$2(CaO)_3(SiO_2) + 6H_2O \rightarrow (CaO)_3(SiO_2)_2 \cdot 3H_2O + 3Ca(OH)_2$
$2(CaO)_2(SiO_2) + 4H_2O \rightarrow (CaO)_3(SiO_2)_2 \cdot 3H_2O + Ca(OH)_2$
$(CaO)_3(Al_2O_3) + 3(CaSO_4) \cdot 2H_2O + 26H_2O \rightarrow (CaO)_3(Al_2O_3)(CaSO_4)_3 \cdot 32H_2O$
$(CaO)_3(Al_2O_3)(CaSO_4)_3 \cdot 32H_2O + 2(CaO)_3(Al_2O_3) + 22H_2O \rightarrow 3(CaO)_4(Al_2O_3)(CaSO_4) \cdot 18H_2O$

Assuming hydrated cement paste with a water to cement ratio of 0.5, at a curing age of 1 year, volume ratio of each component is calculated as 40% of calcium silicate hydrate phase (C-S-H gel), 10% of portlandite ($Ca(OH)_2$, CH), 10% of monosulfate ($((CaO)_3 \cdot (Al_2O_3) \cdot (CaSO_4)_3 \cdot 12H_2O$, AFm), 10% of unhydrated clinker and 30% of pore space [24].

(2) Pore solution

Water molecules are very small, and therefore, are able to penetrate into extremely fine pores of concrete. As a solvent, water is noted for its ability to dissolve more substance than any other known liquid. Water fills the microscopic pores and capillaries of the concrete, and dissolves certain components in the hydrated cement paste to form a local solution, the so-called "pore solution" [25][26]. The chemistry of the pore solution strongly influences the potential durability of concrete [27][28]. The composition of pore solution reflects the ongoing hydration processes as well as leaching process and it determines which solid phases are stable and may precipitate, and which phases are unstable and may dissolve. The composition of the pore solution is not static but is influenced by factors including but not limited to the following: 1) the original ionic environment of the external water; 2) physicochemical interaction between pore solution and cement hydration products; 3) exchange between the pore solution with external water.

(3) Dissolution process

According to the difference in solubility, the alkalis oxides components in the hydrated cement paste will firstly dissolve into pore solution. The pH of pore solution in OPC is in the range from 13 to 13.8 due to the dissolution of the variable amount of Na_2O and K_2O present in the cements [29]. Sodium and potassium components in Portland cement are mainly derived from the clay components present in the raw mix and coal. Expressed as oxide equivalent content, total amount of sodium oxide (Na_2O) and potassium oxide (K_2O) may range from 0.3 to 1.5% [30].

Portlandite, formed during the reaction of clinkers with mixing water, presents as solid product in hydrated cement paste as alkali reserve, which maintains a PH at 12.5 of pore solution. Unlike alkalis oxide components, Portlandite constitute larger percent of the volume of solids in the hydrated cement paste [24][31]. The low solubility of portlandite makes the pore solution easy to maintain a relatively stable saturated state. Buil's model shows that in the presence of portlandite, the concentration of calcium ions in pore solution will be maintained at 20mmol/L [32]. Unlike the pore solution, which remains relatively stable, the pore structure continuously changes as portlandite dissolves.

With the continuous consumption of portlandite and the exchange of pore solution with external environmental water, when the dissolved calcium hydroxide is not enough to maintain the calcium ion concentration in the pore solution as 20mmol/L, the calcium ion concentration will drop and lead to decalcification of C-S-H gel. C-S-H gel is not a well-defined compound and calcium to silicate ratio (C/S ratio), an important parameter describing C-S-H gel, varies from 1.5 to 2.0 [33][34][35]. As the decalcification proceeds, the C/S ratio of

C-S-H gel decreases continuously. During this period, the pore solution is replenished with calcium ions, which in turn inhibits decalcification until the calcium ion concentration in the pore solution decreases again due to the exchange with external water. Equilibrium between C/S ratio of C-S-H gel and calcium ion concentration in pore solution can be described by the Buil's model [32]. C-S-H gel makes up to 50 to 60 percent of the volume of solids in a completely hydrated Portland cement paste and is the most important phase determining the properties of the paste. When the C/S ratio of C-S-H is lower than 0.9, the C-S-H gel will be decomposed into silica gel, which is considered to no longer have cohesion, and lead to decomposition of hydrated cement paste.

(4) Diffusion process

Transportation in hydrated cement paste can be differentiated into diffusion and permeation according to the driving force. Diffusion is a migration phenomenon of ions that occurs due to the presence of concentration gradient, which can be described by Fick's Law. While permeation occurs due to the presence of pressure gradient, which can be described by Darcy's Law [36]. Without considering seepage, the form of exchange between the pore solution and the external water is diffusion. It is important to understand the rate of diffusion of ionic species in the pore structure of hydrated cement paste.

Diffusion is the process by which substance (including atoms, ions, and molecules) is transported from one part of a system to another as a result of random motions. It is a relaxation process towards a state of thermal equilibrium, and it is an entropy driven process. Fick's Law describe diffusion process and it was first posited by Adolf Fick in 1855 on the basis of experimental result [37]. Fick's first Law describes the rate at which a substance diffuses through a medium and how this rate is related to concentration gradients. The mathematical theory of diffusion in isotropic substances is basis on the hypothesis that the rate of transfer of diffusing substance through unit area of a section is proportional to the concentration gradient measured normal to the section, as shown in eq (1-1):

$$J = -D\frac{\mathrm{d}c}{\mathrm{d}x} \tag{1-1}$$

In which, J is the diffusion flux, representing the rate of diffusion, of which the dimension is the amount of substances per unit area per unit time. $\mathrm{d}c/\mathrm{d}x$ is the concentration gradient, representing the change in concentration of the substance with respect to the distance in the direction of diffusion. D is diffusion coefficient, which characterizes the substance's ability to move through the medium, and it is specific to the substance and the medium.

Fick's Second Law is an extension of First Law and is used to describe the diffusion of a substance in two or three dimensions, accounting for changes in concentration over both distance and time. This law provides a more comprehensive description of how the concentration of a diffusing substance changes with respect to both position and time. In one dimension, it is shown as eq (1-2):

$$\frac{\partial c}{\partial t} = D\frac{\partial^2 c}{\partial x^2} \tag{1-2}$$

The diffusion coefficient showed in eq (1-1) and eq (1-2) is a fundamental parameter in the context of diffusion and describes the rate at which particles, such as molecules, ions, or atoms, move through a medium by diffusion. It quantifies how quickly these particles spread from regions of higher concentration to regions of lower concentration. The diffusion coefficient is specific to both the diffusing substance and the medium through which diffusion occurs. There are two technical paths to calculate the apparent diffusion coefficient, one is to obtain the apparent diffusion coefficient macroscopically through standard tests [38]. The other is to model different factors affecting diffusion process and modify diffusion coefficient on basis of self-diffusion coefficient of ions, and finally obtain the apparent diffusion coefficient of ions. In this research, the latter technical path is taken. For cement-based materials, the pore structure influences the diffusion of substance within it. Understanding the pore structure and its effect on diffusion is critical.

Here, we need to make necessary explanations about self-diffusion and the effect of concentration gradient on diffusion. Self-diffusion, which is a spontaneous mixing of molecules taking place in the absence of concentration gradient. The self-diffusion coefficient can be obtained by measuring the diffusion rate of substance by means of isotope tracing, so it is also called the tracer diffusion coefficient. Chemical diffusion occurs in a presence of concentration gradient, and chemical diffusion coefficient characterizes the ability of a specific chemical species to move through a medium in response to differences in concentration. Self-diffusion coefficient and chemical diffusion coefficient are generally different because the diffusion coefficient of chemical diffusion includes the effects due to the correlation. The self-diffusion coefficient and the chemical diffusion coefficient generally have the following relation, as shown in eq (1-3) [39]:

$$D_C = D_{self}\left(1 + \frac{\mathrm{d}\ln\gamma_A}{\mathrm{d}\ln x_A}\right) \tag{1-3}$$

In which, D_C is chemical diffusion coefficient of substance, D_{self} is self-diffusion coefficient, γ_A is activity coefficient and x_A is composition molar fraction.

In dilute solution, under the hypothesis of $\gamma_A = \gamma^H = \text{constant}$ (γ^H is the activity coefficient of water), we have $\frac{\mathrm{d}\ln\gamma_A}{\mathrm{d}\ln x_A} = 0$, and thus $D_A^C = D_A$. Both pore solution formed during leaching process of cement-based materials and external solution can be considered to satisfy the above hypothesis. Therefore, in the subsequent discussion, we will directly refer to the self-diffusion coefficient, and no additional explanation will be made [39][40][41].

Diffusion coefficient of certain species of ions in porous media is mainly determined by the following factors. 1) Species of ion: Different ions have different atomic masses and charges, and therefore have different self-diffusion coefficients. 2) Effect of other ions: During the diffusion process, the solution still needs to maintain electroneutrality constraint, which makes the interaction between different species of ions. 3) Pore structure of media: From a microscopic point of view, molecules move randomly during diffusion. In porous media, the solid

phase becomes obstacles for molecules, which extends path of movement of molecules and reduces diffusion rate.

(5) Change of pore structure and microstructure

According to the size, pore in hydrated cement paste can be divided into three types: 1) Interlayer space in C-S-H gel: This is the interlayer space of C-S-H gel layered structure. Several scholars have estimated the interlayer space in C-S-H structure, ranging from 3 to 25 Å [42][43][44]. Feldman suggested that this interlayer space is too small to affect the strength and permeability of hydrated cement paste [36][45]. 2) Air voids: Air void is spherical, generally due to small amount of air being trapped into hydrated cement paste during mixing. Its size can be as large as 3mm in concrete. 3) Capillary voids: Capillary voids comes from the space not filled by the solid component of the hydrated cement paste. In well-hydrated cement paste with low water to cement ratio, the capillary voids may range from 10 to 50 nm, while in cement paste at early ages of hydration with high water to cement ratio, the capillary voids can be as large as 3 to 5 μm [36][46].

Interlayer space in C-S-H gel is too small to affect permeability [47], while air void is accidental and not within the scope of this research. Therefore, the analysis in this research focuses on the capillary voids and solvent is considered completely fill the capillary voids in leaching process. In the aforementioned dissolution process, the dissolution of solid phase, mainly portlandite phase and C-S-H gel phase, leads to a decrease in the volume of hydrated solid phase, which inevitably increases capillary voids and changes the pore structure. Changes in pore structure in turn affect the diffusion process, whereas the diffusion process is linked to the dissolution process through a local equilibrium.

The diffusion process is manifested as the random motions of substances in microcosm. If diffusion process takes place in a porous medium, the solid phase acts as an obstacle to the free random motions of substances. Macroscopically, it shows that the diffusion coefficient in porous media is lower than the free diffusion coefficient at the same temperature. To quantify the effect of pore structure on the diffusion coefficient, three parameters need to be introduced: 1) porosity ρ: defined as the proportion of void volume in a space. 2) tortuosity τ: the tortuosity of a porous medium, which represents the degree of convoluted pathways within the material, affects diffusion. Higher tortuosity leads to longer effective diffusion pathways, slowing down the diffusion process. It is well established that in two dimensions, tortuosity is equal to the rate of the length of shortest path in pore structure to the distance between its ends. For the tortuosity in the three-dimensional pore structure, it will be discussed in the next section. 3) connectivity δ: media with isolated pores may impede diffusion because particles have limited pathways to travel. In contrast, media with interconnected pores offer more pathways and enhance diffusion. In this research, connectivity is defined as the ratio of the largest pore cluster volume to the overall pore volume [39][48][49].

Diffusion coefficient in porous media can be calculated as eq (1-4):

$$D_{\mathrm{app}} = D_f \frac{\rho\delta}{\tau} \tag{1-4}$$

In which, D_{app} is apparent diffusion coefficient, i.e., diffusion coefficient in porous media, D_f is self-diffusion coefficient in free space.

(6) Effect of multiple ion leachate

Water exists in many forms in nature, including river water, seawater, groundwater etc. The water body is constantly exchanging substances with the surrounding environment, thus forming its own unique ionic environment. The ionic environment of water body will mainly affect the leaching process in the following two aspects: effect on diffusion process, and reaction with hydrated cement paste.

In diffusion process, both driving forces resulting from concentration gradient of ions itself and other species of ions and driving forces resulting from electrical potential can lead to diffusion movement of ions. In order to satisfy electroneutrality constraint, flux of cationic charge equals to flux of anionic charge, which makes tracer diffusion (self-diffusion) coefficient different from mutual diffusion coefficient. Experimental data shows that, the tracer diffusion coefficient show no obvious relationship to the mutual diffusion coefficient in $MgCl_2$ solution [50][51]. Andrew R proposed model to calculate the mutual diffusion basing on thermodynamics of irreversible process [52][53].

Specific species of ions in water body can affect the interaction between water and hydrated cement paste. The first is the concentration of calcium ions in water body, which directly affect the dissolution of portlandite and the equilibrium of C-S-H gel decalcification [32]. Chloride ions in water, typically seawater, is able to bind with hydrated cement paste and form Friedel's salt [54]. Sulfate ions may react with alumina-containing hydrated product and reform ettringite [55]. The above-mentioned processes involving the reaction with solid phase can change the pore structure of hydrated cement paste and further influences leaching process.

1.2.2 Characteristics of interface transition zone (ITZ)

In 1.2.1 section, leaching process is discussed in homogeneous medium. However, in concrete system, pore structure of the interface transition zone (ITZ) between aggregate and the hydrated cement paste is different from that of the hydrated cement bulk.

(1) Formation of ITZ

In fresh concrete paste, due to surface tension, water will adhere to the surface of the aggregate to form a water film. In the subsequent hydration process, this layer of water film will make the cement paste on the surface of aggregate have a higher water to cement ratio. In addition, the surface of aggregate has the influence of "wall effect", which is manifested in the destruction of the gradation of particle accumulation on the surface of the aggregate. According to numerous researchers, the thickness of ITZ is 10 to 300 μm [56][57][58][59]. It should be noted that estimates of thickness of ITZ are not stationary even within the same specimen from the same study, because the crystal growth process of hydrates, such as calcium hydroxide, also affects the thickness of ITZ [60]. Comparing

with aggregate and hydrated cement paste, ITZ is generally considered the weakest part and the strength-limiting phase in concrete system.

(2) Pore structure and permeability in the ITZ

The microstructure of ITZ can be described by the following two aspects: porous structure and hydration process. Both these two aspects differ from the reaction which happen in bulk hydrated cement paste, due to relatedly higher water to cement ratio of ITZ. The effect of the water-cement ratio on the permeability of concrete is generally attributed to the relationship that exists between the water to cement ratio and the porosity of hydrated cement paste in concrete, which makes relatedly higher porosity in ITZ. Owing to the higher air volume, larger crystallite product can form [60], and therefore form a more porous framework than in hydrated cement paste bulk. In leaching process, ITZ with more porous structure allows easier access of water, which will accelerate the dissolution of hydrated cement paste.

1.2.3 Carbonation process

The normal content of carbon dioxide in atmosphere is 0.04 % (400 ppm) [61]. Reaction of gaseous carbon dioxide with calcium-bearing phase in concrete is so-called carbonation of concrete. In reinforced concrete, carbonation will cause a decrease of alkalinity, and lead to depassivation and corrosion of rebars. But in plain concrete, it has been reported that carbonation can decrease porosity of hydrated cement paste and increase resistance towards leaching deterioration [62]. In addition to natural carbonation, in recent years, the research topic of accelerating the absorption of carbon dioxide by cement-based materials to reduce carbon dioxide emissions in the cement industry has also become a hot topic [19][63][64]. In the foreseeable future, the application scenarios of carbonated concrete are likely to increase. These factors make it necessary to study the durability of carbonated cement-based materials.

(1) Physicochemical

Carbonation of concrete is a complex physicochemical process, which mainly takes place in the cement paste of concrete, whereas carbonation of aggregate is generally not considered. The process of carbonation involves gaseous CO_2 in atmosphere, dissolved and solid hydrated product. Hydrated product reacted with CO_2 include not only portlandite ($Ca(OH)_2$), but also C-S-H gel and unhydrated constituents [65][66]. Table 1-2 shows formulas of carbonation process.

According to whether water is involved or not, carbonation process can be divided into direct dry carbonation and aqueous carbonation. In direct dry carbonation process, portlandite, unhydrated constituents and C-S-H gel directly reacts with CO_2 through gas-solid route [65][67]. In aqueous carbonation, CO_2 diffuse in the matrix firstly, and secondly, the CO_2 id dissolved in pore solution and the Ca^{2+} ions are migrated from the cement particles, and lastly, calcite is formed [68]. Previous study showed that water to cement ratio has a profound effect on carbonation

irrespective of the mix design [67]. It has been concluded by the earlier research studies that the carbonation depth is directly related to water to cement ratio and it is identified that depth of carbonation increases with increase in water to cement ratio [69][70]. It is also directly related to the age of the concrete.

Table 1-2 Formulas of carbonation process

Portlandite	$Ca(OH)_2 + CO_2 \rightarrow CaCO_3 + H_2O$
Unhydrated constituents	$(CaO)_3(SiO_2) + 3CO_2 + vH_2O \rightarrow (SiO_2) \cdot vH_2O + 3CaCO_3$
	$(CaO)_2(SiO_2) + 2CO_2 + vH_2O \rightarrow (SiO_2) \cdot vH_2O + 2CaCO_3$
C-S-H gel	$(CaO)_3(SiO_2)_2 \cdot 3H_2O + 3CO_2 \rightarrow (CaCO_3)_3 \cdot (SiO_2)_2 \cdot 3H_2O$
Ettringite	$(CaO)_3(Al_2O_3)(CaSO_4)_3 \cdot 26H_2O + 3CO_2 \rightarrow 3CaCO_3 + 3(CaSO_4) \cdot 2H_2O + Al_2O_3 \cdot vH_2O + (20 - v)H_2O$

(2) Porosity change

Porosity of cement paste might change under effect of carbonation. Generally, this change can be a decrease in case of Portland cement paste or an increase in case of blended cement paste [71][72][73]. Porosity change under carbonation is caused by transition of hydrated cement phase. Carbonation of portlandite results in an increase of volume and precipitation of calcite in the pore network. Table shows density and molar volume of portlandite and calcite, which clearly show the reduction of total pore volume is associated with calcite deposition. Carbonation of Portland cement paste also cause loss of pore connectivity [74]. On the other hand, in blended cement paste, coarsening of the pore structure may be associated with the formation of additional silica gel due to decomposition of C-S-H gel [75][76]. Table 1-3 shows volume change after transition of portlandite

Table 1-3 Volume change after transition of portlandite

Mineral	Density (g/cm^3)	Molar volume (cm^3)	Variation of volume (%)
Portlandite	2.23	33.20	-
Calcite	2.72	36.93	+11.2

1.2.4 Analysis methods on cement hydrated system

(1) Thermogravimetric analysis and Differential thermal analysis (TG-DTA)

TG-DTA is a combined analytical technique used to study the thermal properties of materials, particularly changes in mass and temperature. TG measures the change in mass of a sample as a function of temperature (or time) under controlled atmosphere conditions. It helps to characterize various thermal events such as decomposition, oxidation, dehydration, and desorption. During TG measurement, the sample is heated or cooled at a constant rate, and the change in mass is continuously recorded. While DTA measures the temperature difference between the sample and a reference material as a function of temperature (or time) under identical thermal conditions. It helps to detect endothermic and exothermic transitions, such as melting, crystallization, and phase transformations. Researchers gave the transition and decomposition temperature of cement phase, as shown in Table 1-4 [77].

Table 1-4 Transition and decomposition temperature of cement phase

Phase	Formula	Nomenclature	Temperature (℃)
Dihydrate gypsum	$CaSO_4 \cdot 2H_2O$	$C\bar{S}H_2$	120
Hemihydrate gypsum	$CaSO_4 \cdot 0.5H_2O$	$C\bar{S}H_{0.5}$	170
Calcium silicate hydrate		C-S-H	115-125
Ettringite	$(CaO)_3(Al_2O_3)(CaSO_4)_3 \cdot 26H_2O$	$C_3A \cdot 3C\bar{S} \cdot H_{32}$	125-132
Brucite	$Mg(OH)_2$	MH	400
Portlandite	$Ca(OH)_2$	CH	450
Calcite	$CaCO_3$	$C\bar{C}$	720-740

(2) Scanning electron microscopy and energy dispersive X-ray spectroscopy (SEM-EDS)

Scanning electron microscopy with energy-dispersive X-ray spectroscopy (SEM/EDS) is an important tool in the field of materials science and can be used to examine the structure and composition of cement-based materials [78]. SEM produces high-resolution images of specimen by scanning it with a focused beam of electron, while EDS detects the characteristics X-rays generated by SEM beam displacing the inner-shell electrons of atoms and analyzes the element present in the specimen. P. Vargas et al. applied SEM-EDS to study ITZ of lightweight concrete [79].

(3) Electron Probe Microanalysis (EPMA)

Electron Probe Microanalysis (EPMA) is based on the interaction of a focused electron beam with a sample, similar to techniques like SEM-EDS. EPMA provides high spatial resolution and quantitative elemental analysis. It is particularly useful for analyzing minor and trace elements in materials. Application of EPMA method to cement-based materials has been increased. It can be used for the accurate estimation of the diffusion coefficient in concrete [80]. Mori et al. obtained chloride concentration profile on concrete section by EPMA and estimated the apparent chloride diffusion coefficient [81]. Moreover, EPMA is also used in analysis of structure of C-S-H gel with different calcium to silicon ratio (C/S). Grangeon prepared an analyzed C-S-H gel with different C/S ratio using EPMA and other methods. Result showed that C-S-H with Ca/Si ratio of ~ 0.8 are structurally similar to nano-crystalline turbostratic tobermorite [82]. Calcium releases from specimen, which can also be analyzed by EPMA. Haga et al. used EPMA to analyze the release of calcium exposed to chemical attack, and the dissolution front can be clarified based on the dissolution of portlandite [83].

(4) X-ray computed tomography (CT)

X-ray computed tomography (CT) is a non-destructive technique for visualizing the internal features of objects. X-ray passes through the object and is projected on the film, and its intensity is reduced due to absorption by the object, so the projection reflects the internal information. Combining projections at different angles can obtain cross-sectional slices of the object. Stacking cross-section slices of different heights can reflect the internal three-dimensional information. Each voxel in stack is assigned a different gray scale brightness, representing X-

ray attenuation level called as linear attenuation coefficient (LAC).

The application of CT technology to cement-based materials has long been [84]. In previous studies, the use of CT technology to analyze the pore structure of cement-based materials accounted for a large part. Visualization of internal pore structure enables more efficient study on mechanical and durability properties of cement-based materials. Vicente et al. characterized pore structure of concrete under fatigue testing [85]. Lu et al. obtained CT images, at a resolution of 7.5 μm/pixel, to measure entrained air-void parameters in Portland cement concrete [86].

With the development of technology, more powerful synchrotron radiation CT technology has also been applied to the research of cement-based materials [87]. It allows researchers to obtain more precise pore structures. Burlion et al. outlined the characterization of microstructural evolution in a mortar subjected to a mortar subjected to a chemical attack [88]. Xu et al. analyzed 3D crack propagation, pore size distribution and orientation, tortuosity, and connectivity of ancient concrete from Pompeii [89]. Pavani et al. analyzed the pore structure of hydrated Portland cement at different temperature on 2D slices using synchrotron micro-tomography [90]. Kim et al. used neutron tomography as supplement of X-ray tomography, to not only segmented the solid phase and the pore phase, but also segmented different components in the solid phase such as fine aggregate and cement paste [91]. Voltolini et al. investigated a mortar affected by alkali-silica reaction (ASR), found that cracks from ASR expansion are different from the common pore structures in materials in terms of morphological parameters, which can be used to characterize the impact of ASR [92].

(5) X-ray diffraction (XRD)

X-ray diffraction (XRD) is a powerful technique used for analyzing the crystal structure of a material. It is based on the principle of X-ray scattering by the atoms within a crystal lattice. When X-rays with a wavelength on the order of the atomic spacing in a crystal interact with the crystal, they undergo constructive and destructive interference. The resulting diffraction pattern provides information about the arrangement of atoms within the crystal, including the distances between them and the angles between the atomic planes. By analyzing the diffraction pattern, scientists can determine the crystal structure, identify the type of crystal lattice, and obtain information about the size and shape of the unit cell. In the field of cement-based materials, XRD technology is mainly used to analyze the composition of products in cement chemistry. Scrivener et al. quantitatively analyzed Portland cement hydration by X-ray diffraction and Rietveld analysis [93]. Stulzmen combined X-ray powder diffraction and microanalysis (SEM) quantitatively characterized phase in Portland cement [94].

With the need for in-depth research, some in-situ XRD techniques have also been gradually. Shaw et al. used synchrotron as source for energy-dispersive X-ray diffraction to study hydrothermal formation of calcium silicate hydrates, tobermorite and xonotlite [95]. Christensen used in situ synchrotron X-ray powder diffraction to analyze formation of ettringite and monosulfate in hydration of Portland cement [96]. Claret combined CT technique and XRD technique to obtained distribution map of phases during hydration and carbonation [97].

1.3 RESEARCH OBJECTIVES

The key objective of this research is to quantitatively analyze the transport properties of hydrated cement paste under natural leaching and to provide a reliable basis for the long-term prediction of leaching deterioration of cement-based material. Due to the time-consuming nature of leaching experiments, many researchers have used acid solutions such as ammonium acetate solutions to accelerate it [10][11][98][99]. But the addition of acid changes the dissolution equilibrium of substance in hydrated cement paste, which cannot reflect the real leaching process correctly and research based on natural leaching is still necessary. It is already known that the changes of phase transitions and transport properties of cement-based material will occur under leaching deterioration. Alteration under leaching can be studied from a macroscopic perspective using methods such as TG-DTA and EPMA. However, these methods are destructive and thus there are few discussions on the in-situ changes of cement-based materials under leaching. In addition, there is still a lack of studies on microstructure of cement-based material subjected to leaching. Especially, although more porous structure of ITZ may have impact on leaching, due to the nature of its micro area, relevant research is still lacking.

To solve these problems, non-destructive integrated CT-XRD method is applied to obtain high precision CT image and integrated XRD information for specimens subject to natural leaching. High precision instruments allow analysis on a tiny specimen of micrometer order. Leaching deterioration on tiny specimen is relatedly obvious. Conducting natural leaching test on such tiny specimen can shorten the research periods without the addition of acid that can change the leaching behavior of hydrated cement paste as in accelerated leaching test. Moreover, the in-situ detection of CT-XRD method shows more details information of alteration. In-situ detection also provides three-dimensional geometric information of specimen, which make it possible to obtain the microscopic pore structure and proceed further transport properties analysis. In addition, with the support of high-precision instrument, the ITZ structure on the surface of aggregate was detected, and its transport properties was also analyzed, which can fill the gap in this field.

Objective of this research can be summarized in the following three points:

1) Studying the applicability of the non-destructive integrated CT-XRD method for the study of natural leaching deterioration in cement-based materials. A tiny specimen was immersed in a given solution for a relatively short period of time as compared with conventional experiments employed in the past. Therefore, the productivity of the related research can be significantly enhanced. The CT-XRD method is being more widely used in cement chemistry, and this study can be seen as a continuation of this trend. The advantages of CT-XRD method, such as high precision and non-destructiveness, are well reflected in research of leaching deterioration. Combining the gray scale value difference on the CT result and the in-situ XRD results, it is expected to obtain the dissolution front formed by the dissolution of portlandite and divided the leaching and non-leaching region accordingly.

2) Quantifying the transport properties of non-leaching region, leaching region and ITZ. Many studies on transport properties of cement-based materials are based on macroscopic experiments. With high-precision detection results, we can analyze transport process of substances based on the microstructure of cement-based

materials. Through processes of binary and pore cluster labeling, the pore structure can be extracted from the detected three-dimensional geometric information. The transport properties of different region in the specimen can be analyzed by simulating the diffusion process of substance using the random walk algorithm. Furthermore, through an original image processing method, we start to divide the regions from the irregular surface of the aggregate, and analyze the transmission performance of each region, and attempt to obtain continuous change of the transport properties from the aggregate surface to the leaching region.

3) Predicting the long-term leaching deterioration of cement-based materials. With the evaluated result of transport properties of each region, prediction of leaching behavior of cement-based materials is conducted. The verification of the evaluation results is obtained by predicting the experimental specimens and comparing the predicted results with the experimental results. The evaluation results are later used to predict the leaching deterioration of concrete. Effect of ITZ on the progress of deterioration is evaluated. Moreover, combining with the background of the Fukushima nuclear accident, the simultaneous diffusion of Sr^{2+} into structure during leaching process is also simulated.

1.4 STRUCTURE OF THIS THESIS

In order to explain the research process and conclusion clearly, this thesis would be divided into six chapters, as shown on Figure 1-1. Chapter 1, i.e., this chapter, introduced background of the issue and literature reviews of basic knowledge, including leaching mechanism, characteristics of ITZ and carbonation mechanism. Research object, purpose and structure of this thesis are also introduced. Chapter 2 introduced experiment and measurement in this research. Test procedures, including specimen preparation, carbonation processing, leaching test and CT-XRD measurement are described. Chapter 3 introduced the transport properties analysis method. Pore structure was obtained by image processing method, and transport properties by simulating the diffusion process using the random walk algorithms in the obtained pore structure. Chapter 4 focuses on how to apply transport properties analysis method to leaching altered specimen. Phase transition under pure water leaching, carbonation and seawater leaching was confirmed. Based on the alteration of specimens leched region and non-leached region were divided. The analysis on the transport properties change from the aggregate surface to the non-leached region and all the way to the leached region was carried out. Transport properties of non-leaching region, leaching region and ITZ were quantified. Chapter 5 mainly described how to use the obtained data from image analysis to predict the leaching of cement-based materials. Simultaneous ion transport model (SiTraM2D) was introduced, and the leaching of concrete was simulated using obtained results. A method for estimating the extent to which harmful components enter the interior of cement-based materials through leaching processes was also proposed. Chapter 6 summarizes the conclusions from experimental and analytical results of this research. Recommendations for future works were also made.

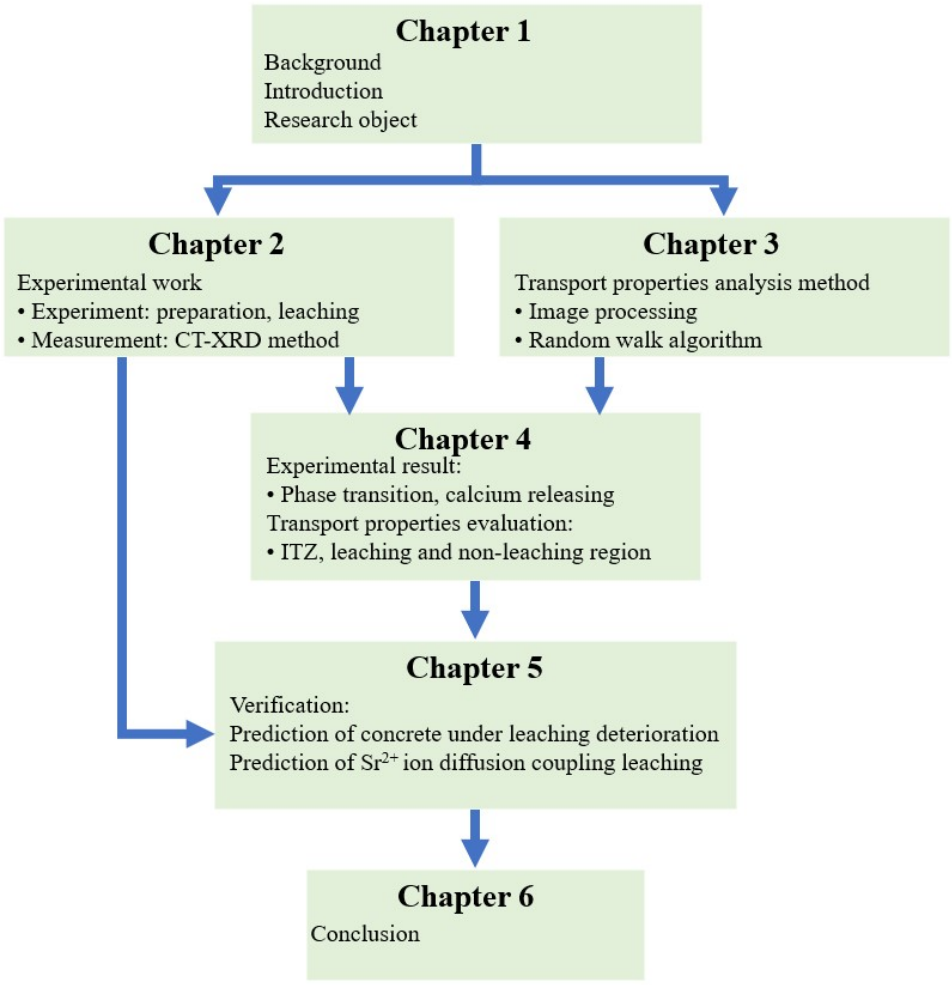

Figure 1-1 Structure of this thesis

CHAPTER 2 EXPERIMENT AND MEASUREMENT

2.1 GENERAL

This chapter explains the preparation of specimens, process of conducting leaching and carbonation tests, and non-destructive CT-XRD measurements used in this research. In order to shorten the experimental period and adapt to the CT-XRD methods, tiny specimens are prepared, and preparation process was introduced in section 2.2. Effect of leaching and carbonation on cement-based materials are the main research objects of this research. Leaching process and carbonation process are introduced in section 2.3. In section 2.4, non-destructive integrated CT-XRD method, the primary measurement method used in this research, is detailly introduced, including its mechanism, facilities, and development.

2.2 SPECIMEN PREPARATION

As a relatively slow form of deterioration, the study of natural leaching is always time consuming. Conducting natural leaching on tiny samples and applying high-precision analysis is one of the methods to shorten the research period. Moreover, the CT imaging technique has the characteristics of high precision and accuracy, but for oversized specimen, scanning will be time consuming. As a result, a tiny cylindrical specimen was used in this research. Size of specimen is selected as 3 mm in diameter and 6mm in height.

2.2.1 Proportion and labeling

Specimens were plain cement pastes and cement pastes with a single aggregate. The binder was ordinary Portland cement (OPC). The density and fineness of OPC in terms of Blaine specific surface area are 3.16 g/cm^3 and 3200 cm^2/g, respectively. Compositions of cement are shown in Table 2-1. Aggregate used was limestone and the particle size ranged from 0.6 mm to 1.0 mm, while the density was 2.71 g/cm^3.

Table 2-1 Chemical composition of cement

Oxide composition	CaO	SiO_2	Al_2O_3	Fe_2O_3	MgO	SO_3
Mass fraction (%)	65.01	21.41	4.84	3.20	1.08	2.02
Compound composition	C_3S	C_2S	C_3A	C_4AF		
Mass fraction (%)	59.09	16.81	7.41	9.74		

Before mixing, materials were calculated as a water to cement ratio of 0.5 and 0.6 respectively, as shown in Table 2-2. Relatively high water to cement ratio is adopted for the following reasons: 1) Specimen with a higher water to cement ratio have greater porosity and can undergo faster leaching process to further shorten research period. 2) The resolution of the CT scanning technique used is about 2.4 μm/pixel. The capillary pore size in the

pore structure of high water to cement ratio samples is closer to the analysis accuracy, which makes subsequent pore structure analysis more effective.

Table 2-2 Proportion of different water to cement ratios

Water to cement ratio	Water (kg/m^3)	Cement (kg/m^3)
0.5	613	1225
0.6	643	1071

In this research, involving in the processing of multiple specimens tested under different conditions, it is necessary to stipulate the labeling rules of the specimens. The classifications are based on specimens tested under pure water leaching or seawater leaching, with different water to cement ratios (0.5 and 0.6), with or without aggregate, with or without carbonation, with different leaching periods, and under different leaching temperatures. Uniformly, the labeling convention is “type of solvent” + “water to cement ratio” + “with or without aggregate” + “with or without carbonation” + “leaching period” + “leaching temperature”. Table 2-3 shows meaning of labeling, while Table 2-4 shows some examples of labeling.

Table 2-3 Meaning of labeling

Processing type	Pure water / Seawater	Aggregate	Carbonation
Without processing	default	default	“N”
With processing	“S”	“L”	“C”
	Water to cement ratio	Leaching period (days)	Leaching temperature (℃)
0.5	5	Number + “d”	Number + “c” For room temperature, default
0.6	6		

Table 2-4 Labeling examples

Labeling	Description
S6N20d	Leaching in seawater, water to cement ratio equals to 0.6, plain hydrated cement paste, without carbonation, after 20 days leaching, leaching in room temperature
5LN33d20c	Leaching in pure water, water to cement ratio equals to 0.6, with aggregate inside, without leaching, after 33 days leaching, leaching in 20 ± 2 ℃ environment
5C120d	Leaching in pure water, water to cement ratio equals to 0.5, plain hydrated cement paste, with carbonation, after 120 days leaching, leaching in room temperature

2.2.2 Molding, demolding, curing, and storing

The cement paste is mixed and placed into a cylindrical plastic mold with a dimension of 3 mm in diameter and 6 mm in height. For specimens containing aggregate, one piece of limestone is gently inserted into the fresh cement paste as aggregate, as shown in Figure 2-1. Specimens are demolded after 24 h and cured by being wrapped in a wet towel at 20 ± 2 ℃ for four weeks.

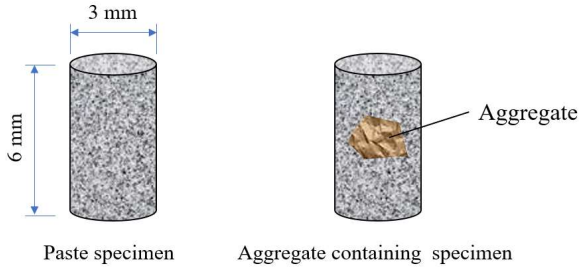

Figure 2-1 Schematic diagram of specimens

Integrated CT-XRD technique requires specialized instruments and are only conducted at SPring-8, which has the schedule of using CT-XRD method to be arranged at predetermined time. This is inconvenient for some specimens that require fixed leaching period. As a result, for some specimens we soaked them into acetone and then vacuum them to stop the hydration. They were stored under vacuum conditions until CT-XRD measurement.

2.3 LEACHING AND CARBONATION TEST

2.3.1 Solvent preparation

Two kinds of solvent are used in this research, namely deionized water (pure water), and modulated seawater.

Deionized water is water that has nearly all of its ions (electrically charged atoms or molecules) removed through a process known as deionization. This means that most of the mineral salts and impurities present in regular tap water or natural water sources have been eliminated. In this research, we firstly selected pure water as solvent to remove the influence of ions to study the leaching behavior of the specimen.

In order to analyze the influence of ions on leaching process, we also studied the leaching process in seawater. In order to exclude the influence of biological factors in natural seawater, modulated seawater was prepared. Ion composition in the modulated seawater is shown in Table 2-5:

Table 2-5 Ion composition in modulated seawater [100]

Ion composition	g/kg of seawater	Moles/kg of seawater
Chloride (Cl^-)	19.162	0.541
Sodium (Na^+)	10.679	0.465
Magnesium (Mg^{2+})	1.278	0.053
Sulfate (SO_4^{2-})	2.680	0.028
Calcium (Ca^{2+})	0.410	0.010
Potassium (K^+)	0.395	0.010

2.3.2 Carbonation process

Carbonation of cement-based materials is unavoidable under the air. The response of cement-based materials after carbonation subjected to leaching is also one of our research objects. In order to evaluate the leaching behavior of carbonated specimen, some specimens were prepared for an accelerated carbonation test after curing for 28 days. In the accelerated carbonation test, specimens were firstly placed into airtight plastic container, which has two valves on it, as shown in Figure 2-2. The interior of container was evacuated to a vacuum using a vacuum pump, and then pure carbon dioxide (99 %) is injected subsequently. During the accelerated carbonation test, carbon dioxide was complemented every three days and for the remainder of the test while the container remained sealed. The accelerated carbonation test was carried out over a period of two weeks.

Figure 2-2 Container for accelerated carbonation test

2.3.3 Leaching process

Specimen was immersed in the corresponding solvent during leaching test. To accommodate the size of the tiny specimens, the volume of solvent used in leaching test is 10 mL. Figure 2-3 shows the size of single specimen, one Japanese yen coin and bottle for leaching test (10 mL solvent inside). The solvent needs to be replaced timely because of the following reasons: 1) The components released from the specimen will increase the ion concentration in the solvent. Due to the existence of diffusion equilibrium and dissolution equilibrium, it will in turn inhibit the leaching process. 2) The amount of ions in the solvent reflects the amount of components released from the specimen. Measuring the ion concentration of replaced solvent allows us to quantify calcium released amount from specimen. For leaching test that require specific temperature, the bottles containing specimen and solution were placed as a whole in an incubator.

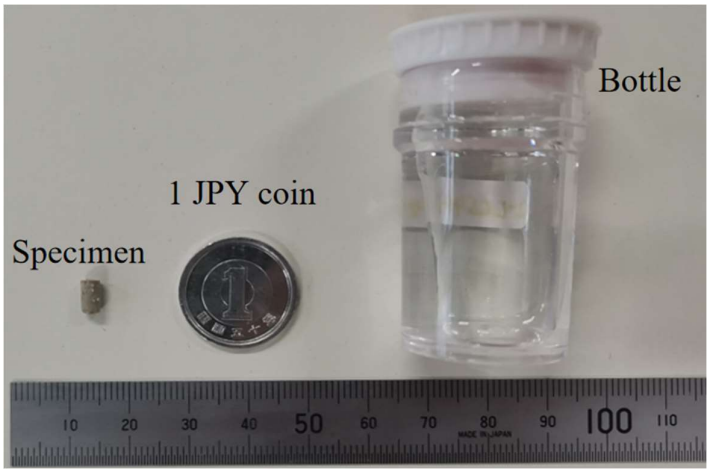

Figure 2-3 Size of one specimen and bottle

2.3.4 Test procedures, overview of specimens and measurements

Test procedures of specimens in different series can be roughly summarized in Figure 2-4. Table 2-6 shows an overview of specimens, and detailed descriptions of each kind of specimens will be given in subsequent chapters.

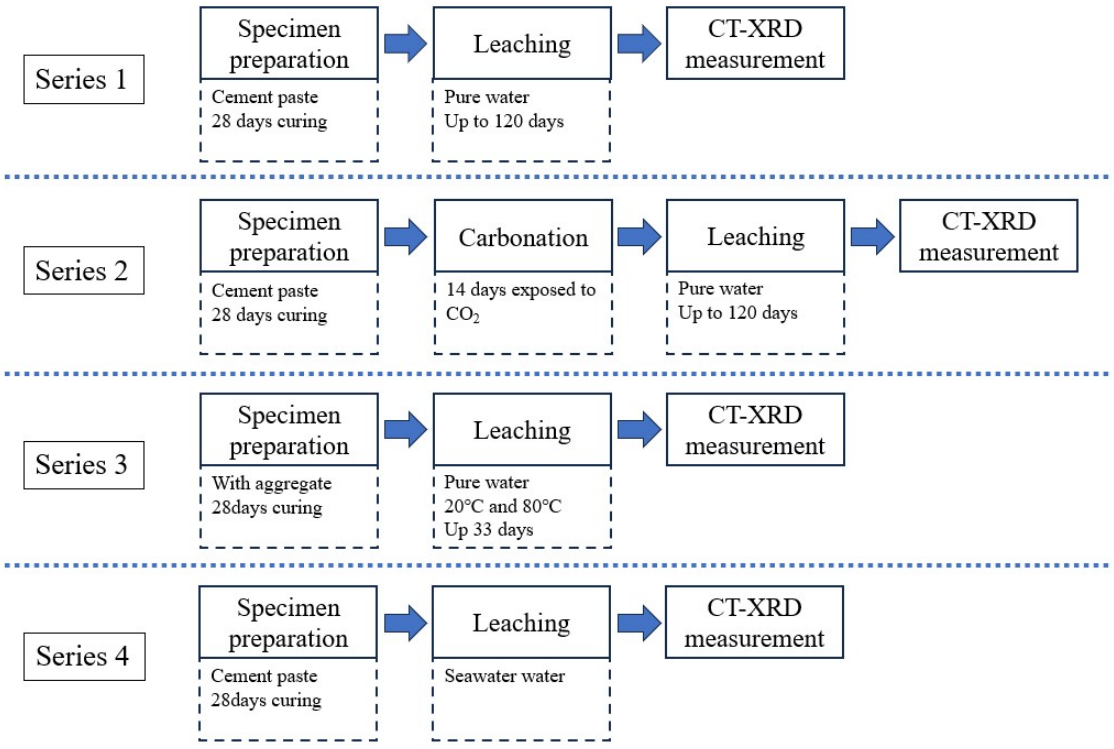

Figure 2-4 Test procedures of specimens

Table 2-6 Overview of specimens and measurements

Series		1	2	3	4
Pre-treatment	Aggregate containing	× *	×	√	×
	Carbonation	×	√	×	×
Leaching test	Solvent	- **	-	-	S
	Temperature (℃)	20	20	20 & 80	20
	Leaching period (days)	120	120	33	147
Measurement	CT-XRD, (time point (days))	0,7,15,60,120	0,7,60,120	33	21, 147
	ICP-OES ***	√	√	√	×
	Powder XRD	√	√	×	√
	TG-DTA	√	√	×	√

*: "×" representing without this processing or measurement while " √ " representing with.

**: "-" in solvent column representing default pure water while "S" representing seawater.

***: ICP-OES measurement conducted on replaced solvent after each exchange.

2.4 NON-DESTRUCTIVE INTEGRATED CT-XRD METHOD

2.4.1 Basic introduction of facility

CT (Computed Tomography) and XRD (X-ray Diffraction) are common research method, which enable researchers to obtain three-dimensional information of specimen and phase composition of materials, respectively. Light source quality has an important influence on both CT imaging resolution and XRD measurement accuracy. In pursuit of better light source, CT-XRD technology using synchrotron radian from accelerators as light source was developed, namely as Synchrotron microtomography. "Synchrotron microtomography," sometimes referred to as "synchrotron X-ray microtomography," is a powerful imaging technique used to obtain high resolution three-dimensional images of the internal structure of a wide range of materials. With development of synchrotron microtomography (μCT) technique and demand for high-precision imaging in the study of cement-based materials, microtomography using synchromatic radiation as the X-ray source has been applied in many previous building materials relative research [101]. Bentz, Dale P. et al. used three-dimensional μCT technique to analyze microstructure of building materials [102]. Hitomi, T. et al. analyzed fine structure of mortar with μCT technique as SPring-8 [103]. Helfen, L. et al. characterized the hydration process of Portland cement [104]. Burlion, Nicolas et al. analyzed the leaching process of cement-based materials and calculated porosity of specimen subject to acid leaching [88]. Gallucci, E. et al. studied cement pastes aged from 1 to 60 days [105]. Takahashi et al. used μCT technique to analyze cement-based materials subject to high temperature and pure water [106][107][108]. Non-destructive integrated CT-XRD used in this research has been originally developed at BL28B2 in Super Photon Ring-8 GeV (SPring-8), Harima Science Garden City, Hyogo Prefecture, Japan [106][107]. It is one of the world's most advanced and prominent synchrotron radiation facilities, known for producing high-intensity, high-brilliance X-ray beams for a wide range of scientific research and industrial applications. SPring-8 consists of a storage ring

containing an 8 GeV electron beam and on its path around the storge ring, the beam passes through different facilities to obtain synchromatic radiation with energies ranging from soft X-ray (300 eV) up to hard X-rays (300 keV). From the first beam was produced in 1999, and data-taking commenced in 2000, the synchrotron radiation produced at SPring-8 has been used for materials analysis and biochemical protein characterization by many manufacturers and universities [109].

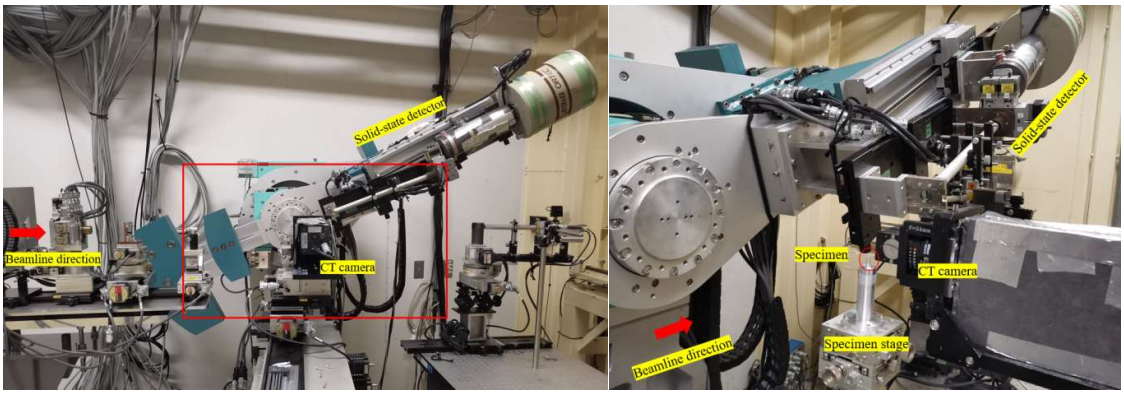

Figure 2-5 Equipment for non-destructive integrated CT-XRD method

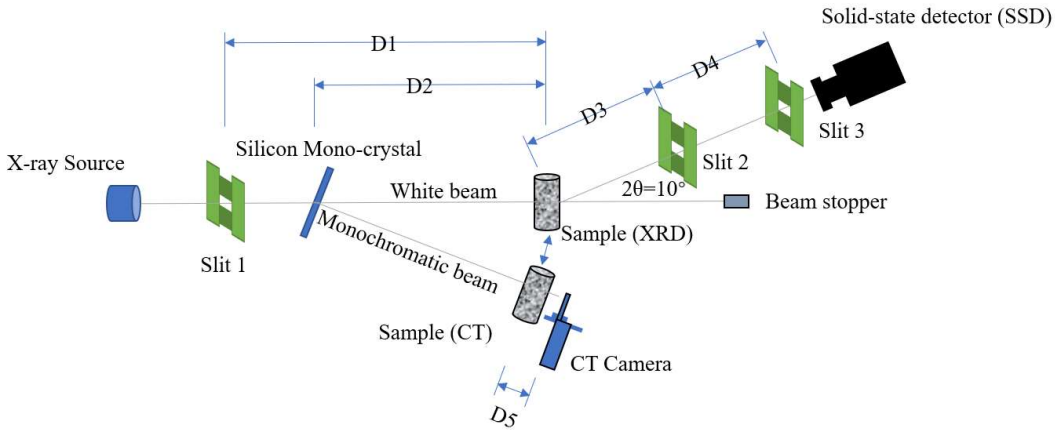

Figure 2-6 Schematic diagram of the system for non-destructive integrated CT-XRD method

BL28B2 at SPring-8 is one of the beamlines (experimental stations) at the SPring-8 synchrotron radiation facility. It is white X-rays beam line for multi-purpose, including high precision computed tomography, white X-ray diffraction (XRD), X-ray absorption fine structure (XAFS) for studying chemical and/or physical reaction process, and biomedical imaging and radiation biology studies. Figure 2-5 shows CT-XRD equipment used in this research inside the hutch in SPring-8, and appearance of specimen. The Equipment can be roughly divided into X-ray source, slit system, CT camera, solid-state detector (SSD) and stage for specimen, while Figure 2-6 shows schematic diagram of the system for non-destructive integrated CT-XRD method. There are two light paths in Figure 2-6. The first light path is for CT measurement. X-ray passes through silicon mono-crystal and specimen successively, and images on CT camera. In the second light path, white X-ray passes specimen and captured by

SSD, is for the in situ XRD measurement [110]. The positional relationship between various units of the equipment and the specimen is determined by D1 to D5, as shown in Figure 2-6. The CT-XRD results obtained in SPring-8 covered in this research were obtained from multiple measurements. In the same series of measurements, the position of each unit would not change once determined, but for different series, to improve imaging quality, position of each unit will be adjusted. For example, adjusting the distance from the CT camera to the specimen can lead to better focus and improve the image. Table 2-7 shows position of each unit in each series of measurement. More details for CT and XRD measurements are shown in subsequent sections.

Table 2-7 Position relationship among units in each series of measurement (mm)

Measuring time	2020-11	2021-06	2021-10	2021-11	2022-05	2023-05	2023-10
D1	800						
D2	600						
D3	170						
D4	450						
D5	30	30	30	60	60	60	60

2.4.2 CT measurement and image processing

Since Roentgen discovered X-rays and took the first picture, humans have gained the ability to observe internal of object. However, in the single picture, the internal structures overlap, making further distinction difficult. Obtaining tomographic images without structural superposition has been the dream of many researchers throughout history. Radon proposed the mathematic tool for reconstructing the set of projections into cross-section image in as early as 1917, but due to limitations of computing power, obtaining a clear internal structure still remains to challenge. With the development of mathematical tools and advances in computer technology, the first CT scanner was finally invented in the 1970s. Although CT technology has many variations and technological improvements so far, its basic processes are still the same: from projection to cross-section. Here, we follow this path to explain the synchrotron radiation CT scanning technology used in this research.

Raw CT images, or projections are obtained using synchrotron radiation through the following processes: As shown in Figure 2-6, white X-ray firstly produced from end of accelerator, and then is diffracted by silicon mono-crystal. Monochromatic X-ray can be obtained at a specific angle of outgoing light path. On the path of monochromatic X-ray, specimen and X-ray camera are set successively. Line beam of monochromatic X-ray is reduced as it passes through specimen due to absorption, and imaging by emerged reduced X-ray reflects internal structure of specimen. The projection of X-ray on the camera is the raw CT image [111][112]. The reason for using monochromatic X-ray instead of white X-ray directly is as follows: white X-ray contains photons with various wavelength, and its imaging on the CT camera is not only affected by the absorption of the specimen, but also by wavelength of photons [113]. In contrast, monochromatic X-ray has single wavelength and its imaging on the CT camera will reflect absorption of specimen more effectively.

X-ray projection (all referred to raw CT image in the following) on camera reflects the intensity of the exposure by lightness, which contains the structural information inside the specimen. However, a single projection cannot accurately reflect the interior of the sample, and projections at virous degree are required for analysis [111][112][114]. To accurately grasp internal information of specimen, imaging data at different exposed angle of specimen need to be obtained. The number of projections is an important parameter indicator of CT imaging. In this research, raw image with different angles were obtained by rotating the specimen at 0.12° in each step until a 180° rotation was completed, total 1501 slices of raw images for each specimen. Projections (raw images) need to be converted into sectional images to observe internal of specimen. To achieve that, sinogram and inverse Radon transformation need to be introduced. Sinogram is formed by splicing all projection of a single cross-section at different projected angle, while inverse Radon transformation is the mathematical tool that connects the sinogram and sectional image. The process is shown in Figure 2-7: arranging and combining single layer pixels in all raw images, sinogram of corresponding layer can be obtained. Inverse Radon transformation is subsequently introduced to obtain sectional images of specimen (all referred to reconstructed image in the following) [114]. Figure 2-8 shows reconstructed image of layer 720. Stacking all reconstructed images sequentially, images stack which reflect internal 3D geometry information of specimen can be obtained, also shown in Figure 2-8. Table 2-6 shows details information of the CT measurements in this research. For scanned region, there were 1440 slices except the last measurement. If taking size of one pixel as 2.4 μm per pixel, the height of the scanned region is about 3.46 mm.

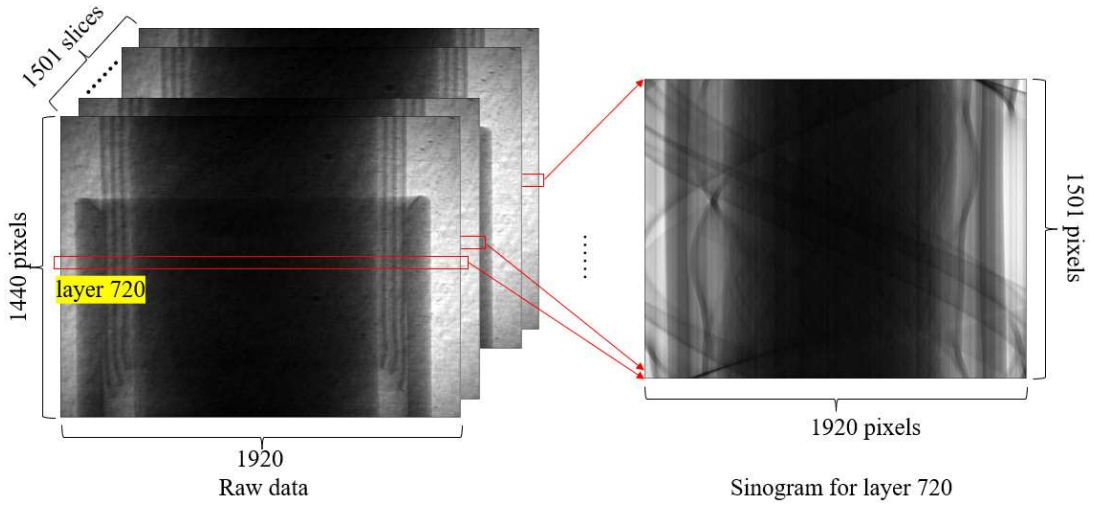

Figure 2-7 Generation of sinogram

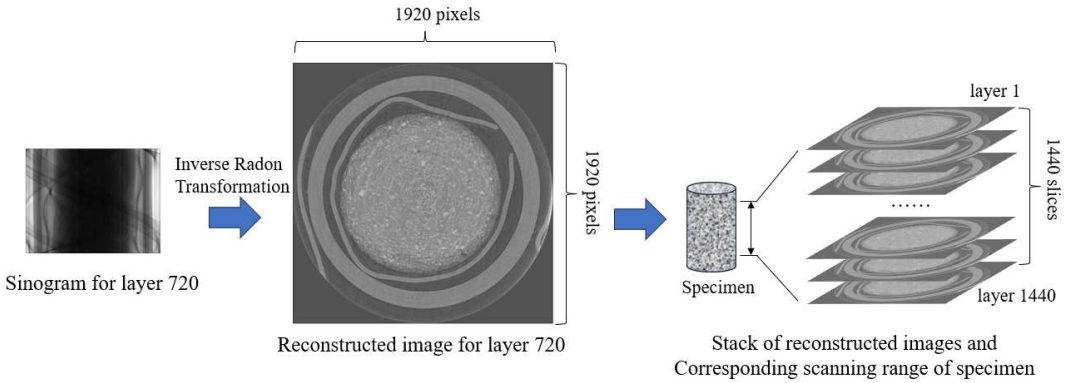

Figure 2-8 Reconstruction process and stack of reconstructed images

Table 2-8 Detailed information of the CT measurements in this research

Time of measurement	2020-11	2021-06	2021-10	2021-11	2022-05	2023-05	203-10
Extracted X-ray energy (keV)	25						
Exposure time (s)	0.4						
Step of rotation (°)	0.12						
Projection number	1501						
Slices number in stack	1440						1200
Pixel size (μm/pixel)	2.46	2.46	2.45	2.31	2.35	2.46	3.2
Size of slice (pixels)	1912	1920	1914	1912	1920	1920	2304

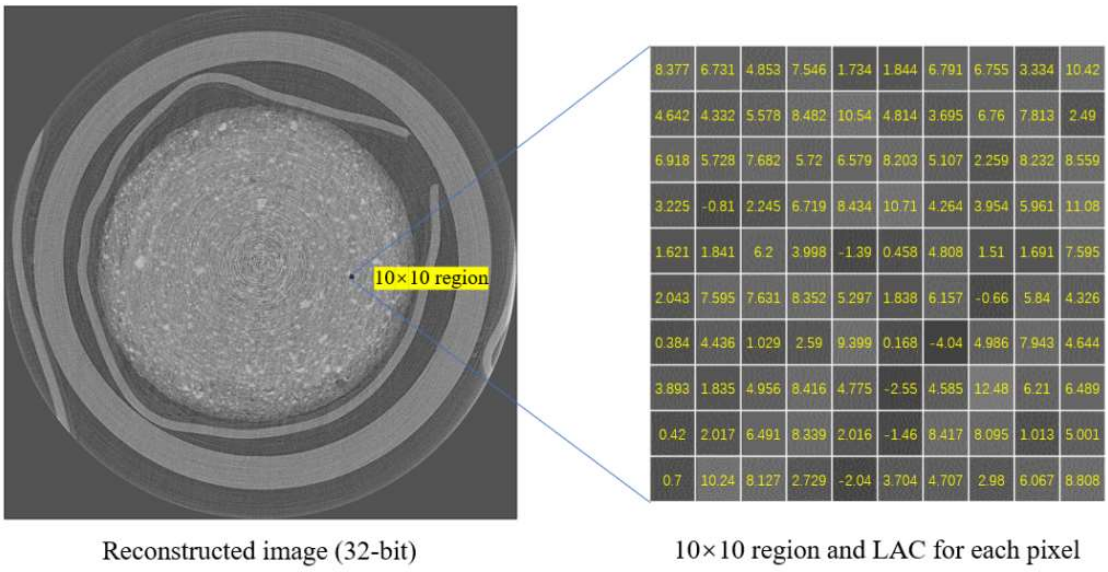

Figure 2-9 Data form of reconstructed image (32 - bit)

Every pixel on the reconstructed image has a corresponding data, as shown in Figure 2-9. Its physical meaning is the linear attenuation coefficient (LAC) of the materials within the range of the pixel at X-ray energy

of 25 keV. The linear attenuation coefficient is a measure of how effectively a material absorbs or scatters radiation, such as X-rays or gamma rays. It quantifies the decrease in the intensity of the radiation as it travels through the material. The linear attenuation coefficient depends on the type and energy of the radiation, as well as the properties of the material. Promentilla et al. calculated LAC for different phase in cement chemistry at the X-ray energy level of 15 keV [115]. Its relationship with intensity of monoenergetic photons is given by the exponential attenuation law [113], as shown in eq (2-1):

$$\frac{I}{I_0} = \exp\left[-\mu x\right] \tag{2-1}$$

In which, I_0 is intensity of incident monoenergetic photons of narrow beam, I is intensity of emerged photons, x is thickness of substance, and μ is linear attenuation coefficient (LAC)

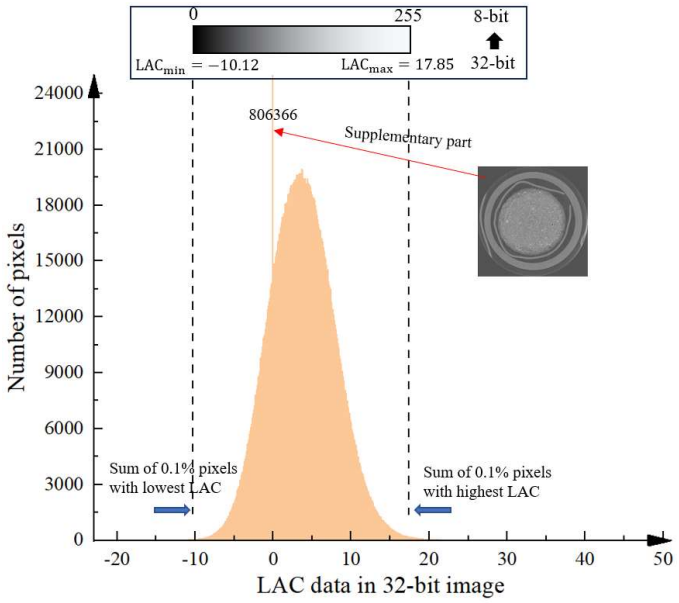

Figure 2-10 Histogram and conversion of 32 - bit image to 8 - bit image

In reconstructed image (32 - bit), every pixel has a floating-point number to characterize the LAC, which makes the total data amount of one image stack (with 1440 slices) huge (around 19.3 Gb). To process data more efficiently, in this research, 32 - bit images is generally converted to 8-bit images before subsequent processing. Figure 2-10 shows histogram of 32 - bit image and conversion to 8-bit image. Figure 2-11 shows conversed 8 - bit image. In conversion, in order to allow more precise analysis of pixels centered in the median range, minimum and maximum value of LAC are set to narrow the range. For pixels with out-of-range data, their data are set to minimum and maximum respectively.

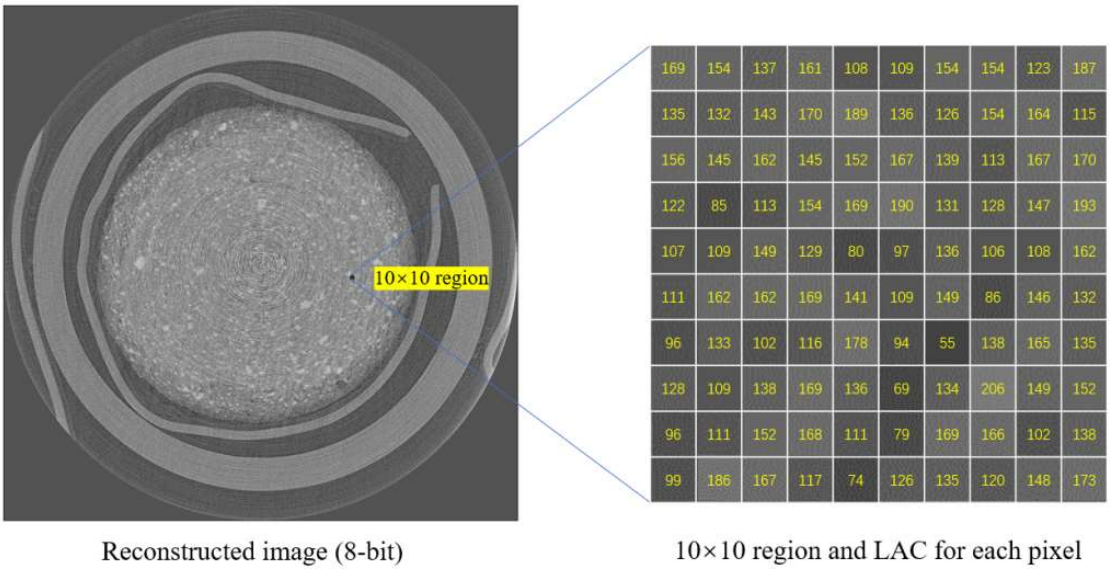

Figure 2-11 Data form of reconstructed image (8 - bit)

In 8 - bit reconstructed image, every pixel has an integer number in the range of 0-255, also called gray scale value (GSV) in the following. According to the process of converting a 32-bit image into an 8bit image, the following relationship exists between GSV and LAC:

$$GSV = (\frac{LAC - LAC_{min}}{LAC_{max} - LAC_{min}}) \cdot 255 \tag{2-2}$$

GSV is an integer data. In conversion from 32 - bit images to 8 - bit images, the reduction of the amount of data is achieved by mapping the original floating-point data within a certain range to a specific inter data between 0 - 255. 8 - bit images have been widely used in the field of image processing for a long time because of their simple data form and easy processing [116]. In the follow-up content, if no explanation is given, when it comes to reconstructed image, they will default to 8 - bit reconstructed images. It should be pointed out that because LAC_{min} and LAC_{max} are set differently for different specimens, grayscale value for CT image of different specimen cannot be compared with each other.

2.4.3 Synchromatic XRD measurement and crystal phase analysis

Laue first discovered the diffraction phenomenon of X-rays on crystal structures and the Braggs developed a crystal structure analysis method based on this. The wavelength of X-ray (0.01 nm – 10 nm) is similar to the distance between the atomic planes inside the crystal. This crystal can be considered as a diffraction grating for X-ray. That is, when a beam of X-rays is illuminated on an object, it is scattered by the atoms in the object, and each atom is scattered. These waves interfere with each other, resulting in diffraction. The result of the superposition of diffracted waves is that the intensity of the ray is strengthened in some directions and weakened

in other directions. By analyzing the diffraction results, the crystal structure can be obtained. The above is the basic principle of X-ray diffraction. XRD analysis is widely used in phase analysis in different field. XRD measurement has various forms, in which, the most commonly used is to irradiate the sample with monochromatic light and measure the diffraction peaks at different angles by adjusting the angel of light path to generate pattern of intensity-2θ, such as powder XRD method. In contrast of this, XRD analysis system in SPring-8 uses the same X-ray source as CT measurement, but not through the silicon mono-crystal, which is white X-ray. Compared with general XRD technique, XRD technique using the same synchrotron radiation in the CT-XRD method has the following advantages: 1) Synchrotron-based XRD is non-destructive, making it suitable for analyzing precious or irreplaceable samples without altering or damaging them. 2) Synchromatic X-ray source can provide higher photon energy (~100 keV) and it makes the information collected by powder XRD at a diffraction angle of 120° can be completed at 10° under high-energy X-ray photons, which shorten measurement time. 3) Divergence of synchromatic X-ray source is small, so that the size of spot can be small, which makes analysis on in situ region of interest possible [117]. Synchromatic XRD system is shown in Figure 2-6, angle between incident light path and the emerged light path of solid-state detector in XRD system is fixed as 10° and never change in XRD measurement. After the computed tomography is completed, the region of interest (ROI) of XRD measurement can be located based on the three-dimensional information obtained from the CT measurement.

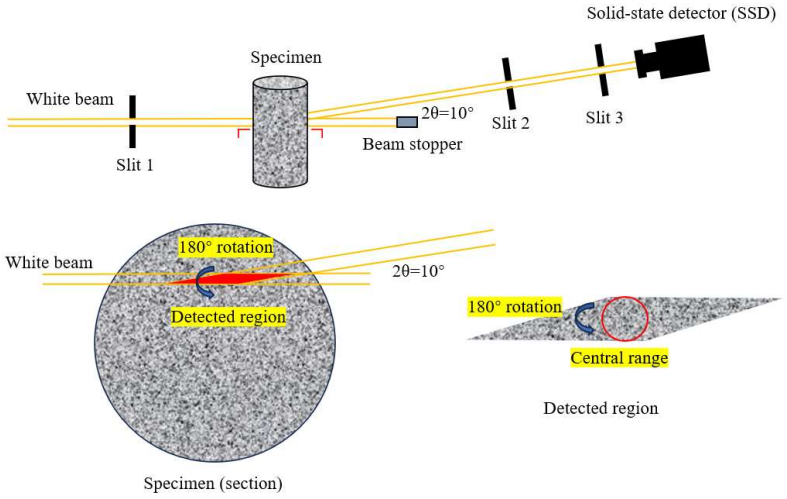

Figure 2-12 Detected region in XRD measurement

Detected region in XRD measurement is determined by overlapping portion of incident path and emerged path, forming an irregular quadrilateral, as shown in Figure 2-12. In order to ensure that the crystal structures of different attitudes are well detected, the specimen rotates 180° around the intersection point of incident light path and emerged light path during the measurement. It should be noted that due to rotation of specimen while the detected region is fixed, region outside the central range will also be detected which may result in interference signals.

White X-ray contains photons of many different wavelengths. When the wavelength of photons is exactly

equal to the interplanar spacing of the crystal, superposition enhancement of scattered photons occurs. In the data obtained by solid-state detector (SSD), it appears that there is a peak at this energy. Obtained relationship between energy of X-ray and detected intensity in solid-state detector is shown in Figure 2-13 as an example.

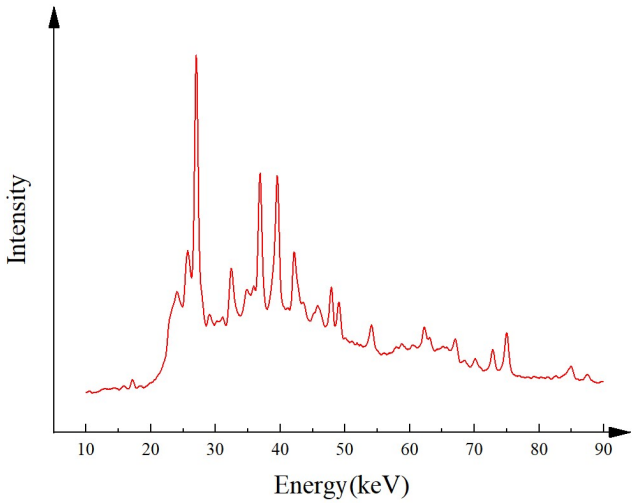

Figure 2-13 Intensity-Energy relationship (detected pattern)

Similar to the powder XRD method, the position and intensity of peaks in Figure 2-13 is related to the interplanar spacing, which can reflect the crystal phase type of sample. By comparing the detected pattern with the XRD standard data of specific crystal phase in a given database, the information of whether the crystal phase exists can be obtained. However, it should be noted that the pattern obtained by the Synchromatic XRD method is in energy scale, while standard XRD pattern in most database is in 2θ angle scale. In order to use the already widely applied crystal database in powder XRD experiments, it's necessary to transfer energy scale into Cu Kα1 2θ angle scale. In principle, various forms of XRD detection methods can be described by Bragg's Law. Bragg's Law is a fundamental principle in the field of X-ray and neutron diffraction that describes the relationship between the angles at which X-rays (or neutrons) are scattered by a crystal lattice and the wavelength of the incident radiation. Bragg diffraction occurs when radiation of wavelength comparable to atomic spacings, wavelength, scattering angle and spacing of atomic lattice have a strict relationship as shown in eq (2-3):

$$n\lambda = 2d\sin\theta \tag{2-3}$$

In which, n is the diffraction order and it is an integer, λ is wavelength of incident X-ray, d is spacing of atomic lattice and θ is the angle of incidence, also the angle between the incident beam and the lattice plane. Wavelength of incident X-ray (λ) and energy(E) can be connected by Planck–Einstein relation, as shown below in eq (2-4):

$$E = hc/\lambda \tag{2-4}$$

In which, E is energy of photon, h is Planck constant, taking as $6.62607015 \times 10^{-34}$ m^2kg/s, c is the speed of light

in vacuum, taking as 299792458 m/s, and λ is the wavelength of photon.

By introducing Bragg's law, energy scale (E) in Fig can be transferred into Cu Kα1 2θ angle scale.

$$\lambda = 2dsin5°$$
$$\lambda' = 2dsin\theta \quad (2\text{-}5)$$

It can be combined as eq (2-6):

$$\theta = \arcsin\left(\frac{\lambda' Esin5°}{hc}\right) \quad (2\text{-}6)$$

In which, λ is wavelength of incident X-ray, d is spacing of atomic lattice, λ' is wavelength of Cu Kα1 radiation, taking as 1.54059 Å, and 5° is determined by the equipment used in this research. Relationship between energy scale and 2θ angle scale is shown in Figure 2-14.

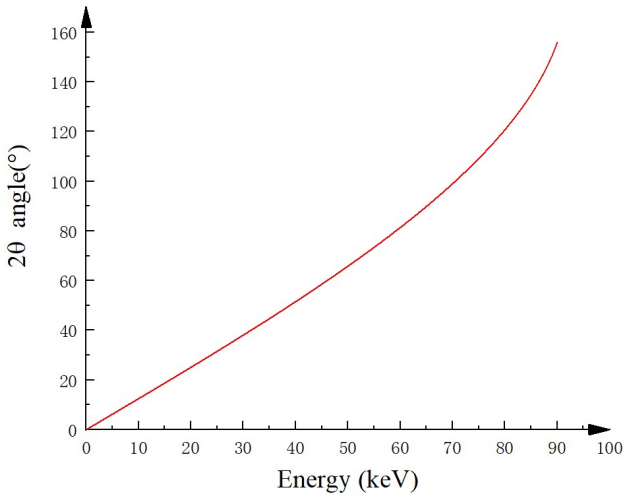

Figure 2-14 Transformation from energy scale to 2θ angle scale

In actual operation, converting the energy of the original data into corresponding angle while keeping the intensity constant can turn the pattern into Cu Kα1 2θ angle scale. XRD detected pattern after transferring into Cu Kα1 2θ angle scale is shown in Figure 2-15 as an example, and this pattern can be compared directly using the standard pdf files in the database [118].

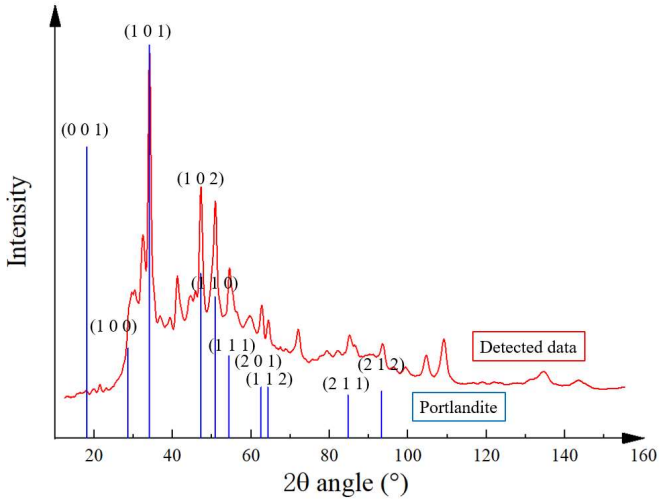

Figure 2-15 XRD detected pattern after transferring into 2θ angle scale.

In Figure 2-15, blue line comes from the standard PDF file of portlandite. Peaks in detected data match well with portlandite pdf file, which not only reveal the existence of calcium hydroxide in specimen, but also verify the correctness of energy to Cu Kα1 2θ angle conversion. It should be noted that signal from crystal face with Miller index (0 0 1) was not detected. This is due to absorption of low energy X-ray by specimen. As photons pass through matter, they can engage in photoelectric interaction with the material electrons. The photoelectric interaction captures all photon energy and deposits it within the material. At the lower photon energies, photoelectric interaction is more intense. For this reason, in the subsequent discussion of SPring-8 XRD, the focus will be on the range above 25°, and the corresponding energy threshold of X-ray is about 20 keV.

2.5 OTHER MEASUREMENT METHODS

As complementary measurement methods of integrated CT-XRD method, ICP-OES, powder XRD and TG-DTA method were also used in this research.

In the leaching test, hydrated products in specimen gradually dissolves into the solvent, manifesting as the release of calcium ions. In order to detect the amount of calcium ions released by the specimen in the leaching test, the replaced solvent obtained during the solvent exchange process was diluted 50 times, and then inductively coupled plasma optical emission spectrometer (ICP-OES) measurement was performed, as shown in Figure 2-16. Combining multiple measurements, the total amount of calcium ion released from specimen can be known.

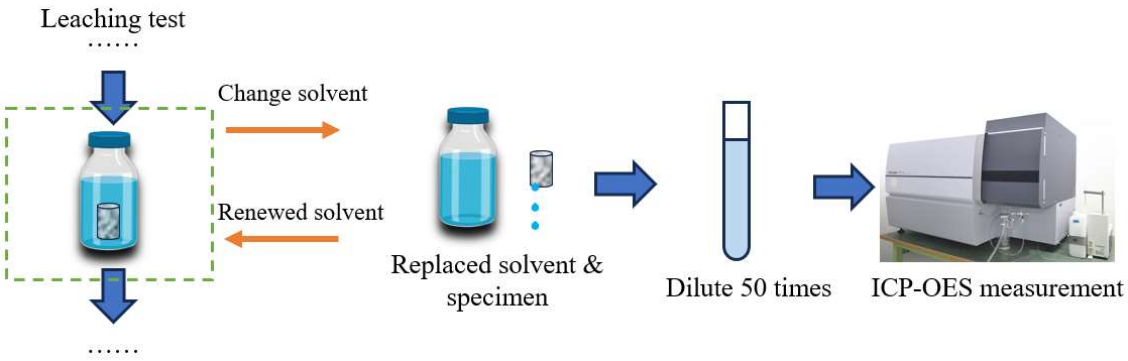

Figure 2-16 Solvent exchange and ICP-OES measurement

Synchrotron XRD is not suitable for detecting diffraction peaks in low energy region, i.e., in small 2θ angle region. As supplement and mutual confirmation, powder XRD and TG-DTA methods were also applied in this research. After the leaching test, the specimen was dried using acetone immersion and vacuum treatment. Subsequently, the dried specimen was ground with an agate mortar, and the fineness of the obtained powder sample was 125 μm. Then the powder specimen was analyzed by powder XRD and TGDTA respectively, as shown in Figure 2-17.

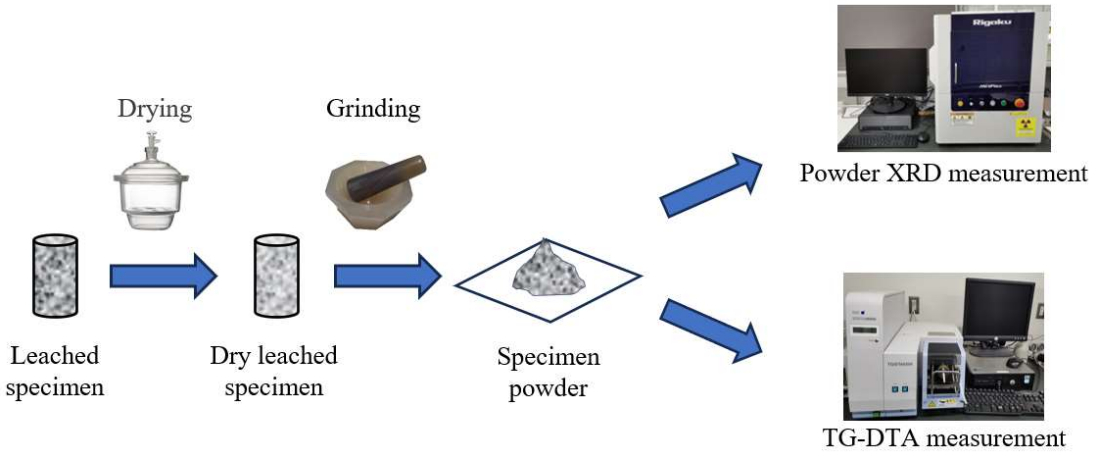

Figure 2-17 Powder XRD measurement and TG-DTA measurement

In powder XRD measurement, powder sample was placed on a glass slide and Cu Kα1 radiation was used as source. Measuring range of 2θ was set from 3° to 90°, and measuring speed was set as 10° per minute. In TG-DTA measurement, the heating rate was set as 10 ℃ per minute, and the powder sample was heated to 1000 ℃ eventually. During the entire heating process, the sample will be heated in a nitrogen-protected environment.

2.6 SUMMARY

In this chapter, experimental methods, and measurement of non-destructive integrated CT-XRD method were introduced. Basic operating methods such as specimen preparation, carbonation processing and leaching test involved in the test procedures were firstly introduced. Then, the CT-XRD method, which was the most important research method in this research, was described.

CHAPTER 3 METHODOLOGY OF IMAGE PROCESSING AND RANDOM WALK SIUMULATION

3.1 GENERAL

This chapter mainly introduced the image processing method and random walk simulation required for analyzing transport properties of specimen. The concept of pore structure under high-precision CT image was firstly introduced. Method of extraction of pore structure from high precision CT image stack was then described. To quantify the tortuosity of extracted pore structure, random walk simulation was introduced secondly.

3.2 EXTRACTION OF PORE STRUCTURE FROM CT IMAGES STACK

The porosity, pore distribution and morphology are important features of the cement-based materials pore structure which may have a significant impact on the macroscopic mechanical properties and durability performance [119]. The pore structure of cement-based materials has long been defined. It refers to the arrangement and characteristics of the voids or spaces within the matrix. Basing on the size of pore, the pore structure is mainly categorized into two types: capillary pores and gel pores. In leaching process, diffusion mainly occurs in capillary pores, whose size is ranging from 3-5μm for specimen with high water to cement ratio [36]. The CT scanning technology used in this research achieves an accuracy of approximately 2.5 μm per pixel, which can cover the size of capillary. This gives us the basis for analysis in the following process: through specific image processing methods, extracting the geometric structure from the CT image stack as pore structure and preforming analysis on it. What CT scanning gives us is the three-dimensional geometric information inside the specimen, or in other word, a stack of 8-bit images. How to obtain the pore structure from such a stack is the task of this section. It should be noted that although we use the term “pore structure”, the extracted structure is still not the real pore structure. It is only a structure that reflects some geometric characteristics of the pore structure.

A general process for extracting pore structure information from CT images includes: 1) Binary processing: using image processing techniques to separate the pore space from the solid matrix. 2) Labeling processing: labeling the whole pore space based on the concept of pore clusters. 3) Extraction: remaining the largest pore cluster as the pore structure.

3.2.1 Images stack and ROI

As shown in CHAPTER 2, the three-dimensional information of specimen is obtained in the form of images stack after CT scanning. In order to facilitate the description of data processing methods, this chapter will introduce an example for illustration. The water to cement ratio of this specimen was 0.5. Specimens had been cured for 28 days without any deterioration treatment, and CT imaging had completed in 2021-11. Labeling for

this specimen is “5N0d”. Resolution of this image is 2.31μm/pixel. Layer 0720 of this specimen is shown in Figure 3-1. In order to focus the analysis on the specimen, background and support results outside the specimen region are removed. In the image processing, in order to reduce computing time and avoid edge effect, more importantly, to investigate transport properties of certain region, it is necessary to extract specific region for processing, which is VOI (volume of interest). VOI is a three-dimensional region. The x-axis and y-axis range of the VOI are determined by selecting the ROI (region of interest) in one slice, while the z-axis range is selected by selecting the layers. Figure 3-2 shows selection of ROI in single slice, extraction of VOI and corresponding stereogram of VOI.

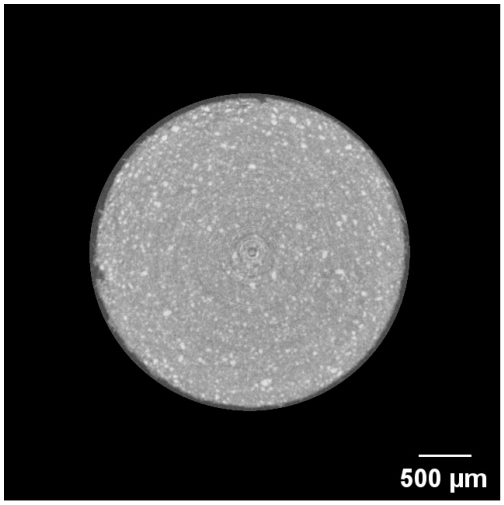

Figure 3-1 CT image of 5N0d specimen (layer 0720)

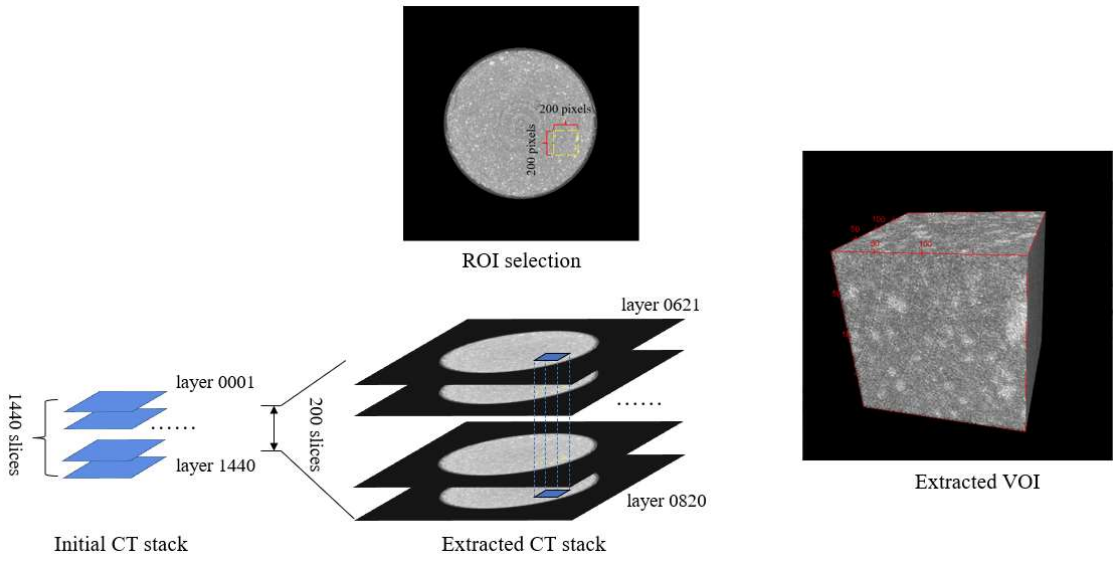

Figure 3-2 Extraction of VOI (200 × 200 × 200 voxels)

3.2.2 Binary process

As introduced in the CHAPTER 2, data of each pixel on 8-bit image (gray scale value) is converted from the 32-bit image, and data of each pixel on 32-bit image reflects the LAC (linear attention coefficient) of substance within corresponding pixel. Pixels with more pore phase or composed entirely of pore phase mean lower X-ray absorption and lower LAC. These pore phase will be darker (with lower gray scale value) in 8-bit image. This makes it possible to divide pore phases according to grayscale values of each pixel and then obtain the pore structure. In order to extract pore space from VOI, it is necessary to set a threshold basing gray scale value globally. The pixels with gray scale value below the threshold are set as pore, while the pixels with gray scale value above the threshold are set as solid phase. In the discussion of pore structure in this research, in order to highlight the pore structure, pixels of the pore phase are set to white (gray scale value = 255), while pixels of the solid phase are set to black (gray scale value = 0).

In regard to setting threshold, histogram is needed to introduce, as shown in Figure 3-3. A histogram of a grayscale image represents the distribution of pixel intensity values in the whole VOI region. Previous researchers have proposed some method for setting the threshold, but still lack a widely accepted method [120]. The threshold setting method used in this research is a global thresholding method based on gray scale value – porosity curve. Going through all the gray scale value from 0 to 255 and using each gray scale value as a threshold to calculate the corresponding porosity, the porosity to gray scale value curve can be obtained and it is overlayed in Figure 3-3. From the porosity curve, the transition point and inflection point can be seen. In this research, transition point is selected as threshold [121][122][115].

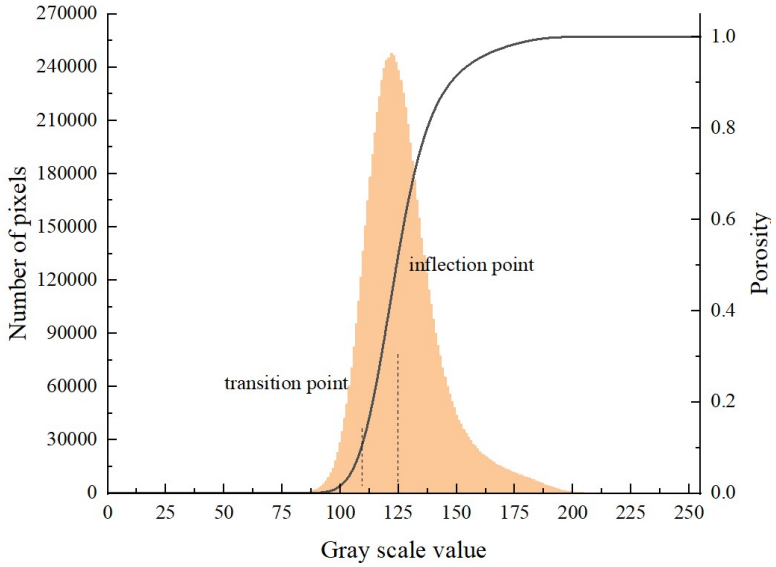

Figure 3-3 Gray scale value histogram of VOI and corresponding porosity curve

According to this method, the effect diagram obtained after applying binary process on VOI in Figure 3-2 is shown in Figure 3-4. Comparing original image in Figure 3-4 (a) and binary image in Figure 3-4 (b), it can be seen that the darker part in Figure 3-4 (a) turn into pore phase in white on Figure 3-4 (b), while the lighter part turn into solid phase in black on Figure 3-4 (b). The porosity of a certain VOI can be obtained by calculating the number of voxels in the pore space and comparing it with the total number of voxels in VOI. It should be noted that no matter which thresholding method is used, the minimum pore size of the pore space will not be smaller than the size of a single voxel of the CT image stack. In the description of this research, the geometric structure directly obtained by thresholding VOI is called pore space.

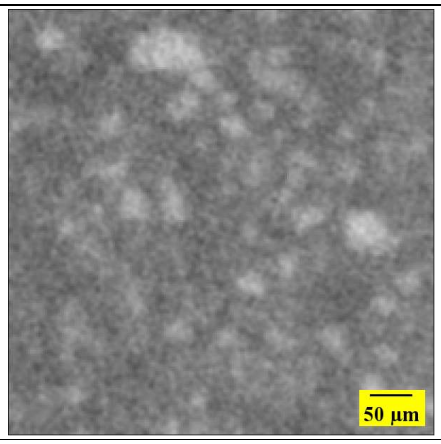

(a) Original image within ROI (layer 0720)

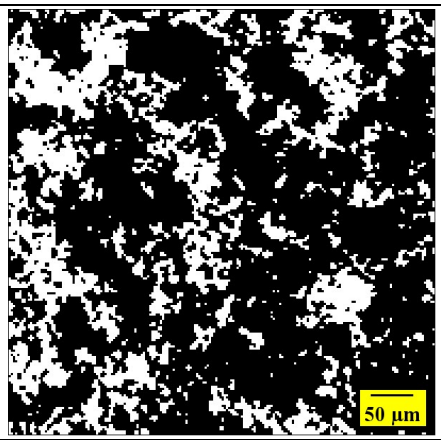

(b) Binary image (layer 0720)

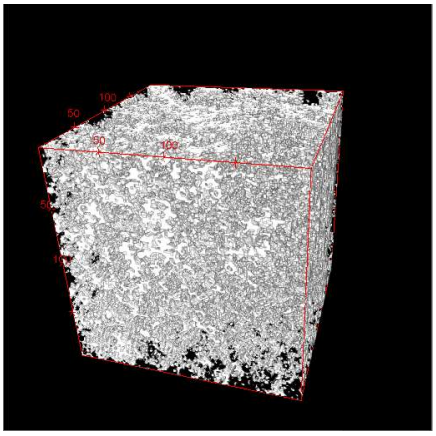

(c) Stereogram of binary image (layer 0621-0820)

Figure 3-4 Three-dimensional effect diagram of binary image

3.2.3 Pore cluster and labeling process

The pore space is the set of all pore phase within the VOI, but diffusion cannot occur freely between all pore phases. The pores inside the hardened cement paste have a geometric relationship of connected and isolated. In discussion of diffusion, for connected pores, we think that substances can diffuse freely in them, but in isolated pores, substances cannot diffuse freely due to solid phase obstacle. Similarly, in the pore space obtained in Figure

3-4, isolated pores also exist, which requires further analysis. For the convenience of explanation, regardless of whether the z-axis is connected or not, the binary image of layer 0720 is used for discussion in two-dimension, as shown in Figure 3-5. Three-dimensional analysis can be generalized based on the process of two-dimensional analysis.

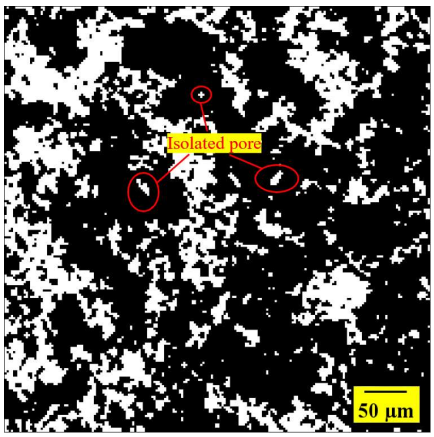

Figure 3-5 Isolated pore in extracted pore structure (2D, layer 0720)

Free diffusion cannot occur between isolated pores due to solid phase obstacle. To analyze the diffusion of substances in interconnected pores, it is necessary to remove the effect of isolated pores, and it must firstly introduce the concepts of "connected" and "pore clusters" in pore space. In two dimensions, two pore pixels are considered to be "connected" if they share the same edge. In the case of three dimensions, it requires two voxels share one same face. Therefore, in two dimensions, a pixel has at most four pixels connected to it (up, down, left, and right), while in three dimensions, a voxel has at most six pixels connected to it (up, down, left, right, front, and behind). A pore cluster is a set of all connected pores and pore space contains multiple pore clusters. Except for the pore cluster with the largest area (or volume in case of three dimension), the other clusters are called isolated pores [123][124][129].

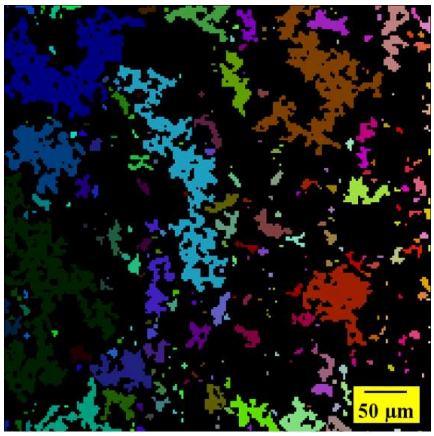

Figure 3-6 Division of pore cluster in two dimensions

The process of assigning a unique number of each pore clusters in pore space is called cluster labelling. Theory required for cluster labeling has long been established. The function that come with some mathematical software can perform pore cluster labeling according to connectivity and assign a unique number for every pore cluster, like function “bwlabel” in MATLAB. Figure 3-6 shows the division of pore cluster based on the four connected regulation in two dimensions, each color represents a single pore cluster.

The area (or volume) of each pore cluster can be obtained by counting number of pixels (or voxels). The effect of isolated is eliminated by retaining only the pore cluster with the largest area (or volume). Figure 3-7 shows the application of this operation in three dimensions. Figure 3-7 (a) shows pore space of VOI shown in Figure 3-4 (c), while each color in the Figure 3-7 (b) represents a pore cluster. Figure 3-7 (c) shows the largest pore luster, or in other word, pore structure of VOI. The pore cluster with the largest area or volume is used as the pore structure because it has the greatest influence on diffusion.

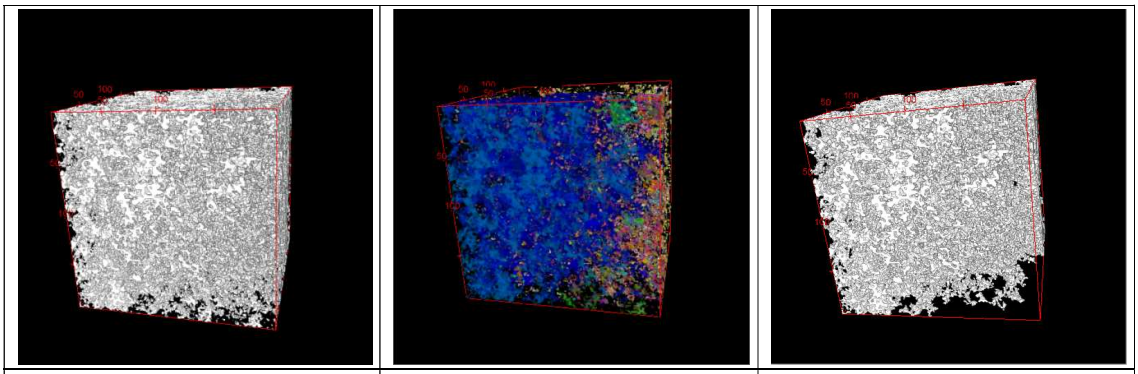

(a) Original pore space | (b) Labeled pore structure | (c) Largest pore cluster

Figure 3-7 Pore cluster labeling process and extraction of largest pore cluster in three dimensions

3.2.4 Expansion

The expansion mentioned here refers to expanding the extracted pore structure to the required size. The need to expand the pore structure mainly comes from two aspects: 1) For more accurate analysis, the scale of the frame selected VOI may be small. 2) Algorithms applied for subsequent analysis may require larger regions.

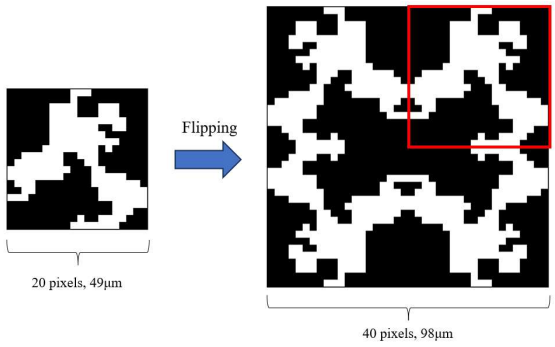

Figure 3-8 Schematic diagram of expanding ROI by flipping

Expansion process of pore structure needs to preserve the geometric information of pore structure while ensuring the connectivity on the interface remains unchanged. An image operation that satisfies the above requirements is flipping and stitching images. Here we take the expansion of frame-selected ROI on a CT image as an example to illustrate. Figure 3-8 (a) shows extracted ROI while Figure 3-8 (b) shows extended ROI obtained after two mirror flips. It can be seen that the expanded pore structure doesn't not change the pore structure (each small area is a copy of the original area), while ensuring the connectivity on the boundary [131].

The same mirror operation can also be applied to the three-dimensional pore structure. At this time, there are six mirror operation directions (front, back, left, right, up, and down). Figure 3-9 (b) shows a pore structure with size of 400 × 400 × 400 expanded from Figure 3-9 (a). Such an expansion operation allows us to expand the pore structure of any size to any required size without changing its geometric properties. This is also the premise for further analysis of the pore structure.

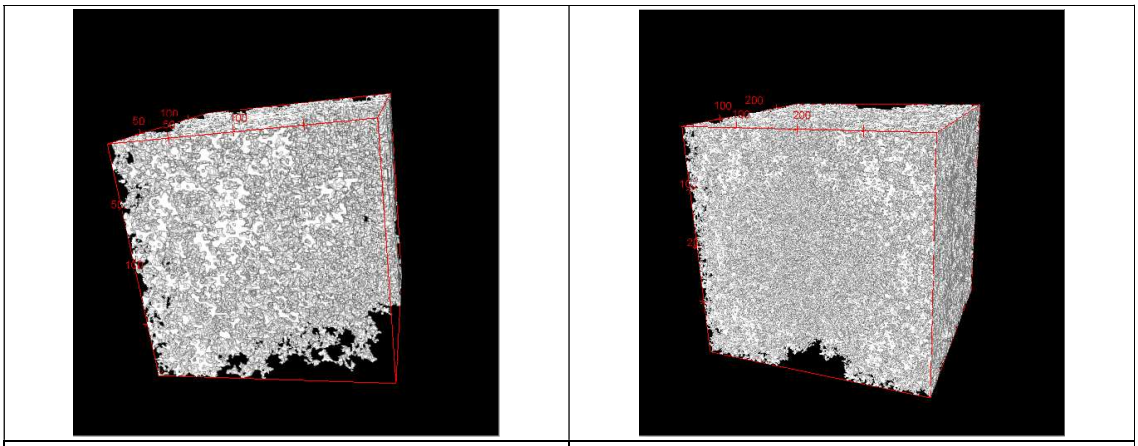

(a) original pore structure (200 × 200 × 200) | (b) expanded pore structure (400 × 400 × 400)

Figure 3-9 Expanded pore structure in three dimensions

3.3 TORTUOSITY CALCULATION BY RANDOM WALK ALGORITHM

Tortuosity refers to the degree of irregularity or winding in a path, trajectory, or shape [128]. It is a measure of how much a route deviates from being straight or direct. Although tortuosity is an important parameter for quantifying pore structure, how to mathematically define the tortuosity of the three-dimensional pore structure has always been a difficult problem. Some studies have estimated tortuosity through image analysis and simulation methods [125][126][127][128][129][130]. Tortuosity refers to the ratio of diffusivity in free space to diffusivity in a porous medium. There is a basic idea, which is to find a method to simulate diffusion process, apply it to free space and pore structure, and then calculate the tortuosity. Microscopically, Brownian motion serves as a microscopic model for diffusion at the molecular or particle level. When molecules or particles move randomly due to Brownian motion, they collectively contribute to the macroscopic process of diffusion. From the perspective of non-absorbing diffusion of substance, it is a feasible method to investigate the Brownian motion difference of

substances in free space and pore space and calculate the tortuosity from this difference. Mathematically, Brownian motion can be considered a limit of a random walk as the step size becomes infinitesimally small, the number of steps becomes infinitely large, and the time between steps approaches zero. In other words, Brownian motion is a continuous-time random walk in the limit. As mentioned above, the diffusion process is represented by the random motion of substance on the microcosm, which gives us an inspiration that the random walk algorithm can be used to simulate the diffusion process [131][132][133].

The concept of random walk was first proposed by Karl Pearson in 1905 [134]. A random walk simulation is a computational model used to describe and simulate the random movement or trajectory of particles or entities as they move through a medium or space. It is a stochastic process in which the future position of a particle is determined by probabilistic rules, typically involving random steps or changes in direction. Random walk simulations are used in various fields, including physics, mathematics, biology, and economics, to study and understand processes characterized by randomness and uncertainty [135]. In this research, random walk is used to simulate the diffusion of non-sorbing species in the pore structure. The emphasis on "non-sorbing" here is because the purpose is to calculate the tortuosity of the three-dimensional pore structure and the undesirable effects of the sorbing of species on the solid surface should be eliminated.

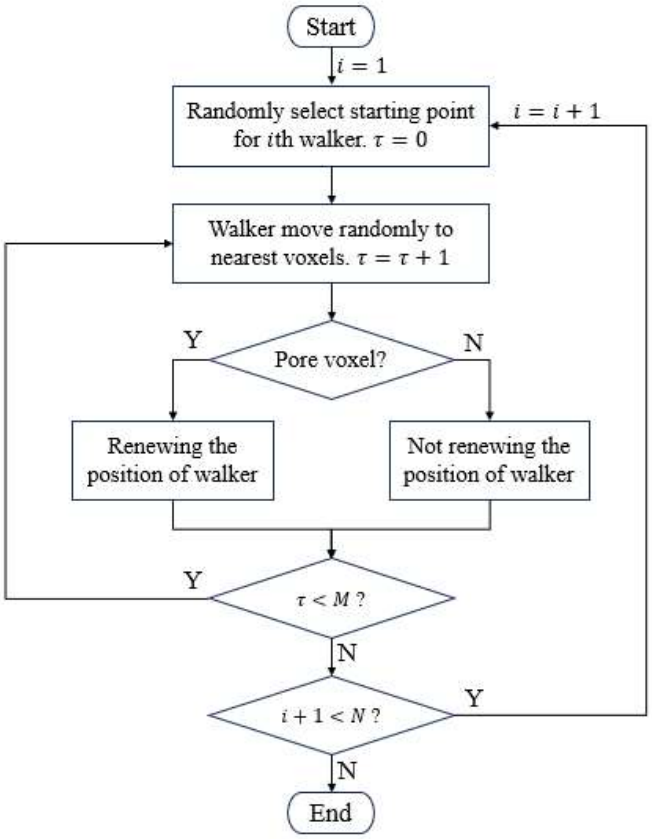

Figure 3-10 Flow diagram of random walk simulation

The random walk algorithm in pore structure is roughly described as follows [131]:

1) Starting point (starting voxel) of first walker is selected randomly from among the whole pore structure in VOI at $\tau = 0$, where τ is the dimensionless integer time, or steps of walker.

2) The walker executes a random motion to the nearest voxels. The "nearest voxels" here is consistent with the concept of "connected" mentioned above, which means that a pore voxel has at most six nearest voxels in three dimensions. τ is increased by a unit after the motion, becomes $\tau + 1$. If the random motion of walker happens to go to a solid voxel, this motion is considered invalid and walker stay in the original pore voxel, but the time still becomes $\tau + 1$.

3) When the time τ reaches a certain value, end the random walk of this walker [131][136]. As mentioned in section 3.2 , the pore structure can be expanded until it fills the entire space, so there is no need to consider the situation that the walker reaches the boundary.

4) Starting the random walk of the next walker. To fully reflect the geometry of the pore structure through the random walks, one walker alone is not enough. In the program, the parameter N will be set as the number of walkers. N mainly depends on the discreteness of mean square distance of walkers. When the mean square distance of walkers is stable enough, we consider N to meet the requirements.

5) Program ends when all walkers finish their random walk.

Figure 3-10 shows flow diagram of random walk simulation. For free space, it can regard as a pore structure with a porosity of 1, and the same random walk algorithm can be applied. Figure 3-11 shows a trajectory of single walker in free space with steps of 10000.

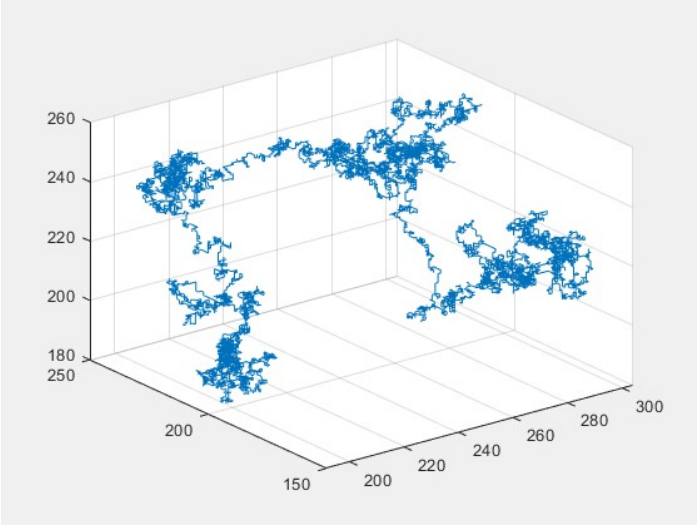

Figure 3-11 Trajectory of single walker in free space (M = 10000)

The main output of random walk algorithm is the mean square displacement (MSD) of walkers. It is the average walking distance of all walkers in the same simulation time in a random walk simulation, and it can be calculated as eq (3-1):

$$\langle r(\tau)^2 \rangle = \frac{1}{n}\sum_{i=1}^{n}[(x_i(\tau) - x_i(0))^2 + (y_i(\tau) - y_i(0))^2 + (z_i(\tau) - z_i(0))^2] \quad (3\text{-}1)$$

In which, n is the number of walkers. $x_i(\tau)$, $y_i(\tau)$ and $z_i(\tau)$ are the 3-D coordinates of ith walker's position at time τ.

It should be noted that the concept of "distance" used in this research is not the more intuitive Euclidean distance. The use of mean square distance is determined by the characteristics of the data form of image stack and the logic of the random walk algorithm. The six-connected characteristics between voxels makes it impossible to have a shortest path even in the free space, making the path length equal to the Euclidean distance, as shown in Figure 3-12.

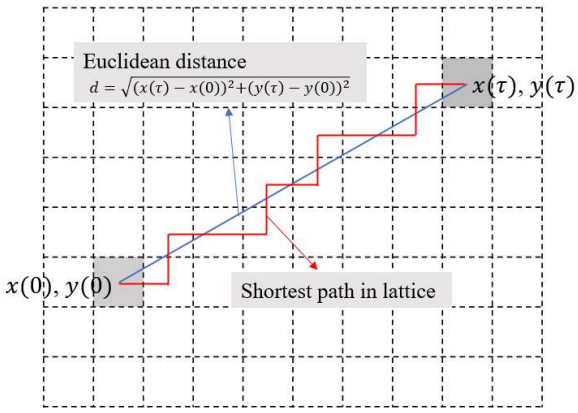

Figure 3-12 Euclidean distance and shortest path in lattice

The use of Euclidean distance does not accurately reflect the hindrance of the pore structure to the walkers compared to the free space, and it cannot reflect the tortuosity of the pore structure. Therefore, in random walk simulation in this research, mean square distance is selected as the scale of random walk.

As random walk simulates diffusion process, from the perspective of diffusion of walkers, MSD in free space can also be calculated by eq (3-2) [137][138]:

$$\langle r^2 \rangle_{free} = 6D_0 t = a^2 \tau \quad (3\text{-}2)$$

In which, t is diffusion time. D_0 is diffusion coefficient of walker in free space without solid phase. It should be noted that the diffusion coefficient mentioned here is to calculate tortuosity of pore structure and it is a mathematical concept rather than the diffusion coefficient in the real diffusion process. The "6" in the eq (3-2) is because there six moving directions of walkers (± x, ± y, ± z). As an example, the number is "4" in the case of using the four-connected rule in a two-dimensional pore structure. τ is time in random walk simulation. a is constant lattice parameter, which is related to the physical size of lattice and the real physical time represented by τ. Here, we will not discuss the parameter a in detail, because in the process of calculating the tortuosity, the

parameter a will be eliminated in the comparison of random walk simulation in pore structure and in free space.

When performing random walk simulation in a three-dimensional pore structure, trajectory of walkers is restricted and $\langle r^2 \rangle$ is reduced due to the obstruction effect of solid phase. The degree of reduction enables to quantify tortuosity of pore structure. In random walk simulation, the diffusion coefficient in pore structure can be calculated as eq (3-3):

$$D(t) = \frac{1}{6}\frac{\mathrm{d}\langle r^2 \rangle}{\mathrm{d}t} \tag{3-3}$$

The tortuosity of the pore structure is defined as the limiting value of the ratio of D_0 in free space to $D(t)$ in the pore structure, as shown in eq (3-4) [47][156]:

$$\tau_p = \frac{D_0}{D(t)} = \left[\lim_{\tau \to \infty} \frac{\mathrm{d}\langle r^2(\tau) \rangle}{\mathrm{d}\tau}\right]^{-1} \tag{3-4}$$

Figure 3-13 (a) shows trajectory of 100 walkers in free space while Figure 3-13 (b) shows trajectory in pore structure. Each color represents one trajectory of single walker.

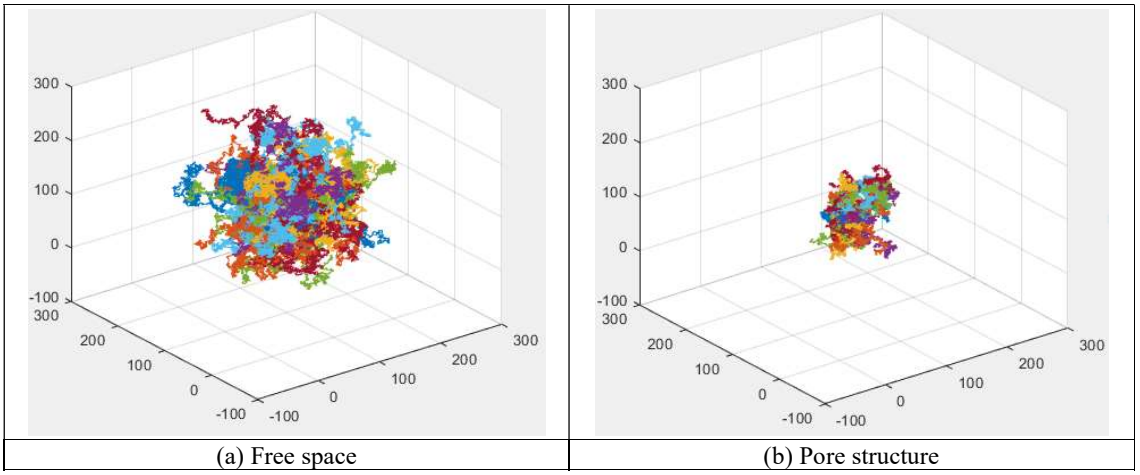

(a) Free space (b) Pore structure

Figure 3-13 Trajectory of walkers (N = 100, M = 10000)

By comparing Figure 3-13 (a) and Figure 3-13 (b), it can be clearly seen that the trajectory of walkers in the pore structure is constrained by the solid phase. By stating the MSD data of walkers in free space as well as in pore structure, the obstruction of solid phase on walkers' trajectory in pore structure can be quantitatively seen. Figure 3-14 shows the MSD of walkers at different steps for free space and pore structure.

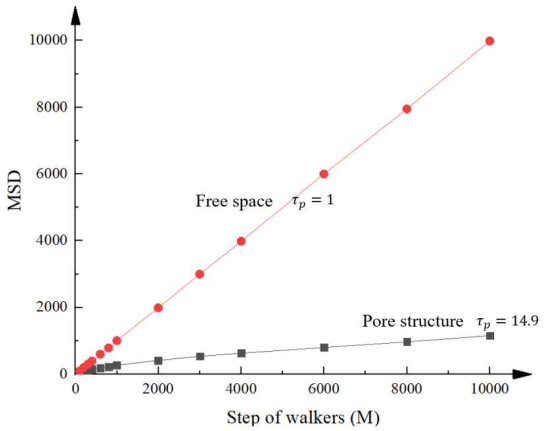

Figure 3-14 MSD of walkers at different steps for free space and pore structure

Basing eq (3-4), tortuosity of this pore structure is calculated as τ_p=14.9. Tortuosity calculated from eq (3-4) require τ approaching infinity. Although the expansion of the pore structure allows us to conduct random walk simulation with any number of steps, the limitation of computer performance do not allow us to do so. This requires the establishment of a standard so that τ can be approximately regard as infinity when it reaches the value M, or in other word, steps of walkers. Theoretically, the value M should be related to the following factors: 1) Size of selected VOI. The calculation of the tortuosity by random walk algorithm is essentially to measure the whole pore structure in selected VOI through walkers. When the trajectory of walkers exceeds the original VOI by a large amount, it's not meaningful to continue the simulation, because the extended part is just a copy of the initial part. 2) How easy it is for the movement of walkers. For pore structure with low porosity, low connectivity and high tortuosity, there may be case where the MSD of walkers is still very small (comparing with the size of the selected VOI) even if τ is very large. Based on the above situation, in the subsequent discussion of this research, when the MSD-step curve changes periodically or shows a linear relationship, we think that τ is large enough [47].

3.4 SUMMARY

This chapter introduced the image processing method and random walk simulation required for further analyzing transport properties of specimen. Method of extracting pore structure through binary process and clusters labeling process is firstly introduced. Secondly, to quantify the extracted pore structure, tortuosity was introduced and calculated by random walk simulation. The random walk algorithm simulates the Brownian motion of substances, thereby simulating the diffusion process. The difference of mean square distance of walkers in free space and in pore structure quantifies tortuosity of pore structure.

CHAPTER 4 STUDY OF ALTERATION OF CEMENT HYDRATED SYSTEM AND THE ROLE OF ITZ

4.1 GENERAL

The focus of this chapter is mainly on how to use the information measured from CT-XRD method as well as random walk algorithm to practically evaluate the transport properties of leaching altered cement-based materials, especially the transport properties of ITZ. Non-accelerated leaching experiments in deionized water of three kinds of specimen and leaching experiment in seawater of one kind of specimen were carried out in this chapter. The first is the long-term (up to 120 days) leaching experiment in pure water for plain hydrated cement paste at a controlled temperature. The second is the aggregate containing non-accelerated specimens leaching at different temperatures (20 ℃ and 80 ℃) in pure water. The third is pure water leaching experiment for carbonated plain cement paste. The last is leaching experiment for non-carbonated specimen in modulated seawater. The analysis on the pure water leaching of plain cement paste reveals the general characteristics of leaching deterioration, clarifies the phase transition that occur under leaching, and gives the concepts of leached region and non-leached region. In the analysis on single aggregate containing specimen, an original image processing method was applied to analyze the ITZ. Under this method, transport properties of leached region, non-leached region and ITZ were quantitatively evaluated on basis of obtained CT images. Analysis of carbonated specimen quantifies the influence of carbonation process on the transport properties of specimen.

4.2 EXPERIMENTAL RESULTS

4.2.1 CT images of each kind of specimen

(1) Leaching test on plain cement paste

Plain hydrated cement paste specimens were used in this section. Ordinary Portlandite cement was used with a water to cement ratio of 0.6 and 0.5. preparation and curing of specimen are as described in section 2.2 , only the process of inserting single aggregate is removed. All specimens started the leaching test together. According to the water to cement ratio, specimens were divided in to “5N” and “6N” series. “N” for normal, means the specimen has not undergone special processing. Every time a specific time elapses, one specimen was taken out from each series for dehydration and vacuum storge. In this experiment, the time point for taking out the specimen is 7 days, 15 days, 60 days, and 120 days after the start of leaching experiment. All specimens obtained at the end were taken to SPring-8 for preforming CT-XRD measurements. According to the leaching period, each specimen was further named as 5N7d, 5N15d, 5N60d, 5N120d; 6N7d, 6N15d, 6N60d, 6N120d, “d” here represents days. Test procedures of non-carbonated plain specimen is shown in Figure 4-1. Figure 4-2 and Figure 4-3 show CT images for specimens with water to cement ratio equal to 0.5 and 0.65 respectively.

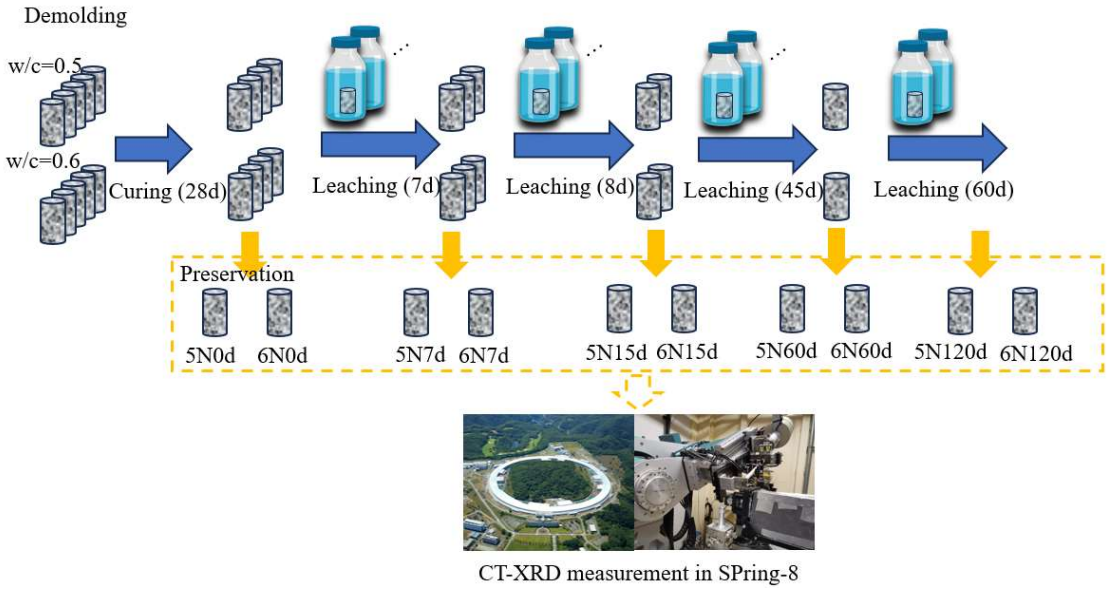

Figure 4-1 Test procedure of non-carbonated plain specimens leaching in pure water

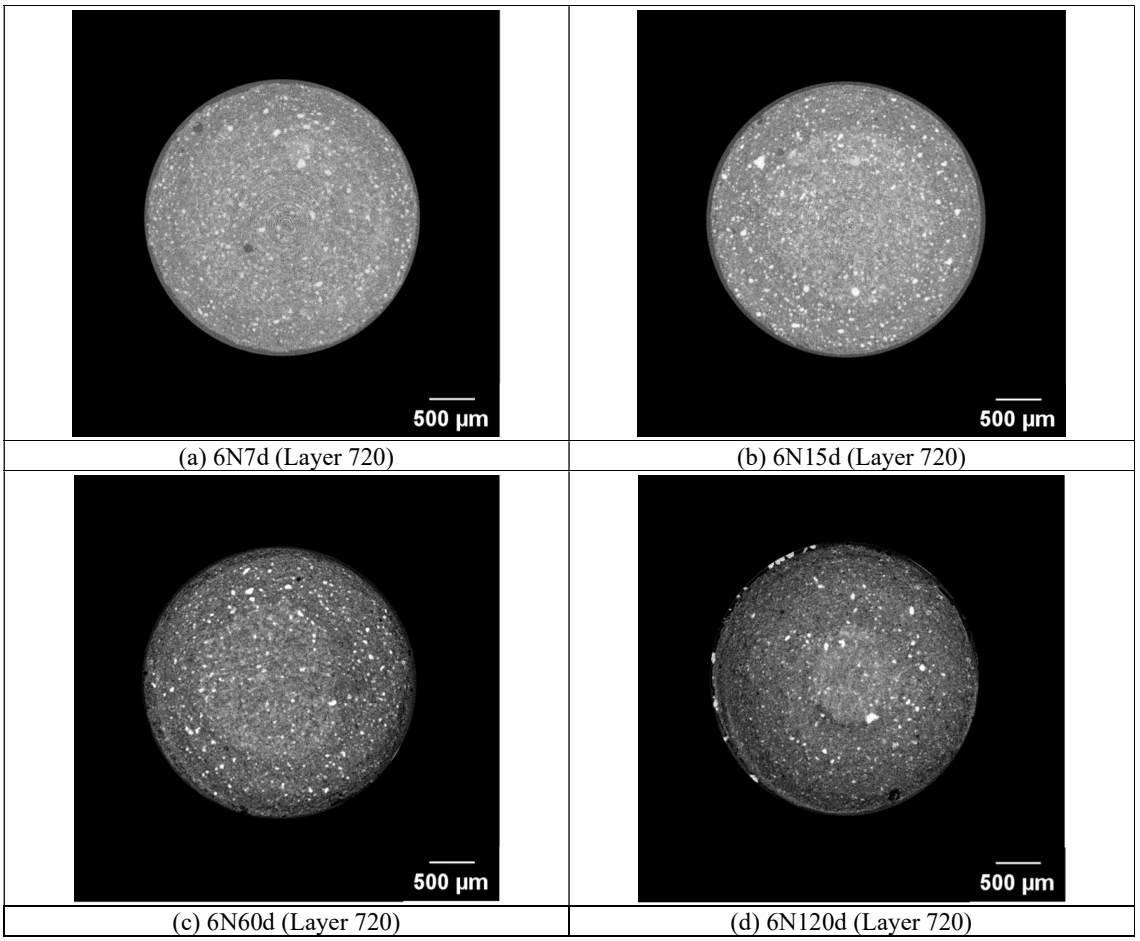

(a) 6N7d (Layer 720) (b) 6N15d (Layer 720)

(c) 6N60d (Layer 720) (d) 6N120d (Layer 720)

Figure 4-2 CT image of specimens with w/c=0.6, under pure water leaching

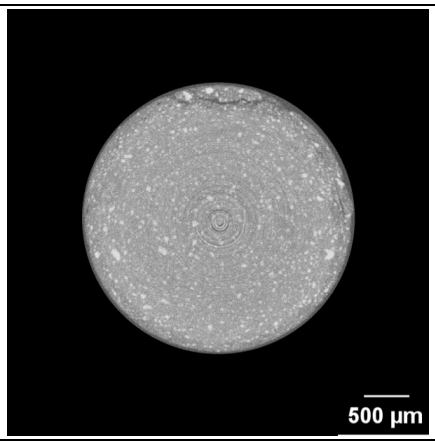

(a) 5N7d (Layer 720)

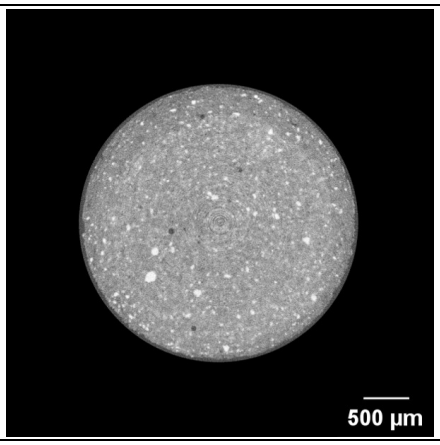

(b) 5N15d (Layer 720)

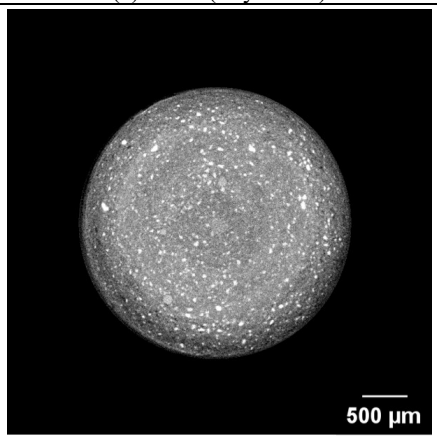

(c) 5N60d (Layer 720)

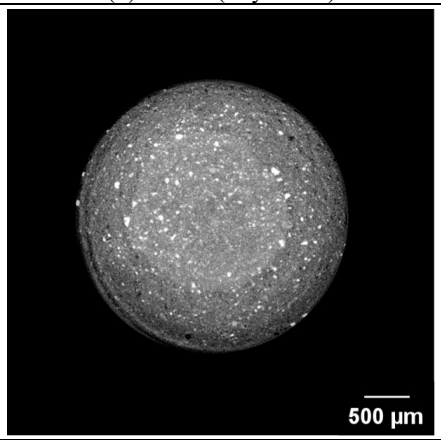

(d) 5N120d (Layer 720)

Figure 4-3 CT image of specimens with w/c=0.5, under pure water leaching

(2) Leaching test of single aggregate containing specimen

Cement paste was used for this section. Ordinary Portland cement was used with a water to cement ratio of 0.5. A cylindrical plastic mold with 3 mm in diameter and 6 mm in height was used. A piece of limestone is inserted as an aggregate to the fresh cement mixture at the same time as the mould. After 24 hours of curing in the mold, demolding, and then curing in a constant temperature room until 28 days. The above preparation of specimen and curing are detailed introduced in section 2.2 . Subsequently, non-accelerated leaching test was carried out. In the leaching test, each specimen was placed in a plastic bottle. After leaving the specimen in the bottle for a specified number of days, the solvent was removed. The same volume of fresh solvent was immediately poured back into the bottle, repeating the leaching process until 33 days. Leaching experiments were performed at 20 ℃ and 80 ℃ respectively. According to the temperature of leaching test, specimens are named as 5LN20c and 5LN80c respectively. “L” here represents limestone (as aggregate) while “c” here represents Celsius. After leaching test, CT-XRD measurements were conducted. Figure 4-4 shows the test procedures of single aggregate containing specimens, and Figure 4-5 shows CT image of specimens:

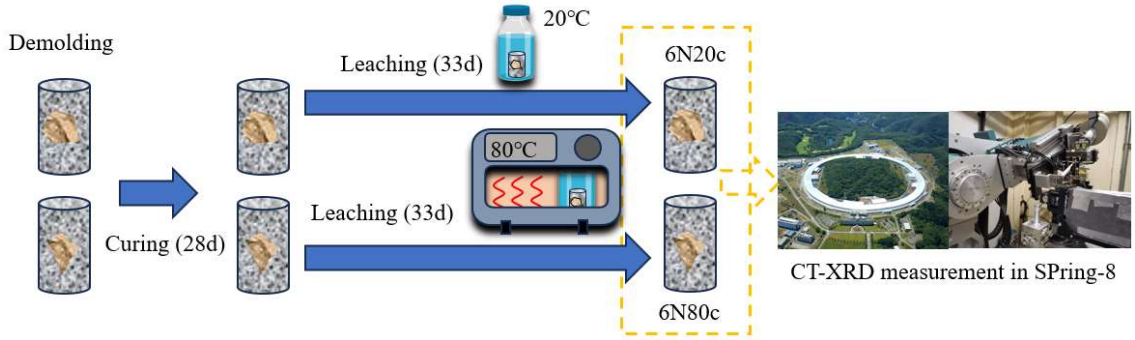

Figure 4-4 Test procedure of single aggregate containing specimens

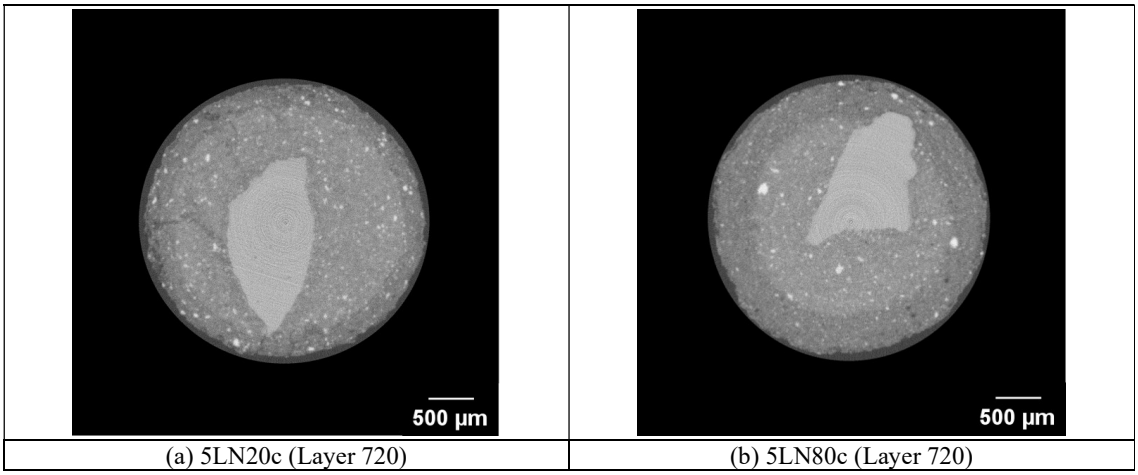

(a) 5LN20c (Layer 720) (b) 5LN80c (Layer 720)

Figure 4-5 CT image of 5LN20c and 5LN80c specimens

(3) Leaching test on carbonated cement paste

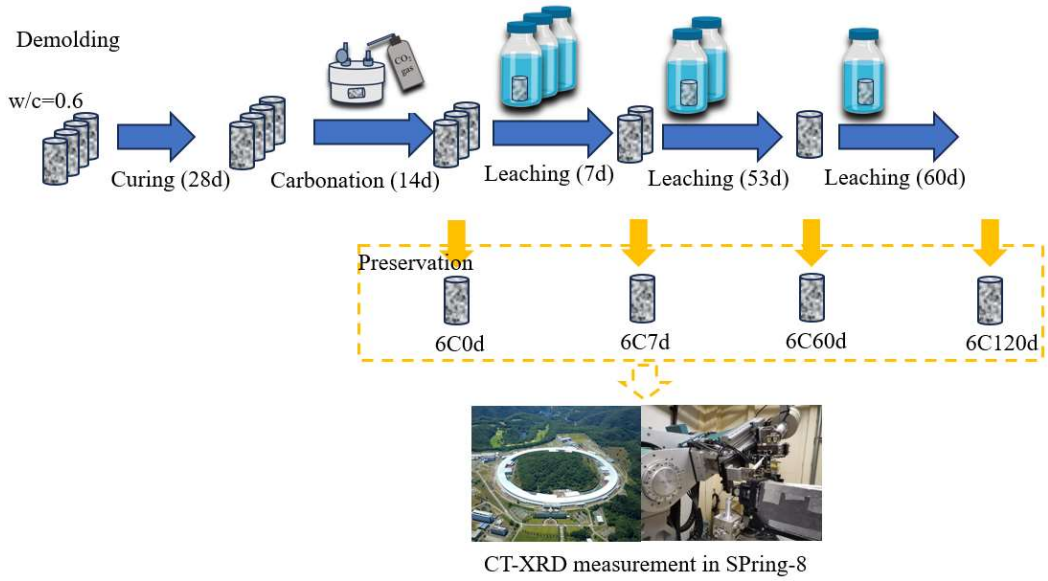

Figure 4-6 Test procedure of carbonated specimens

Plain cement paste was used in this research. Ordinary Portland cement was used with a water to cement ratio of 0.6. Preparation and curing are the same as described in the 2.2 . After curing, specimens were subjected to two weeks accelerated carbonated process, and detail method is shown in 2.3 . Carbonated specimens were subsequently subjected to leaching test, and carbonized specimen with different leaching period were obtained. Test procedure is shown in Figure 4-6.

Here, carbonized specimens after 7 days, 60 days and 120 days of leaching period were subjected to CT-XRD measurement. According to the water to cement ratio and leaching period, specimens are named as 6C7d, 6C60d, and 6C120d respectively, here "C" represents carbonation. Figure 4-7 shows CT images for these specimens:

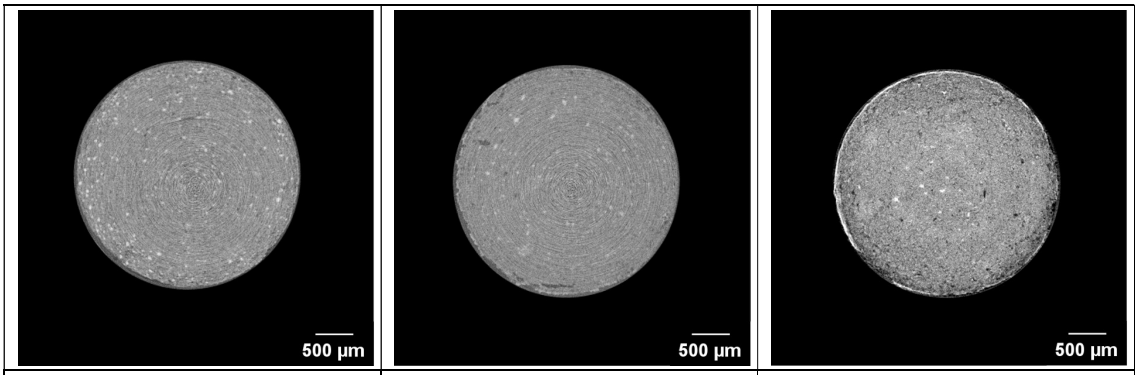

(a) 6C7d (Layer 720)	(b) 6C60d (Layer 720)	(c) 6C120d (Layer 720)

Figure 4-7 CT image of carbonated specimens with w/c = 0.6

(4) Leaching test under seawater environment

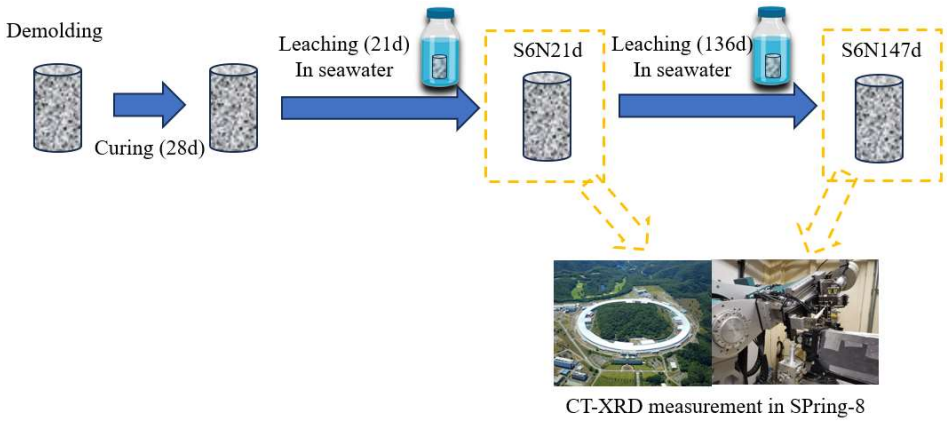

Figure 4-8 Test produce of specimens leaching in modulated seawater

Seawater can have a significant effect on leaching processes when it comes into contact with cement-based materials. In order to study the influence of ionic environment on leaching process, leaching test of specimen in modulated seawater was conducted. Cement paste with only the ordinary Portland cement was used. A water to

cement ratio is 0.6. Size of cylindrical specimen is 3 mm in diameter and 6 mm in height. The specimen was cured for four weeks after demolding. A detailed description of specimen preparation, curing are provided in section 2.2. Specimens were named following the labeling rule of "S" + "water to cement ration" + "type" + "leaching period". Test procedures of specimen leaching in modulated seawater is shown in Figure 4-8.

4.2.2 Phase transition under leaching in different solvent and carbonation

(1) Dissolution front

Figure 4-9 shows the CT image of 5LN20c specimen, and with the following markings: dissolution front (in blue), labeled line a-b (in red) and XRD data points. Corresponding gray scale change along labeled line is shown in Figure 4-10. According to gray scale value difference, three regions can be seen. In the order from a to b, temporarily name these three regions as region 1, 2 and 3. The shape of the aggregate is very clear in CT image, and thus, region 3 is aggregate. According to the gray value difference between region 1 and region 2, a clear boundary line (in blue) can be drawn on the CT image, and the shape of this boundary line is basically concentric circles. In order to clarify the specific physical and mineralogical meaning of region 1 and region 2, it is necessary to add XRD data for discussion.

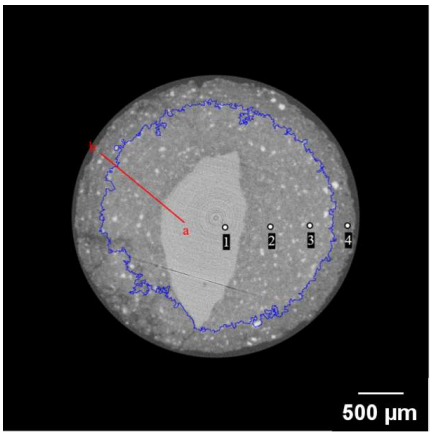

Figure 4-9 CT image of 5LN20c specimen (layer: 0720)

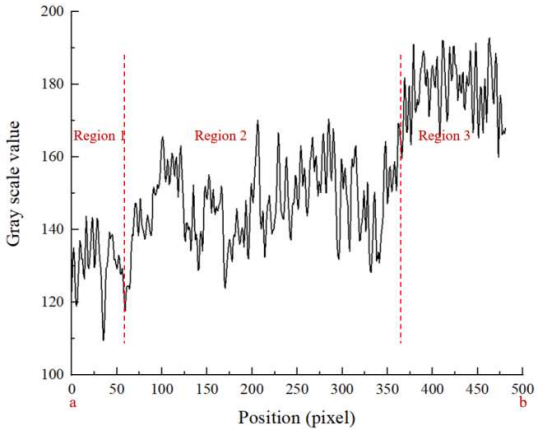

Figure 4-10 Line profile of labeled line a - b

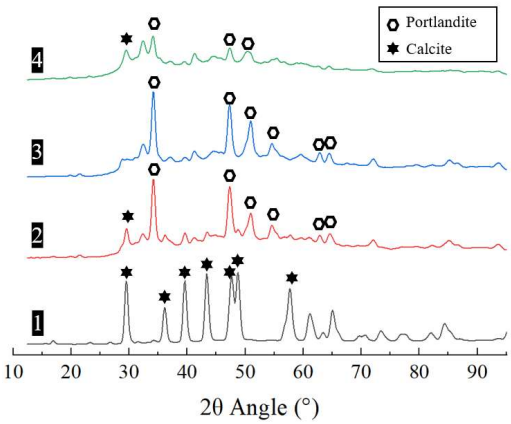

Figure 4-11 XRD data of 5LN20c specimen

Figure 4-11 shows XRD data for each selected point. Point 1 locates inside the aggregate, point 2 and point 3 locate on region 2, and point 4 locates on region 1. It can be seen that the XRD data for points located inside the boundary line show a clear signal from portlandite, while for point located outside the boundary, signal from portlandite weaker significantly. This shows that the decrease in gray scale value at region 1 is due to the decrease in portlandite content, and thus the boundary line between region 1 and region 2 can be named as dissolution front (of portlandite).

The same method can be used to find the dissolution front of portlandite in plain hydrated cement paste. Figure 4-12 (a) shows CT image of 6N60d specimen, with the marking of dissolution front of portlandite, in yellow line and position of XRD datapoint. Figure 4-12 (b) shows the corresponding XRD data. It can be seen that for point inside the front, signal from portlandite is detected while for point outside the front, it is not the case.

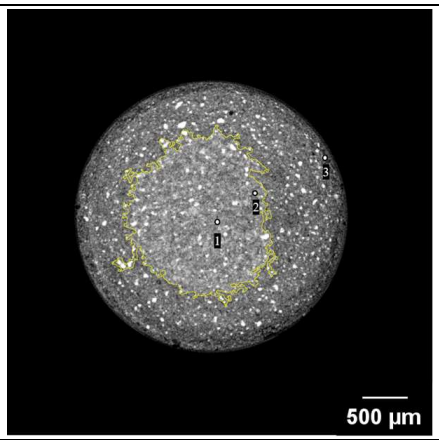

(a) CT image of 6N60d (layer: 0720)

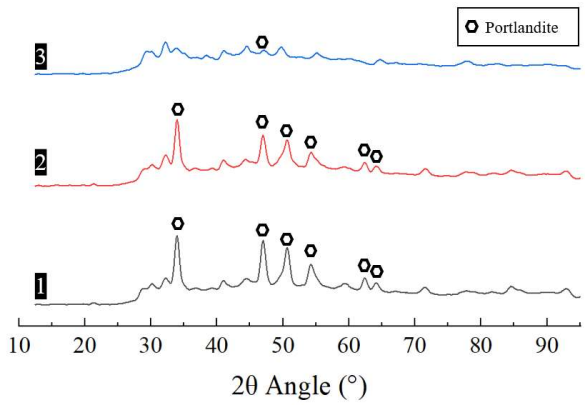

(b) XRD data for 6N60d

Figure 4-12 Dissolution front for non-carbonated specimen after 60 days leaching (6N60d specimen)

(2) Effect of carbonation

Carbonation of cement paste is a chemical reaction and deterioration process that occurs in concrete and other cement-based materials over time. It involves the reaction between carbon dioxide (CO_2) from the atmosphere and the portlandite ($Ca(OH)_2$) present in the hydrated cement paste. Figure 4-13 and Figure 4-14 show CT-XRD result of plain, non-leached specimens without carbonation and after two weeks of accelerated carbonation respectively. In order to analyze the effects of carbonation, these specimens were not subjected to leaching test. Figure 4-13 (b) and Figure 4-14 (b) show corresponding XRD data of each point. It can be seen that XRD data of non-carbonated specimen show clear peak match well with portlandite, while for XRD data of carbonated specimen shows clear peak match well with calcite. This shows that during the accelerated carbonation process, portlandite is converted into calcite. It should also be noted that in the carbonated specimen, the signal from portlandite can still be detected, which may come from portlandite that has not been carbonated.

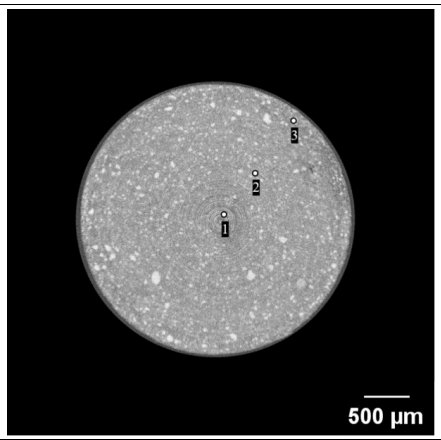

(a) Non-carbonated specimen 6N0d (layer: 0720)

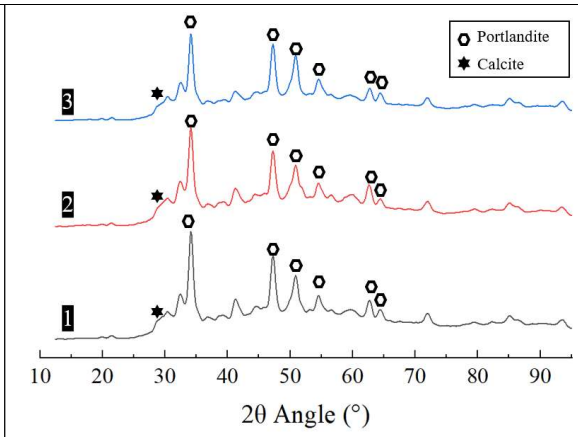

(b) XRD data for 6N0d

Figure 4-13 CT-XRD result of 6N0d specimen

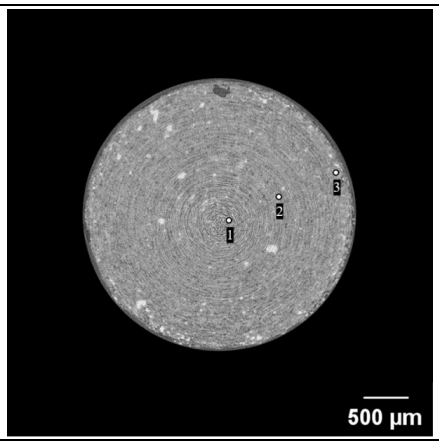

(a) Carbonated specimen 6C0d (layer :0720)

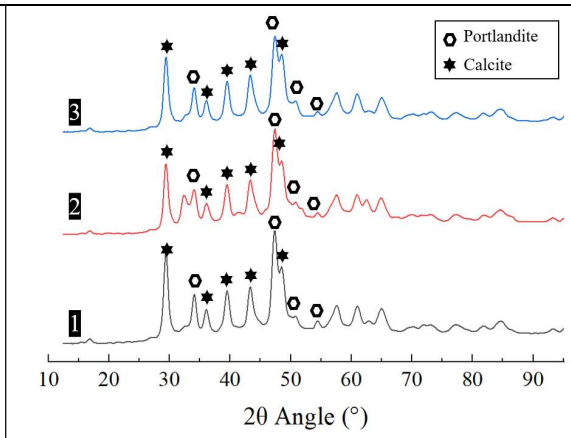

(b) XRD data for 6C0d

Figure 4-14 CT-XRD result of 6C0d specimen

In order to study the impact of the carbonation process 6N0d and 6C0d specimens were ground into powder for the powder XRD measurement, Figure 4-15 shows powder XRD data for both 6N0d and 6C0d respectively. Compared with the synchrotron XRD, powder XRD measurement can detect diffraction peaks in low 2θ regions. However, as a destructive detection method, powder XRD may introduce interference of carbonation factor during the sample preparation stage. Therefore, for 6N0d specimen, signal from calcite is stronger in powder XRD measurement. Both for synchrotron XRD and powder XRD measurement, the peaks of portlandite (CH) can be detected both before and after carbonation process, which indicates that the carbonation was not completed and there was still portlandite remaining.

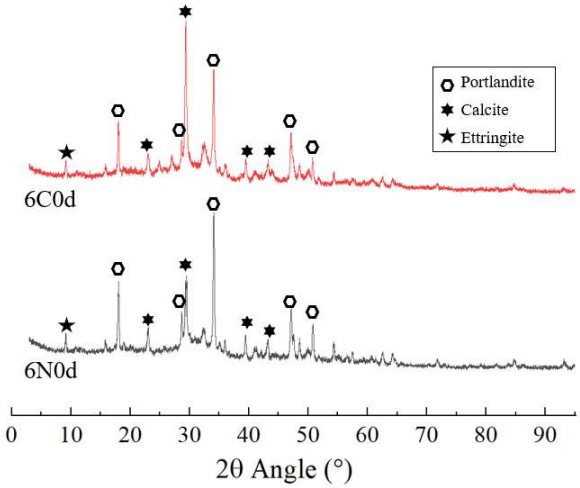

Figure 4-15 Powder XRD data of specimens with or without carbonation before leaching test (6N0d and 6C0d)

The carbonation process of cement-based materials can be regarded as the combination of carbon dioxide penetrating into the matrix and the reaction of carbon dioxide and hydrated component. Under unpressurized conditions, carbon dioxide enters the matrix in the form of diffusion. The concentration of carbon dioxide in the

air is only 0.04 %, so the natural diffusion rate of carbon dioxide in concrete is very low. In order to accelerate the carbonation process, the carbon dioxide concentration is generally increased to reach a deeper carbonation front in a short time [139]. Sanjuán reported that after 5 days exposed to 100 % carbon dioxide, carbonation depth was around 15 mm in concrete with water to cement ratio equal to 0.5 [139]. Hongzhi reports under 90 % of CO2 concentration and 14 days exposure, carbonation depth is evaluated as 15 mm [71]. For the tiny specimens used in this research (3 mm in diameter), they were put in a closed container and 99 % carbon dioxide was injected inside. It can conclude that the carbon dioxide completely diffused into the specimen after two weeks exposure, and it is why signal for calcite is detected for different position inside 6C0d, as shown in Figure 4-14 (b). The reasons why portlandite still remains in the carbonated specimen are as follows: 1) the carbonation process will reduce the pore volume and reduce the diffusivity of carbon dioxide, preventing further carbonation [71]. 2) Portlandite crystals form a protective film of calcite on the surface during carbonation process [140].

(3) Phase transition under seawater immersion

Figure 4-16 and Figure 4-17 shows CT-XRD result of S6N21d and S6N147d respectively. For S6N21d, 5 points were measured by XRD method, while for S6N147d, 10 points were set up along the diameter of the specimen. As representative, the XRD data for points 1, 2, and 5 were shown in Figure 4-17 (b). Some of the unmarked peaks in Figure 4-16 (b) were resulted in interference from the fixed structure of the specimen. See appendix A for details.

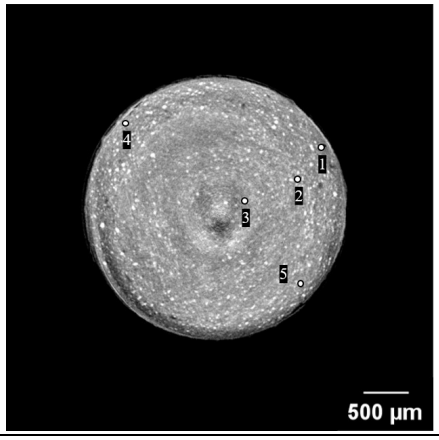

(a) CT image of S6N21d (layer: 0720)

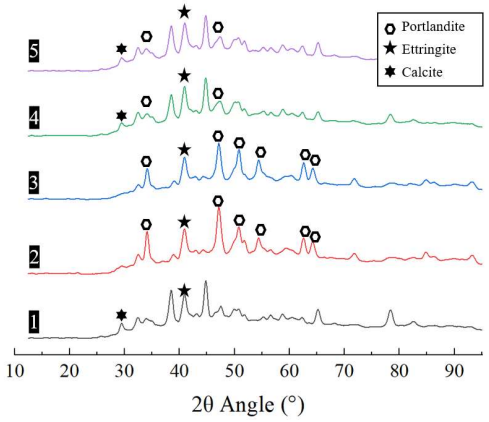

(b) XRD data of S6N21d

Figure 4-16 CT-XRD result of non-carbonated specimen after 21 days seawater immersion (S6N21d)

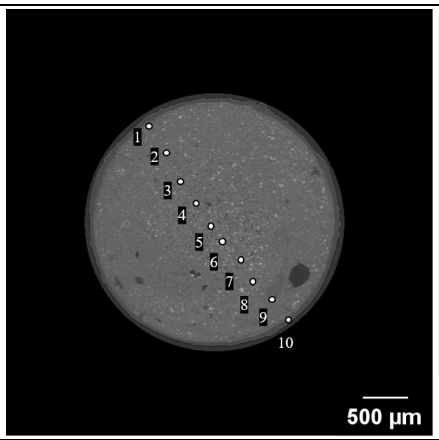

(a) CT image of S6N147d (layer: 0600)

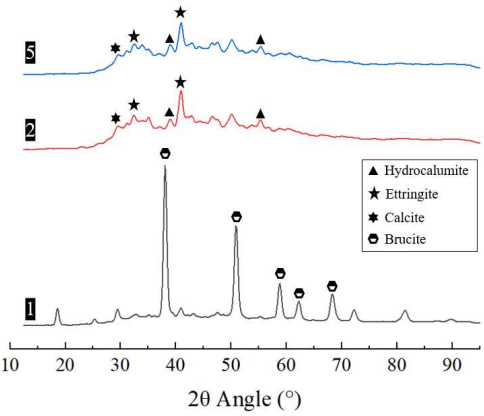

(b) XRD data of S6N147d (partial)

Figure 4-17 CT-XRD result of non-carbonated specimen after 147 days seawater immersion (S6N147d)

Similar to the leaching test in pure water, the leaching of specimen in seawater also resulted in the gradual loss of portlandite. After leaching test in seawater for 21 days, the points at the edge of specimen, such as point 1, 4, and 5, no longer showed obvious XRD diffraction peaks from portlandite, while for points inside the specimen, such as point 2 and 3, clear peaks for portlandite were still detective, as shown in Figure 4-16 (b). After 147 days of leaching, diffraction peaks of portlandite at all point within specimen was no longer detective, as shown Figure 4-17 (b).

However, due to the presence of various ions in seawater, a series of phases were formed inside the specimen in seawater leaching test which were different from those in the pure water leaching test.

The formation of ettringite (AFt) was presented in specimen after 21 days seawater immersion, as shown in Figure 4-16 (b). All points within specimen showed the diffraction peaks of ettringite, which was because the sulfate ions in seawater diffuse into specimen, changing the local sulfate to aluminum ratio, and causing reformation of ettringite [141]. De Weerdt et al considered that precipitation of ettringite can reduce porosity, potentially favoring the resistance of cement-based materials to water attack [141][142]. Due to the relatively fast diffusion rate of sulfate radicals [143][144], the diffraction peak of ettringite was also detected in the center of specimen. Due to the relatively lower solubility of ettringite, the diffraction peak of ettringite was still detected in the specimen after the 147 days seawater leaching test, as shown Figure 4-17 (b).

Chloride ion in seawater may react with the phases of the Portland cement, particularly the aluminum silicate phase (C_3A, tricalcium aluminate) present in the cement, and lead to formation of Friedel's salt. This reaction proceeds as follows:

$$C_3A(s) + 2Ca(OH)_2(s) + 2NaCl(aq) \rightarrow FS(s) + 2NaOH(aq)$$

In CHAPTER 2, it was mentioned that the synchrotron radiation XRD measurement applied in this research has a limited coverage due to the absorption of the X ray diffracted, and it cannot effectively detect the presence

of Friedel's salt. Here, as a complement, the powder XRD method is introduced to detect the presence of Friedel's salt. Figure 4-18 shows powder XRD result of S6N147d, and presence of Friedel's salt is clearly seen in low energy region.

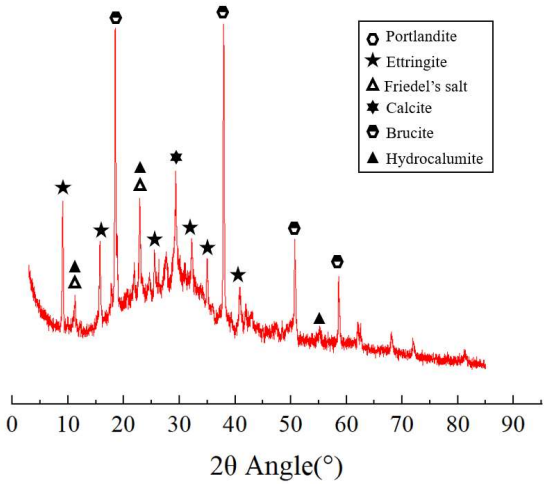

Figure 4-18 Powder XRD result of S6N147d specimen

Friedel's salt is not very soluble in water, so it tends to precipitate out of the pore solution in the concrete as solid crystals. This actually increases the volume of the solid phase and reduces the porosity, which is beneficial to the resistance of cement-based materials to water attack.

Additionally, formation of Brucite was also demonstrated. Brucite, a mineral with the chemical formula $Mg(OH)_2$ (MH) can form in cement paste as a result of various chemical reactions involving magnesium ion and water [146]. In the pore solution, magnesium ions combine with hydroxide ions to form brucite due to lower solubility of brucite compare with portlandite.

Figure 4-19 and Figure 4-20 show TG-DTA curve of specimen without leaching and after 25 days immersion in seawater, respectively. The decomposition of brucite generally begins around 350 °C in air while decomposition of portlandite single crystals begins around 450 °C in air [148].

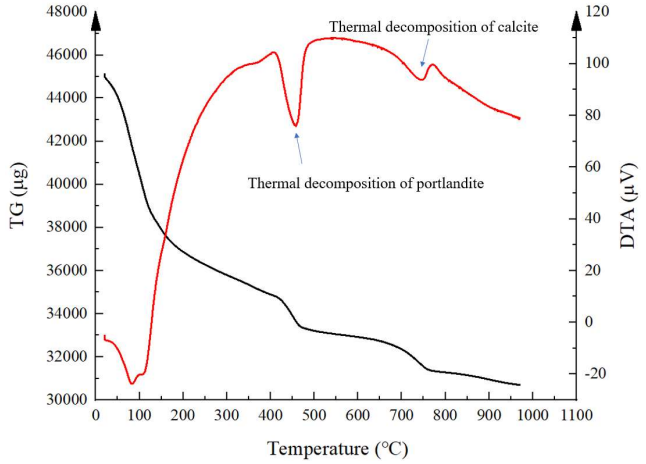

Figure 4-19 TG-DTA curve of specimen without leaching (6N0d)

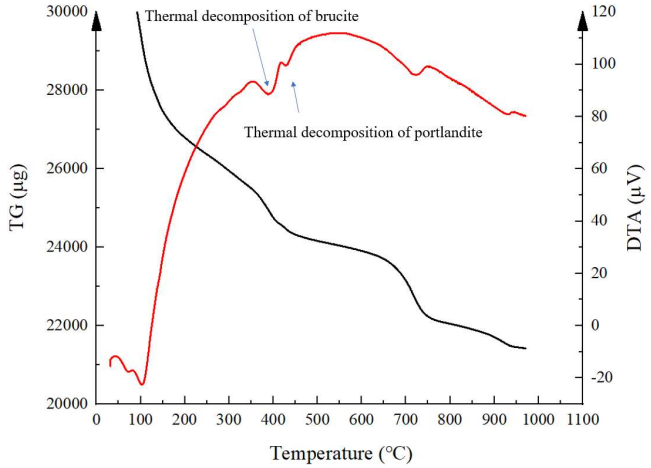

Figure 4-20 TG-DTA curve of specimen after 21 days leaching in seawater (S6N21d)

In both Figure 4-19 and Figure 4-20, thermal decomposition of portlandite and calcite are detected, which comes from the unconsumed portlandite inside the specimen, and the calcite formed due to carbonation during specimen preparation and transfer, respectively. In Figure 4-20, thermal decomposition of brucite is also detected, resulting from conversion of brucite from portlandite during immersion in seawater. The DG-DTA data of S6N21d specimen only revealed the presence of brucite, while the CT-XRD data of S6N147d specimen more intuitively showed the brucite layer. Figure 4-21 shows extracted CT image of S6N147d specimen near the edge of specimen and corresponding XRD data for Point 1 is shown in Figure 4-22, which reveals the presence of brucite layer.

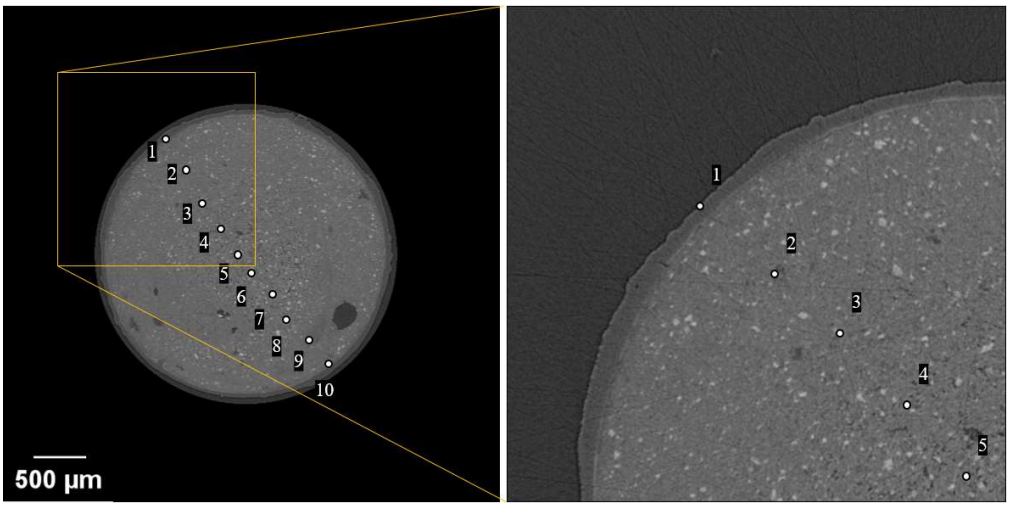

Figure 4-21 Image at the edge of S6N147d specimen

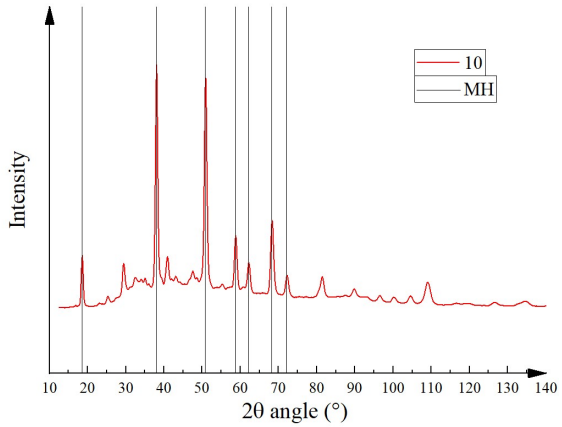

Figure 4-22 XRD data of non-carbonated specimen after 147 days seawater immersion (S6N147d) (point 1)

The brucite layer appears darker on CT images due to the lower density of brucite compared to hydrated products. Thickness of brucite layer is about 30 µm. The solubility product of brucite is very low, which means that magnesium ions will precipitate at a lower pH value. The high pH value of the pore solution environment can easily capture magnesium ions to form precipitates, and that is why the precipitation of brucite mainly form on the surface of specimen. Formation of brucite had been observed by many researchers. Buenfeld and Newman believe that this brucite layer is denser and can protect the interior from further deterioration [146]. However, some studies suggested that the properties of brucite layer is only temporary [147]. The impact of the brucite layer on leaching is complex. On the one hand, it isolated the interior of specimen from the external environment, which may benefit to resistance to leaching. But on the other hand, magnesium ions continue to diffuse into the interior, which also indirectly lowers the pH value and accelerates the dissolution of portlandite and the decalcification of C-S-H gel.

Under ionic environment of seawater, the formation of phases such as ettringite, Friedel's salt were observed

although the boundary of the leaching and non-leaching in the specimen was not found in the CT image. Compared with pure water leaching test, these newly formed phases in seawater environment may have an impact on the leaching process. Sedimentation phase, like Friedel's salt, can refine the pore structure of specimen and can be beneficial to the resistance of specimen to water attack. With the presence of magnesium ions, a brucite layer was formed on the surface of specimen. The dense nature of brucite layer protected the interior of specimen from further leaching. But on the other hand, Magnesium in seawater lowers the pH at the exposure front, which may lead to gradual decalcification of C-S-H gel.

4.2.3 Released calcium amount from specimen

As leaching process proceeds, calcium gradually released from the specimen in the form of dissolution of portlandite and decalcification of C-S-H gel. According to the data obtained in this research, there are two methods that allow to quantify the amount of calcium released from the specimen during the leaching test. The first one is basing the position of dissolution front obtained from CT image and calculating the released calcium amount by making some assumptions. The second one is to directly use the ICP-OES method to measure the calcium ion content in the solvent obtained after each water change. Accumulating it is the total amount of calcium released from the specimen. The parallel implementation of these two methods helps us better understand the leaching behavior of hardened cement paste.

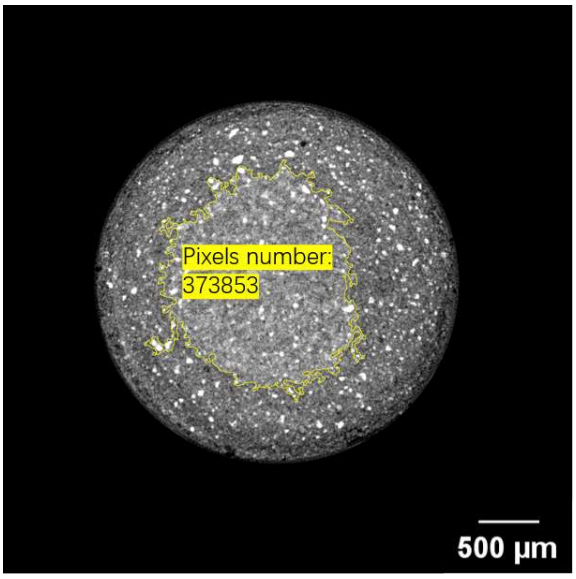

Figure 4-23 Dissolution front of 6N60d specimen

Calculating the released calcium amount from CT images requires introducing the concept of equivalent depth and transforming the dissolution front into ideal circle. Figure 4-23 shows CT image of 6N60d specimen. Area of non-altered region can be obtained by counting pixels number inside the front and then multiplying it by

the area of each pixel i.e., resolution of pixel. Assuming that there is an ideal circle whose area is equal to the area of non-altered region and is concentric with the circle of specimen edge, then, equivalent depth is defined as the distance from edge of specimen to the position of the ideal circle, which can be calculated by eq (4-1):

$$d_e = r - \sqrt{\frac{\overline{NR_e{}^2}}{\pi}} \tag{4-1}$$

In which, r is diameter of specimen, N is number of pixels inside the dissolution front and R_e is resolution of CT image.

Using the aforementioned method (coupling gray scale difference on CT image and XRD data) to extract the dissolution front of portlandite on specimens' CT images with different leaching period in both "5N" and "6N" series, and all dissolution fronts are displayed superimposed on the same image, as shown in Figure 4-24. For each dissolution front, the equivalent depth is also calculated using eq, and Figure 4-24 shows the relationship between equivalent depth of dissolution front and square root of time.

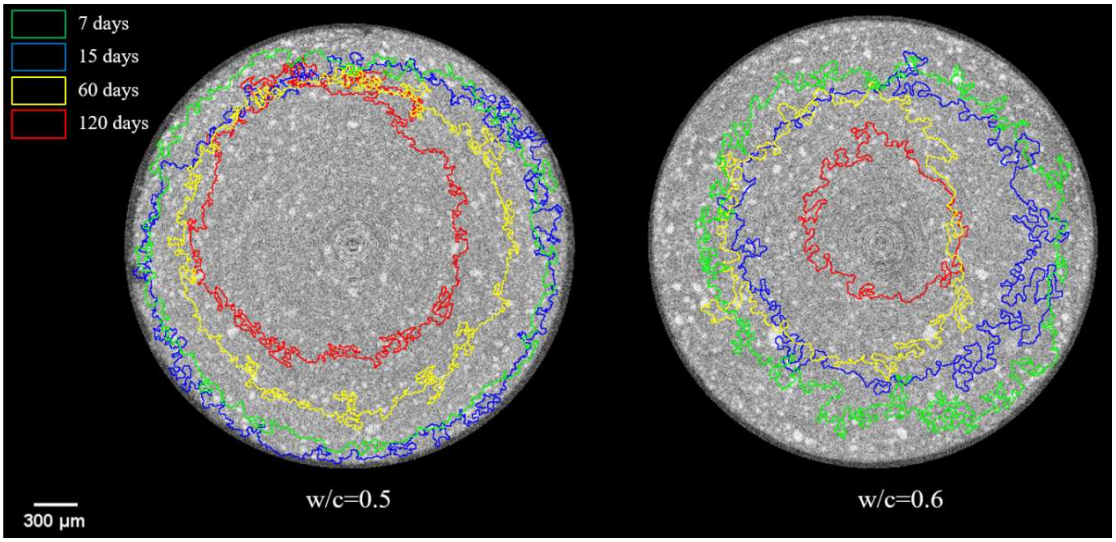

Figure 4-24 Dissolution fronts of specimens with different leaching period

It can be seen that the equivalent depth is basically linearly related to the square root of time, which is consistent with the literature [7][10][14][149]. The leaching degradation is governed by a diffusion mechanism and can be described by Fick's law, which relates the degraded thickness to the square root of time. The slope on the Figure 4-25 reflects the rate at which the dissolution front progresses. The leached depth increases with the leaching period. One factor affecting progress rate of dissolution front is water to cement ratio. Leached depth of specimen with a higher water to cement ratio is greater than that with a lower water to cement ratio.

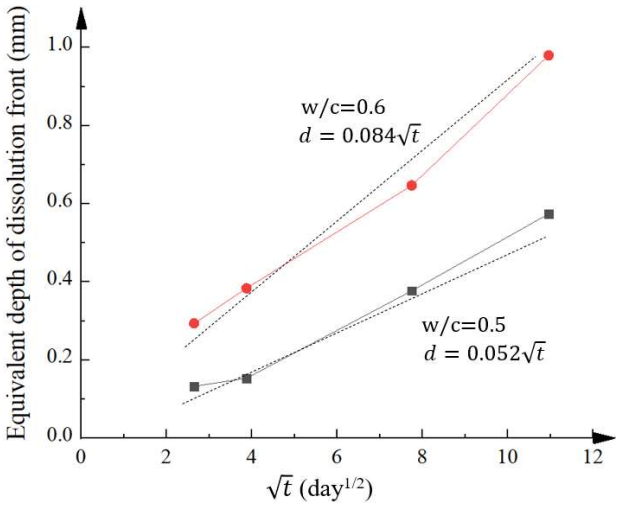

Figure 4-25 Equivalent depth of dissolution front of non-carbonated specimen with different leaching periods

With the dissolution front and corresponding equivalent depth, the accumulated amount of calcium released from the specimen can be calculated based on the following two assumptions: 1) The dissolution front progresses the same distance in all directions, i.e., the equivalent depth, and leaves a non-leached cylindrical core inside the specimen, as shown in Figure 4-26. 2) All calcium from portlandite in leached region is assumed to be released, while in non-leached region not. Released calcium amount per specimen volume can be calculated by eq (4-2):

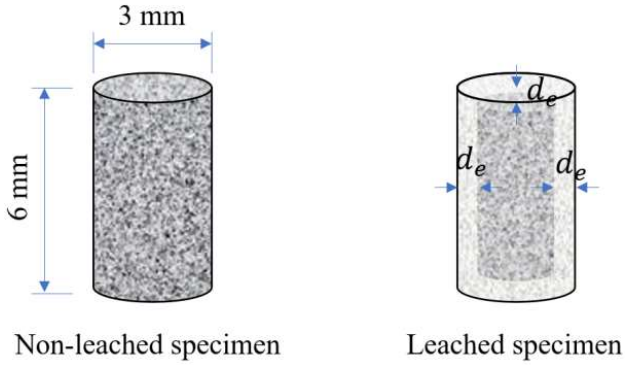

Figure 4-26 Equivalent dissolution front in 3 dimensions

$$\frac{m_{\mathrm{Ca}}}{V} = \frac{1}{V}\{\frac{[V-\pi(r-d_e)^2(h-2d_e)]c_{\mathrm{Ca}}^{\mathrm{CH}}M_{\mathrm{CH}}}{\rho_{\mathrm{CH}}}\} \tag{4-2}$$

In which, r and h are diameter and height of specimen respectively. V is volume of the whole specimen. $\pi(r-d_e)^2(h-2d_e)$is the volume of non-leached core. M_{CH} is molar mass, and ρ_{CH} is density of portlandite. $c_{\mathrm{Ca}}^{\mathrm{CH}}$ is solid phase concentration of calcium from portlandite.

On the other hand, in the leaching test, the solvent after certain leaching period was obtained from each time of water exchange and the calcium ion concentration was measured by applying the ICP-OES method.

Accumulating calcium amount from every time solvent exchanged, we can quantitatively know how much calcium amount released from specimen. Figure 4-27 shows accumulated leached calcium amount per volume with different leaching periods, and released calcium amount calculating from equivalent dissolution front is also attached for comparison. It can be seen that less calcium releases from the specimen with a water to cement ratio of 0.5 at the same leaching time comparing with the specimen with a water to cement ratio of 0.6. This is due to the lower porosity of the lower water to cement ratio specimen. The calculated calcium released amount is in good agreement with the actual calcium released amount in specimens with different water to cement ratio. This shows that during the leaching process, the calcium released from specimen mainly comes from portlandite. The Buil's model mentioned in CHAPTER 1 shows that in addition to dissolution of portlandite, leaching process should also include decalcification of C-S-H gel, which seems to be inconsistent with the results in this section. The reasons for this is as follows: with the existence of portlandite, the calcium ions generated by its dissolution, maintain the calcium concentration in pore solution, result in decalcification of C-S-H gel being inhibited.

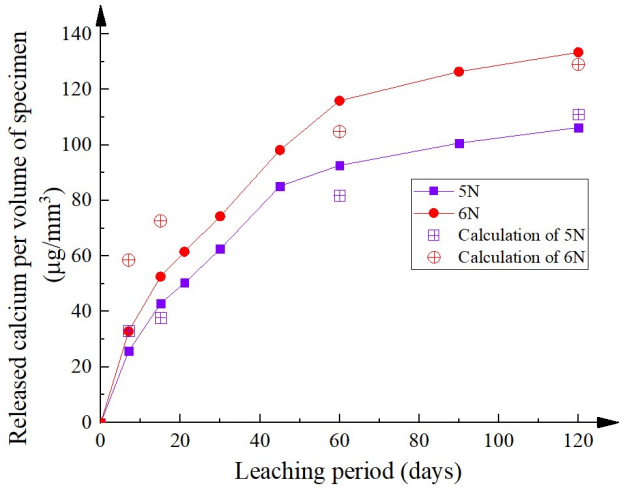

Figure 4-27 Accumulated released calcium per volume with different leaching periods

For carbonated specimen, carbonation consumes the portlandite and converts it into calcite. It results in very little calcium being released from the specimen, and also makes it unable to see obvious deterioration areas, such as dissolution front, on the CT images of specimen. Figure 4-28 shows comparison of calcium amount released from non-carbonated specimen and carbonated specimen after 120 days of leaching period. It shows that under the same water to cement ratio conditions, the calcium released amount of specimen after accelerated carbonation process is only about 25 % of that of non-carbonated specimens. The released calcium amount for carbonated specimen may mainly come from the portlandite remaining after carbonation. As shown in Figure 4-29, the signal of portlandite still remains in the non-leaching but after carbonated specimen (6C0d), while for carbonated specimen after 120 days leaching period, signal for portlandite completely disappeared.

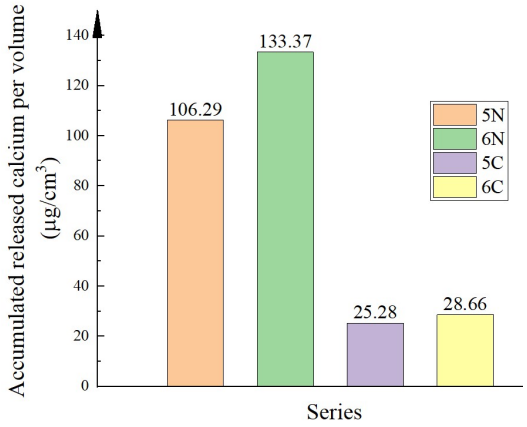

Figure 4-28 Accumulated released calcium per volume after 120 days of leaching period

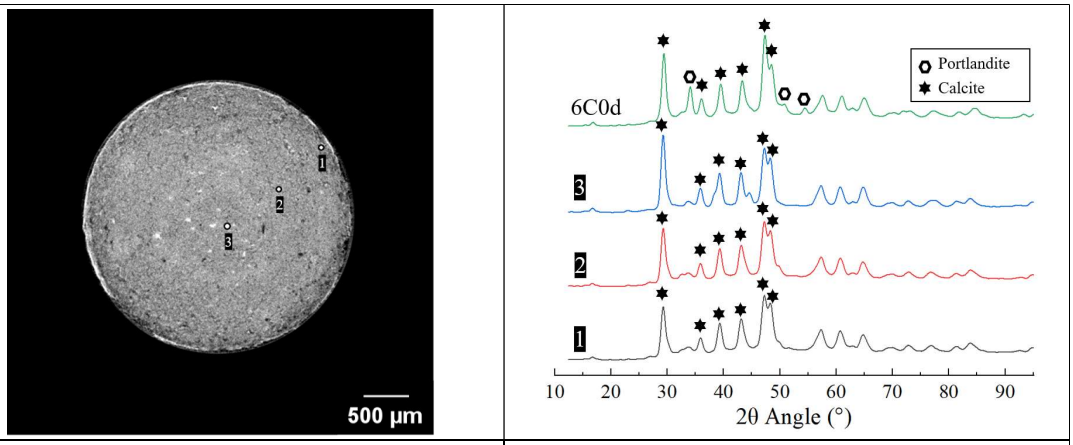

(a) CT image of 6C120d | (b) XRD data of 6C120d

Figure 4-29 CT-XRD result for 6C120d

4.3 TRANSPORT PROPERTY OF LEACHED REGION, NON-LEACHED REGION AND ITZ

When discussing transport properties, we first need to clarify what transport properties is and what indicators we use as a representative of transport properties in this research. Transport properties of cement-based materials refer to the characteristics and behaviors of materials related to the movement of fluids (typically water) and gases within its structure. These properties are important in various engineering applications, such as construction, durability assessment, and the design of concrete structures. Generally, the concept of transport properties includes permeability, porosity, absorption, and diffusivity. For the leaching process in cement-based materials, the pore structure is filled with liquid, and the exchange rate of ions in the pore solution with the external environment is an important indicator for evaluation. As a result, diffusion coefficient is a well indicator to evaluate the transport properties. Previous studies have provided methodologies for quantifying the transport properties of sound-hardened cement paste. In some of these studies, the apparent diffusion coefficient was calculated from the amount of ions released [139][150]. However, research on directly determining transport properties based on the pore structure of concrete is still limited. On the other hand, these studies lack quantification of transport properties for

deteriorated or leaching regions and ITZ in concrete. The difficulty in studying the transport property in ITZ mainly comes from the thin and irregular geometry of ITZ. It is technically difficult to capture the ITZ, let alone obtain detailed pore structure of it. In this section, Basing on the CT images of leaching altered, with an aggregate inside specimen, we will analyze the transport property of interfacial transition zone (ITZ), non-leached region and leached region respectively.

4.3.1 Effect of ITZ on dissolution front

The Interfacial Transition Zone (ITZ) is a critical region within a concrete matrix where the cement paste (composed of cement, water, and sometimes admixtures) in contact with the aggregate particles. The ITZ is a key area in concrete microstructure and is of particular interest in concrete science and engineering due to its influence on the overall performance of concrete. The rate of leaching, which is embodied as the depth of dissolution front, is highly correlated with the permeability of cementitious materials. Theoretically, ITZ has more porous structure compared to bulk hardened cement paste. This makes it more permeable and can provide easier pathways for the movement of water, contaminants, and ions. As a result, leaching may occur more rapidly in the ITZ compared to the rest of the concrete. This will be shown on the CT image that the dissolution front will progress deeper into inner specimen when it contacts the edge of the aggregate. Figure 4-30 and Figure 4-31 illustrate different slices of the extracted stack from 5LN20c and 5LN80c, in which the dissolution front is marked by the yellow line, based on the grayscale value difference between the leaching region and non-leaching region. According to the position of the aggregate in specimen, slices with aggregate exposed at or near the dissolution front were selected here to investigate the effect of ITZ on the leaching process. Taking the center of specimen as the origin, counterclockwise scanning the entire slice in polar coordinates beginning from due east direction (three o'clock, in another way) and measuring the depth of dissolution front simultaneously, the corresponding depth-direction relationship can be obtained and shown on the right.

For every selected slice, the average depth of the dissolution front was shown on the corresponding depth-direction curve. The average dissolution front depth of 5LN80c was greater than that of 5LN20c, which was also verified on CT images. It seems to be a paradox here. The solubility of portlandite decreases as the temperature increase. The increase in temperature seems to weaken the leaching deterioration, rather than increase it. The reason for this situation is that the leaching process is diffusion controlled, that is, compared with the amount of dissolution per unit time, how many calcium ions diffuse from the pore solution to the external environment per unit time is more important. Higher temperature leads to higher diffusion rate, which causes the dissolution front progress deeper at higher temperatures.

For both 5LN20c and 5LN80c, the depth of the dissolution front fluctuates slightly within the average depth in the direction governed by the normal leaching process (i.e., direction not affected by cracks or aggregate). There are peaks in some directions which are not under the effect of the aggregate, such as in 90°, 120° and 180° of 5LN20c slice 700 and 30° of 5LN20c slice 790. CT images show small cracks in this direction. These cracks only appear in specimens containing aggregate because hardened cement paste, and aggregate have different shrinkage

behaviors during hardening process. These cracks provide pathways for solvent to enter, accelerating the dissolution process, which may lead to a deeper dissolution front. Regardless of the interference of the crack, peaks are present in all slices of 5LN20c in the direction of 270°. This is mainly attributable to the aggregate close to the dissolution front and the ITZ with a more porous structure, which makes it easier to be degraded in this direction. In 5LN80c, all slices showed a "U" shape trend in the direction around 60°. This "U" shape is due to the aggregate exposed to the dissolution front, while the peaks on both sides are due to the existence of ITZ, making the dissolution front go deeper inside the specimen along the aggregate surface. It is also observed that the "U" shape for 5LN80c slice 640 is not completely symmetrical, containing only one side peak. Because of the strike direction of the aggregate, the thickness of ITZ on both sides was not generally the same, which resulted in the different progression of the dissolution on both sides of the aggregate.

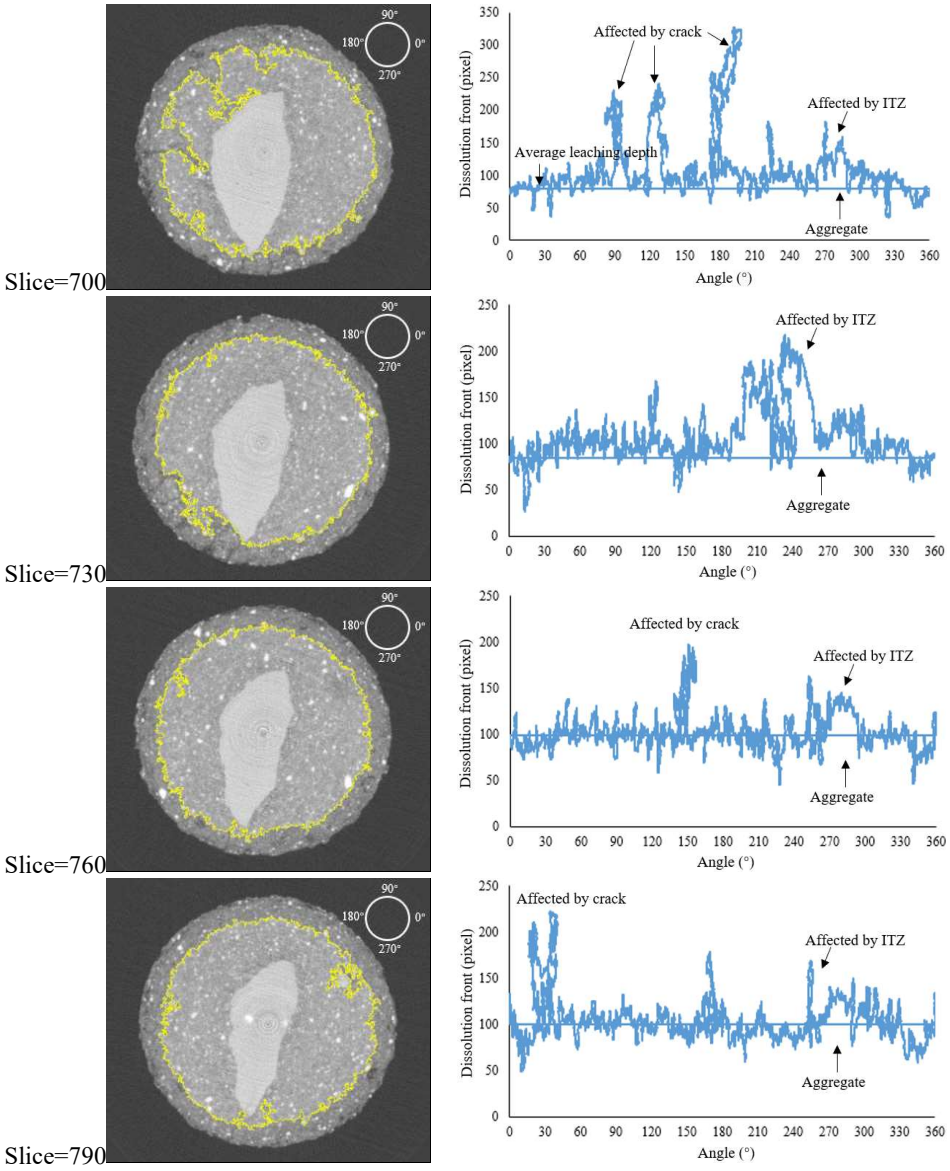

Figure 4-30 Dissolution front of different slices of 5LN20c

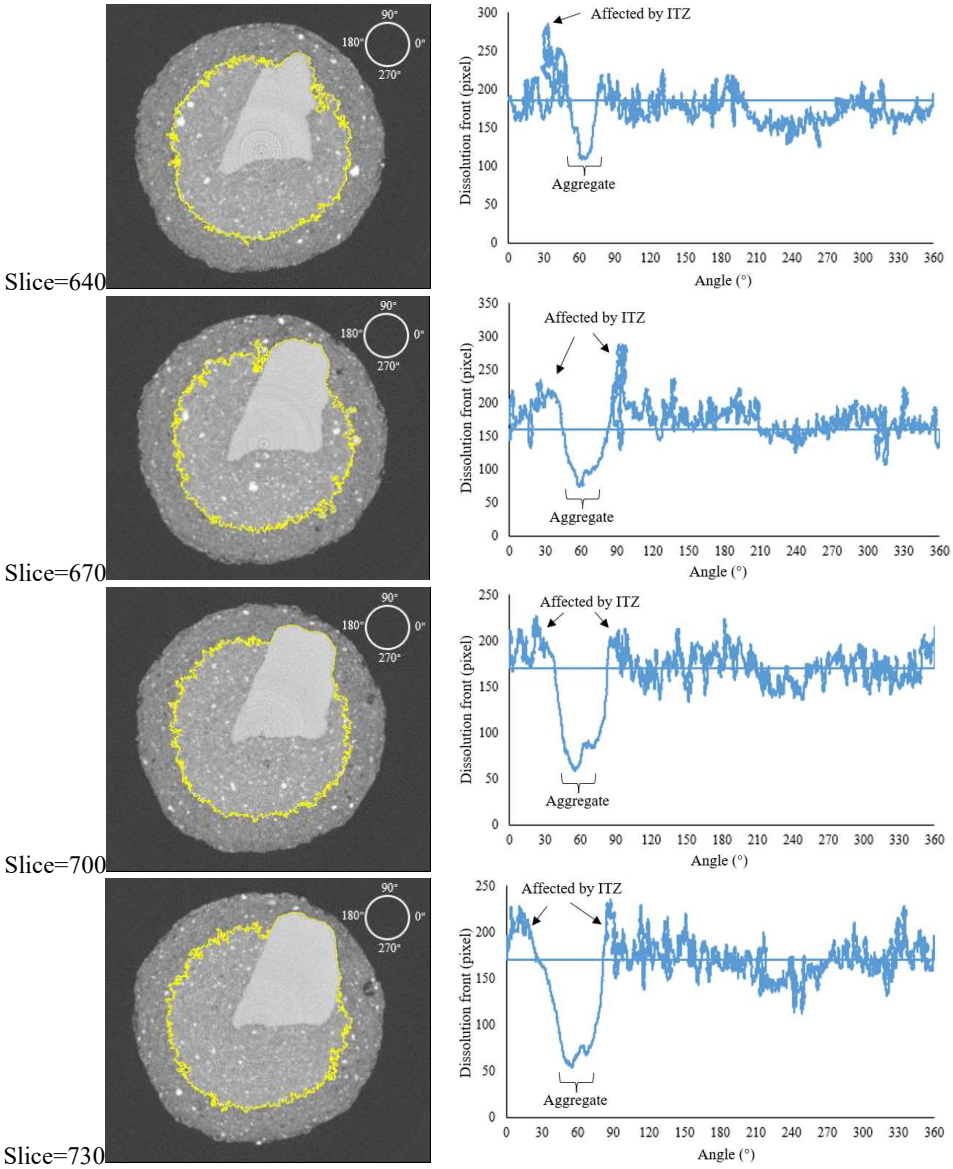

Figure 4-31 Dissolution front of different slices of 5LN80c

4.3.2 Image reconstruction and segmentation

Section 4.3.1 showed that ITZ has high transport properties, resulting in dissolution front progress deeper at the intersection with the aggregate profile. How to quantify the transport properties of ITZ becomes the next topic. Previous studies on transport properties in ITZ have mainly focused on computer simulation [151][152][153] or macroscopic experiments [154][155]. Although the previous studies confirms the higher permeability of ITZ, the information of microstructure directly from real ITZ is still lack. This is largely due to the thin and irregular geometric properties of ITZ. The irregular shape of the aggregate inevitably results in the ITZ around the aggregate is typically uneven in shape, making the extraction and further analysis challenging. Therefore, it is necessary to

process ITZ region and improve the geometric characteristics of ITZ to make it easier to analyze while retaining the original information. This research proposes an image reconstruction method for the regularly shaped ITZ region. Figure 4-32 depicts the schematic of reconstruction in a single slice.

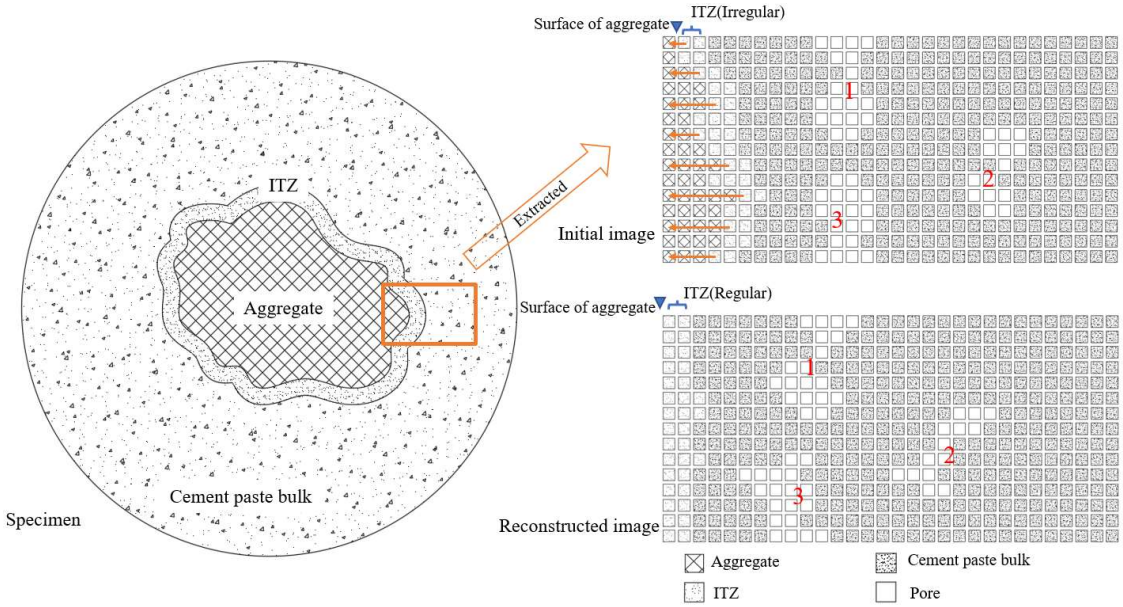

Figure 4-32 Schematic of reconstruction in one single slice

Pixels adjacent to the aggregate surface will be aligned on the same line, and irregularly shaped ITZ will become regular simultaneously. As shown in Figure 4-32, there are three labeled pores in the image before and after reconstruction, labeled as No.1, 2, and 3. Pore No.1 becomes disconnected after reconstruction, while pore No.2 becomes connected. The connectivity of pore No.3 is unchanged, but its shape is changed. Reconstruction seemed to affect the topology of the pore, but when the direction away from the aggregate surface was used as the coordinate, the influence of reconstruction on different areas was the same. At the same time, considering the continuity of the aggregate surface, reconstruction would largely retain the original pore structure's characteristics.

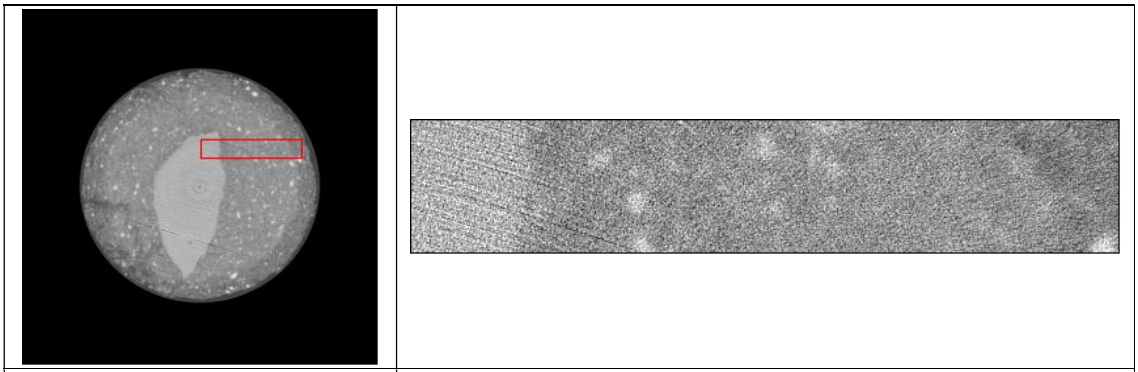

(a) 5LN20c (layer 0720)	(b) Selected ROI (540×100 pixels)

Figure 4-33 Extraction of strip ROI

To illustrate, single aggregate containing specimen under 33 days 20 ℃ leaching test was introduced for discussion. Figure 4-33 (a) shows CT image of 5LN20c and selection a strip ROI, which includes aggregate, non-leached region, and leached region, respectively. Figure 4-33 (b) shows the extraction of ROI region, with size of 540 × 100 pixels. For the strip ROI, from left to right, the gray scale value from high to low corresponds to aggregate, non-leached region, and leached region respectively. It is necessary to clarify which part of strip ROI belongs to the aggregate and remove it. Figure 4-34 (a) shows the binary image of the aggregate profile extracted through the gray scale value difference. Figure 4-34 (b) the region selected using the same strip ROI, in which the white part is aggregate.

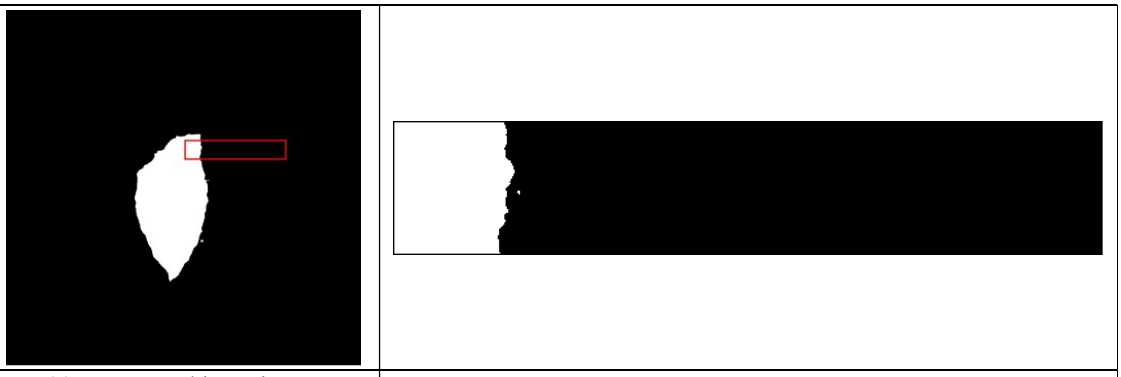

(a) Aggregate binary image | (b) Selected ROI (540×100 pixels)

Figure 4-34 Extraction of aggregate part in strip ROI

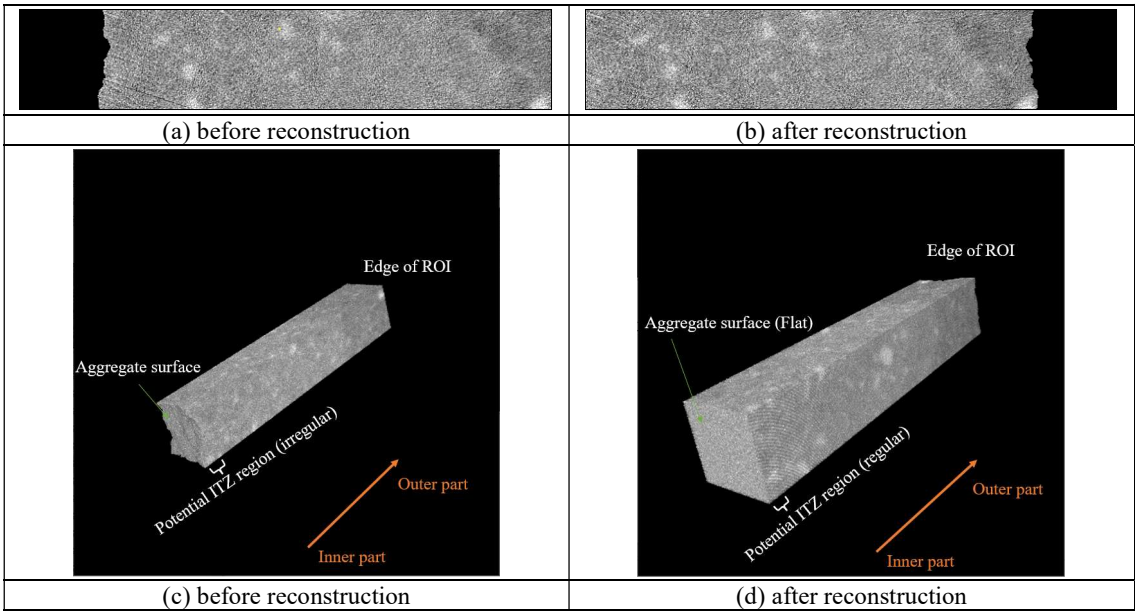

(a) before reconstruction | (b) after reconstruction

(c) before reconstruction | (d) after reconstruction

Figure 4-35 Reconstruction of selected ROI and VOI

Using the Boolean operation, subtracting the aggregate portion from Figure 4-33 (b) gives an image from the adjacent region excluding aggregate to the leached region, as shown in Figure 4-35 (a). The same operation

can be applied to different slices in the stack. Here, layers from 0671 to 0770 were selected, and the three-dimensional diagram of the stack after the operation is shown in Figure 4-35 (c). As shown in Figure 4-32, align every pixel in contact with the aggregate surface to a line, and perform corresponding operations on the subsequent pixels to obtain a single reconstructed slice. Preforming it to the stack can obtain the reconstructed stack. Figure 4-35 (a) and Figure 4-35 (b) shows reconstruction process in single slice, while Figure 4-35 (c) and Figure 4-35 (d) shows in 3 dimensions.

To analyze the changes in transport properties from aggregate surface to the leached region, it requires dividing the VOI into several regions and then performing analysis in each sub-region. Through the reconstruction process, the originally irregular contact surface with the aggregate becomes flat, which makes it possible to divide equidistantly from the adjacent areas of the aggregate to obtain multiple VOIs. In this research, these VOIs are named as sub-VOI. Segmentation of sub-VOIs is shown in Figure 4-36. The sub-VOI closest to the aggregate surface was set as No.1, and subsequent sub-VOIs were numbered accordingly. The sub-VOI closest to the aggregate, i.e., No.1, contains the 3D information of ITZ in theory, while the rest of the sub-VOI are located in non-leaching and leaching regions, respectively. The locations are based on the positional relationship with the dissolution front. Because of the uncertainty of the ITZ thickness, it is difficult to determine if the No.1 sub-VOI completely covers pure ITZ. However, it can be confirmed that the pore structure of the No.1 sub-VOI is affected by ITZ, to the very least. It should also be noted that the opposite surface of the striped VOI becomes irregular after reconstruction, making it difficult for sub-VOI segmentation to cover the whole striped VOI. Thus, a small portion near the edge cannot be analyzed. This was a compromise that had to be made to analyze the ITZ region. Subsequent process such as binary, pore labeling and extraction will be conducted to each sub-VOI. The 3-D pore structure of each sub-VOI was obtained by thresholding the stack of the sub-VOI based on the gray level histogram, which is discussed detailly in previous part of this research. As an example, processing of No.4 sub-VOI is shown in Figure 4-36. The segmented No.4 sub-VOI is binarized to obtain the pore space. The threshold for binary process is determined from histogram of the whole striped VOI, and it is applied for all sub-VOI. After pore cluster labeling, pore space is divided into connected pore, i.e., the largest pore cluster, and isolated pore, i.e., the remaining pore clusters. Removing all the isolated pore, and the pore structure of No.4 sub-VOI can be obtained.

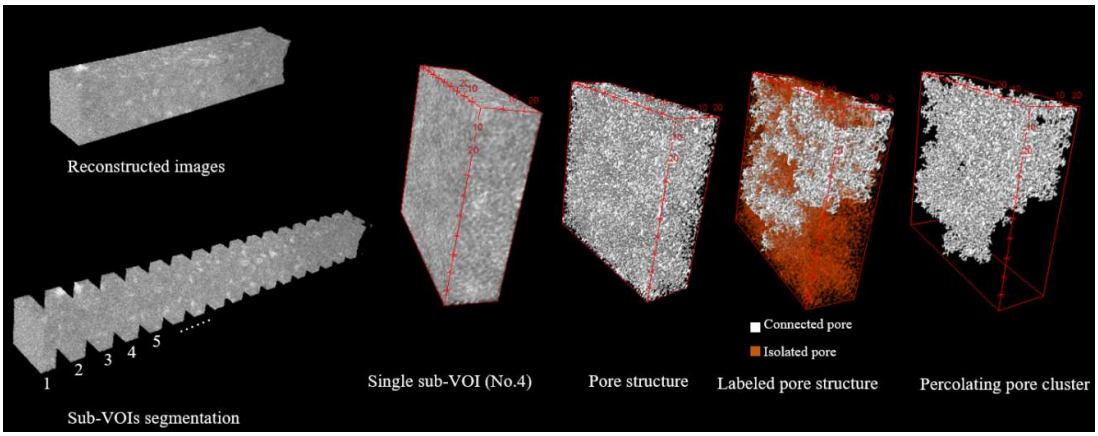

Figure 4-36 Segmentation of sub-VOIs

4.3.3 Quantitative analysis of diffusion coefficient in non-carbonated specimen

The purpose of dividing sub-VOIs and extracting the pore structure of each sub-VOI is to apply random walk simulation on each sub-VOI and obtain the position change map of the calculated diffusion coefficient from region close to the aggregate to region far away from the aggregate until region in leached region. Figure 4-37 shows CT image of 5LN20c and 5LN80c, with the following mark: dissolution front of portlandite (blue line) and ROIs (yellow line). There are three labeled striped ROIs (A, B, and C) on CT image for both 5LN20c and 5LN80c, and corresponding VOIs will be extracted for further processing. 100 slices were extracted from CT images stack, and layer range is from 0671 to 0770 for both 5LN20c and 5LN80c. The width of all ROIs is 100 pixels, which makes the size of the cross-section of each striped VOI is 100 × 100 pixels. According to the position of dissolution front, it can be seen that all VOIs contains aggregate region, non-leached region, and leached region.

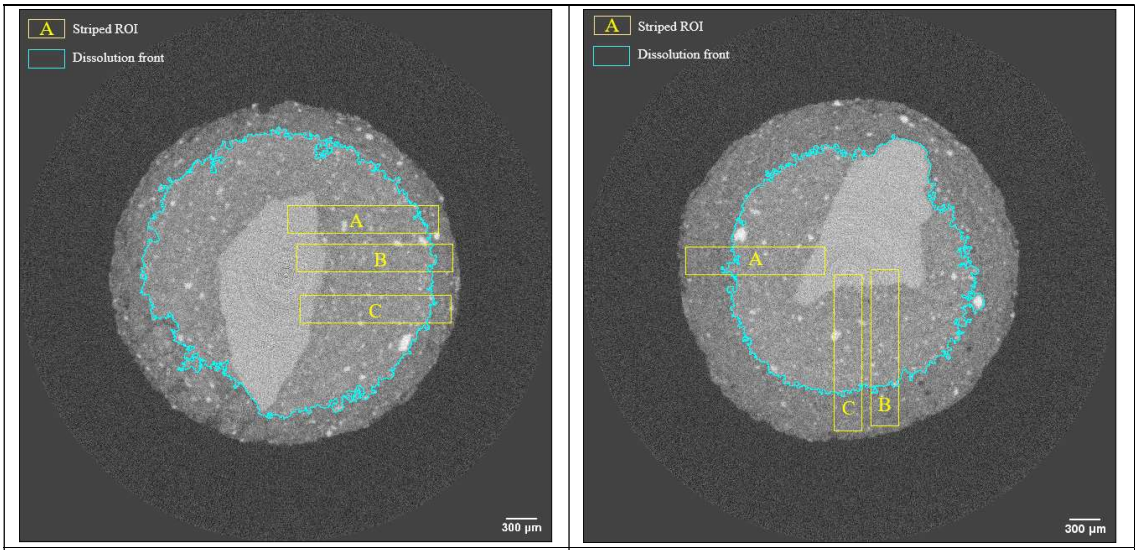

(a) 5LN20c specimen (layer: 0720) (b) 5LN80c specimen (layer: 0720)

Figure 4-37 Striped ROIs selection of 5LN20c and 5LN80c specimens

The result of the random walk simulation for a given sub-VOI with the determined tortuosity is shown in Figure 4-38. The supplementary figure in Figure 4-38 shows that at the beginning of random walk, trajectory is not yet limited by obstacles, thus MSD-t curve shows unrestricted behavior. As time elapses, walkers migrate further than pore size and get contact with obstacle (i.e., solid phase), and MSD-t curve shows restricted behavior [156]. In the long-time limit, the random walkers fully experience the pore structure and slope of MSD reaches a constant value.

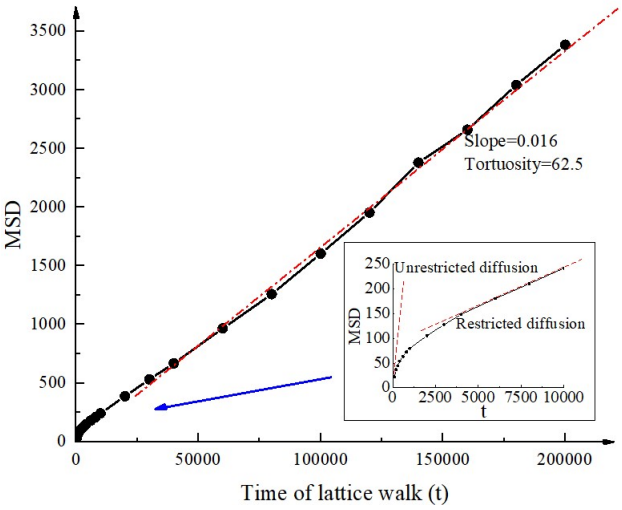

Figure 4-38 Output of MSD-time relationship in an extended sub-VOI

Tortuosity can be calculated by eq (3-4) and the computed diffusion coefficient was calculated by eq (1-1). Figure 4-39 shows the result of each sub-VOI. It should be emphasized that the diffusion coefficient here is based on the self-diffusion coefficient of ions in water, obtained by modifying the pore structure, and does not consider the gradient effect and the interaction between ions. Self-diffusion coefficient of calcium ion refers to the previous research [157].

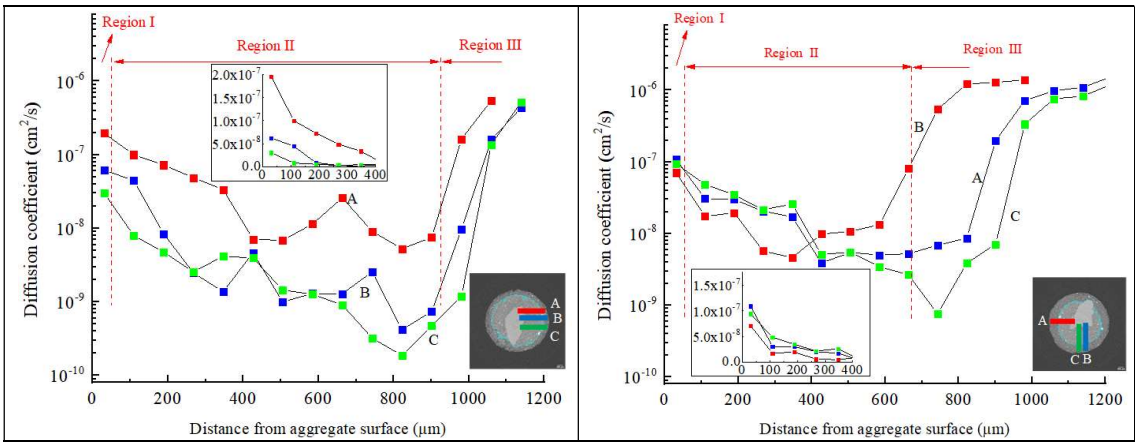

(a) 5LN20c (b) 5LN80c

Figure 4-39 Computed diffusion coefficient of Ca^{2+} ion in each specimen

By analyzing each striped VOI individually for both 5LN20c and 5LN80c, the striped VOI can be roughly divided into three regions along the direction away from the aggregate surface, depending on the apparent difference in the computed diffusion coefficient. The segmentation of the three regions is shown in Figure 4-39 and regions are labeled as Region I, Region II, and Region III. Region I begins from aggregate surface and ends when the computed diffusion coefficient of a subsequent sub-VOI is less than half of the average diffusion coefficient of all previous sub-VOIs. Segmentation of Region II and III bases difference of computed diffusion

coefficient. The computed diffusion coefficient of Region III is much larger than that of Region II, and the boundary between Region II and III highly coincides with the interface between the leaching region and non-leaching region, i.e., dissolution front in each striped VOI. It should also be noted that when placing the three-striped VOI into one plot for analysis, the boundary between Region I and II coincide well with each other, while the boundary between Region II and III does not. This phenomenon will inevitably appear when the distance from the aggregate surface is used as the coordinate axis because Region I roughly reflects the computed diffusion coefficient near the aggregate surface, while Region II reflects the non-leaching region. Supplementary figures that focus on near aggregate surface in Fig.14 (a) and (b) show rather distinct drop of the diffusion coefficients between Region I and Region II, respectively. Thus, in this study, Region I, Region II, and Region III correspond to the ITZ, non-leaching, and leaching regions, respectively. In addition, specimens subjected to different leaching temperature shows the following difference in Fig.14: diffusion coefficient of region III is higher in 5LN80c, and the scope of region III is also larger in 5LN80c.

Table 4-1 shows the computed result of the Ca^{2+} ion diffusion coefficient for each region and each specimen. The average of the diffusion coefficients was computed using the corresponding sub-VOIs in each region given in Figure 4-39.

Table 4-1 Computed result of Ca^{2+} ion diffusion coefficient (cm^2/s)

Specimens	ITZ	Non-leached region	Leached region
5LN20c	9.63×10^{-8}	1.17×10^{-8}	4.99×10^{-7}
5LN80c	9.15×10^{-8}	1.12×10^{-8}	1.15×10^{-6}

In the previous research, the estimated thickness of ITZ ranged from 9 μm to 300 μm [56][57][58][59][158][159][160]. In this study, the thickness of each sub-VOI is 30 pixels, resulting in an actual thickness of 73.8 μm for one sub-VOI. The diffusion coefficient in the ITZ determined in this study is within the range of the previously reported values in the literatures. The estimation of ITZ transport properties is relatively lacking. Table 4-2 shows the estimation of calcium ion diffusion coefficient in the leached region and non-leached region in previous studies, and also attaches the estimation results from this research. In which, Buil's result comes from model estimation. Nakarai's result also comes from model estimation, which includes solid-liquid equilibrium model. Saito's result was obtained in mortar specimens using electrophoresis method. Hitomi's result was obtained by measuring the pores of hydrated cement paste through μCT and then estimating the diffusion coefficient by simulation. It is worthwhile that different from these previous research, the estimation of the diffusion coefficient in ITZ was directly made using the CT image in this research.

Table 4-2 Comparison of Ca^{2+} ion diffusion coefficients in previous studies

Ca^{2+} ion diffusion coefficient ($\times 10^{-8}$ cm^2/s)	This research	Buil [32]	Nakarai [162]	Saito [161]	Hitomi [163]
Non-leached region	1.17	5.00	7.79	1.00	1.92

Leached region	49.9	1000.00	-	170.00	17.8

ITZ without deterioration was framed when selecting VOI, and the computed result in the selected ITZ from 5LN20c and 5LN80c were found to be similar. Furthermore, the diffusion coefficients in non-leached regions of 5LN20c and 5LN80c are similar. As a result, it can be said that the influence of temperature on Ca^{2+} ion diffusion coefficient is significant in leached region but not large in intact region of the specimen. Summarizing the results, the diffusion coefficient of Ca^{2+} ion in non-deteriorated ITZ increases by a factor of 10 when compared to the non-leached region. The diffusion coefficient of Ca^{2+} ion in the leached region is approximately 50 times that of the non-leached region in the 5LN20c specimen and approximately 100 times in the 5LN80c specimen. Higher diffusion coefficients of Ca^{2+} ion in the leached region for 5LN80c correlate to a larger accumulated amount of Ca^{2+} ions. This is attributed to the promoted dissolution of hydration products due to higher temperature.

4.3.4 Effect of carbonation on transport properties

Figure 4-40 shows CT image of 6N0d, 6C0d and 6C120d, several ROIs were selected on each specimen. Size of each ROI is 100 × 100 pixels. Layer from 0671 to layer 0770 were extracted from CT images stack for all the three specimens, which makes size of each extracted VOI is 100^3 cube.

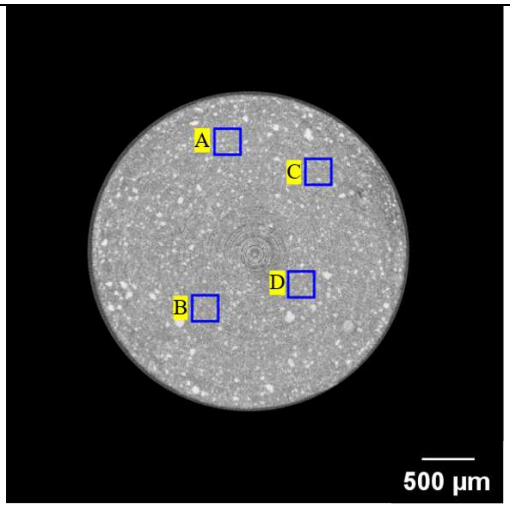

(a) 6N0d (layer: 0720)

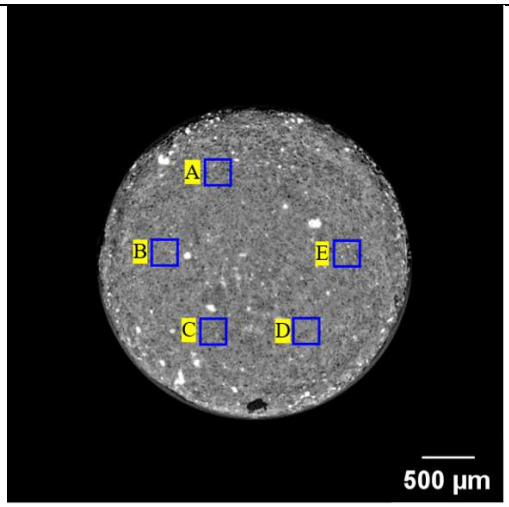

(b) 6C0d (layer: 0720)

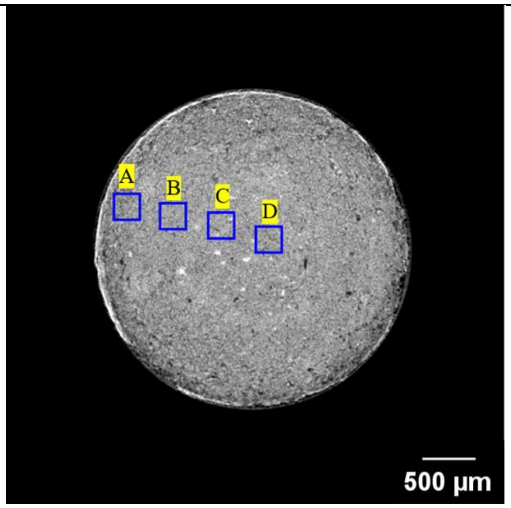

(c) 6C120d (layer: 0720)

Figure 4-40 CT image and VOIs selection of 6N0d, 6C0d and 6C120d

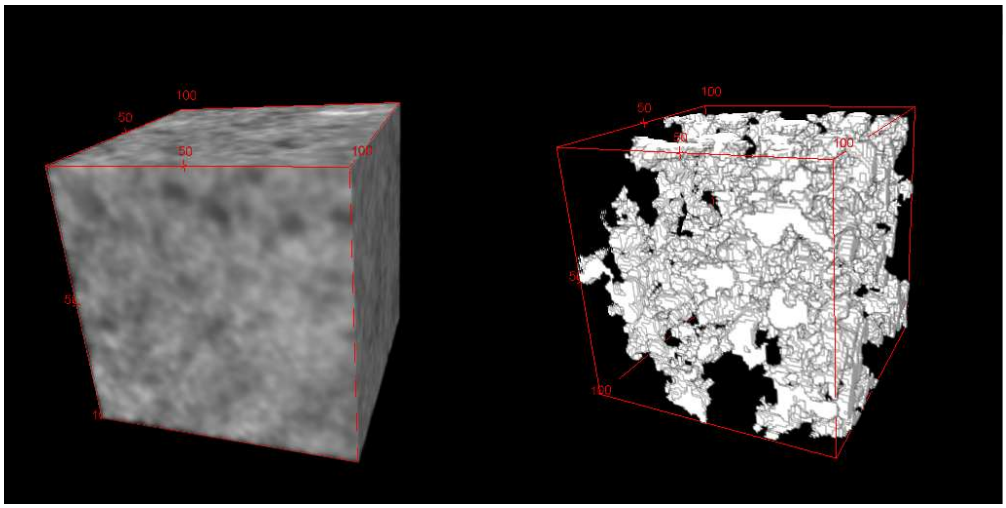

Figure 4-41 VOI A in 6C0d and corresponding pore structure

Similarly, for each VOI, we can use aforementioned image processing method to extracted pore structure and apply the random walk algorithm to quantify the tortuosity of the extracted pore structure. As an example, extracted VOI A from 6C0d is shown in Figure 4-41. Diffusion coefficient of calcium ion can be calculated and used as a quantitative indicator of transport properties. Figure 4-42 shows diffusion coefficient of calcium ion in different VOIs in 6C120d. Result from Figure 4-42 shows that after 120 days of leaching, the carbonated specimen (6C120d) did not show related change in diffusion coefficient along the depth from edge of specimen.

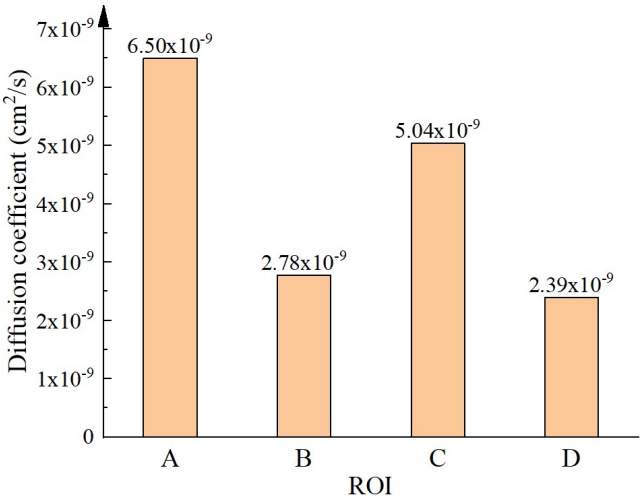

Figure 4-42 Diffusion coefficient of VOIs in 6C120d

Figure 4-43 shows comparison of diffusion coefficient result between 6N0d, 6C0d, and 6C120d, and all results are obtained by averaging results from different regions in the same specimen. Result shows that the diffusion coefficient of the non-carbonated specimen is significantly higher than that of the carbonated sample. This is because of volume of pore reducing due to formation of calcite. While for carbonated specimen, there was no significant difference between before and after 120 days leaching. The above results all illustrate that the carbonation process improves resistance to pure water leaching.

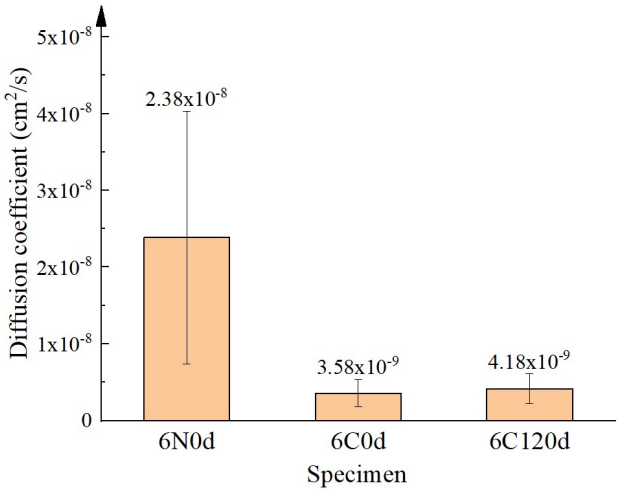

Figure 4-43 Diffusion coefficient comparison between 6C0d and 6C120d

4.4 SUMMARY

In this chapter, focuses were mainly put on how to evaluate the transport properties using the method developed in CHAPTER 3. Firstly, phase transition under leaching in different solvent and carbonation were

analyzed, using integrated CT-XRD method. In the analysis of non-carbonated plain hydrated cement paste specimen leaching in pure water, combining with XRD data, it can be seen that portlandite dissolves during leaching process, and therefore forms a portlandite dissolution front inside the specimen. According to the position of dissolution front of portlandite, the interior of the specimen is divided into leached region and non-leached region. Analysis of carbonated specimen shows that portlandite was partially converted into calcite during carbonation process. During the leaching process, the calcium released from non-carbonated specimen mainly comes from the portlandite originally present in the leached region, while for carbonated specimen, the released calcium may come from the dissolution of residual portlandite after the carbonation process. Carbonated specimen had less calcium released amount compared to non-carbonated specimen, indicating that carbonation improved the resistance of cement-based materials to leaching deterioration. Analysis of non-carbonated plain hydrated cement paste specimen immersed in seawater shows phases of ettringite, Friedel's salt and brucite formed under ionic environment. With presence of magnesium ion, a brucite layer about 30 μm thickness was formed on the surface of specimen. Its dense characteristics may help protect the components inside the specimen from leaching deterioration.

Secondly, transport properties of leached region, non-leached region, and ITZ were quantitatively evaluated. A reconstruction method of region adjacent to aggregate was originally proposed, which allows the division of sub-VOI from aggregate surface and enables the transport properties analysis on each sub-VOI. Using this method, change of calculated diffusion coefficient of calcium ion from aggregate surface to outer edge of 5LN20c and 5LN80c specimen were obtained respectively. According to the difference in calculated diffusion coefficient of calcium ion, three regions were divided and were corresponded to ITZ, non-leached region, and leached region respectively. The diffusion coefficient of calcium ion in these three regions were quantified. Results showed that the diffusion coefficient of calcium ion in the leached region is approximately 50 times that of the non-leached region in the 5LN20c specimen and approximately 100 times in the 5LN80c specimen. The diffusion coefficient of calcium ion in non-leached ITZ increased by a factor of 10 when compared to the non-leached region for both 5LN20c specimen and 5LN80c specimen. Analysis on the shape of dissolution front showed that dissolution front invades into interior of specimen along with aggregate, which reflects the effect of ITZ on leaching process.

Lastly, effect of carbonation on transport properties is also evaluated. Specimen of 6N0d, 6C0d and 6C120d were sampled, the pore structure of sampling regions were analyzed, and the corresponding diffusion coefficient of calcium ion were also calculated. Results showed that there is no obvious radial gradient change in the diffusion coefficient of calcium ion on 6C120d, the diffusion coefficient of calcium ion is basically consistent with that in 6C0d. On average, the diffusion coefficient of calcium ion in carbonated specimen is about 15% of that of non-carbonated specimen (6N0d), which indicated that carbonation process increases the resistance of cement-based materials to leaching deterioration.

CHAPTER 5 APPLICATION OF IMAGE ANALYSIS DATA TO TRANSPORT PREDECTION

5.1 GENERAL

The existing conclusions should serve the durability assessment of cement-based materials, especially for the long-term deterioration mechanism of leaching. This chapter mainly describes how to use the obtained data from image analysis to predict the leaching of cement-based materials. Firstly, long term dissolution of calcium ions is simulated by the simultaneous ion transport model (SiTraM). Effect of ITZ on the transport is highlighted numerically. By combining the SiTraM model with the quantitative evaluation results of transport properties obtained in this research, the leaching process of specimens shown in CHAPTER 2 was simulated. With the quantitative effect of ITZ, the leaching of concrete was also further simulated. Lastly, a method for estimating the extent to which harmful components enter the interior of cement-based materials through leaching processes was also proposed. Considering the Fukushima accident, the concrete is in contact with solution containing strontium ion (Sr^{2+}) and cesium ion (Cs^{+}). Simultaneous strontium ion diffusion was taken as an example for explanation. In a one-dimensional model, coupling leaching process, strontium ion diffusion depth was estimated.

5.2 SIMULTANEOUS ION TRANSPORT MODEL

Simultaneous ion transport model (SiTraM) was proposed by previous researchers [164][165], and it includes mutual diffusion coefficient model, characterizing pore structure model and ion-solid interactions model. This model considers the influence of mutual diffusion of ions during leaching process, the influence of pore structure on diffusion, and the influence of ion exchange between liquid and solid phase on pore structure.

5.2.1 Diffusion of multiple ions

The framework of SiTraM is based on the Fick's second Law as shown in eq (5-1), in which the diffusion coefficient is modified accordingly considering different impact factors.

$$\frac{\partial c}{\partial t} = D\nabla^2 c$$
$$\text{One dimensional: } \frac{\partial C}{\partial t} = D\frac{\partial^2 C}{\partial x^2} \tag{5-1}$$

The first is to modify the diffusion coefficient considering multi-ion environment. Anions are negatively charged, and cations are positively charged. As a result, they can exert electrostatic forces on each other. Oppositely charged ions (e.g., anions and cations) will tend to attract each other while ions with same charge will repel each other. This kind of effect can influence their movement during diffusion. Ion diffusion in a multi-ion

environment is affected by the concentration of other ions due to the limitation of solution neutrality. Felmy and Weare developed a calculation method on mutual diffusion coefficients of several ionic present in multi-ion environment [52][53][166].

5.2.2 Pore structure and liquid-solid inter-reaction

As mentioned in CHAPTER 3, the influence of pore structure on the diffusion process can be quantified by eq (5-2). In which, the porosity is not fixed, and its change is related to the dissolution of hydrated products, including dissolution of portlandite and decalcification of C-S-H gel. The non-uniformity of deterioration in space and time causes the porosity to change dynamically. This change needs to be described by the liquid-solid inter-reaction model. In addition, in SiTraM, the tortuosity is only considered in the parameter input stage. In the subsequent deterioration process, the model considers that the tortuosity has not changed.

$$D_e = D_f \frac{\rho}{\tau} \tag{5-2}$$

The behavior of calcium released from the specimen is related to the calcium concentration in the solid phase and the calcium ion concentration in the pore solution. It is this interaction between solid and liquid phases that leads to changes in the volume of the solid phase, thereby changing the pore structure. Berner and Buil obtained the dissolution equilibrium of hydrated cement paste (portlandite and C-S-H gel system) based on experiments [32], as shown in Figure 5-1.

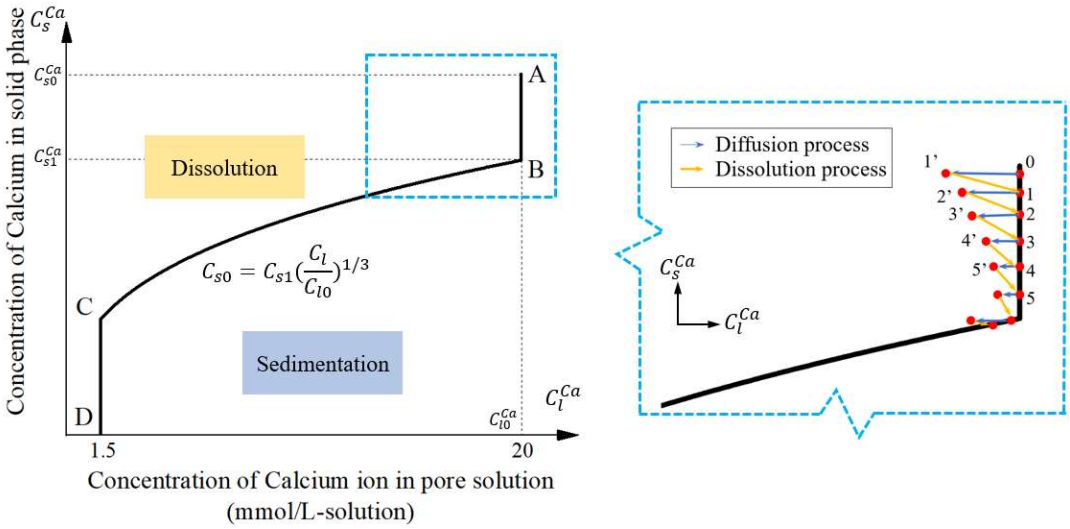

Figure 5-1 Dissolution equilibrium of hydrated cement paste (portlandite and C-S-H gel system)

The C_s^{Ca}-C_l^{Ca} curve reflects dissolution equilibrium of hydrated products, including portlandite dissolution and C-S-H gel decalcification. In which, C_{s0}^{Ca} is initial calcium content in solid phase, while (C_{s0}^{Ca}-C_{s1}^{Ca}) is calcium

content in solid phase from portlandite. C_s^{Ca}-C_l^{Ca} curve (A-B-C-D) divided the plane into two regions: Region above the curve is the dissolution region. In dissolution region, calcium in solid phase tend to release into liquid phase until equilibrium is reached, which means that the state point in dissolution region will gradually return to the curve. Below the curve is the precipitation region, where state points return to the curve through precipitation. States point on the curve reflect the dissolution equilibrium between solid and liquid. Due to the different dissolution behaviors of hydrated products, the curve is divided into different segments. The vertical segment AB represents that calcium concentration in pore solution is stable at 20 mmol/L resulting from continuous dissolution of portlandite. The line BC represents decalcification of C-S-H gel after the dissolution of portlandite, and it is fitted by a function $C^{1/n}$ $(n = 3)$. The shape of C-S-H gel solubility curve has been taken as similar to the empirical curve proposed by Glasser [33]. The vertical line CD represents the decomposition of C-S-H gel into silica gel. For the convenience of subsequent discussions, dissolution equilibrium between C_s^{Ca} and C_l^{Ca} is expressed as function $C_{s,x,t}^{Ca}$=C_s^{Ca} $(C_{l,x,t}^{Ca})$, where x and t are position and time respectively. There should be a governing equation for the conservation of calcium ions during the dissolution process, as shown in eq (5-3):

$$\left(C_{s,x,t}^{Ca} - C_{s,x,t}^{Ca\ \prime}\right)\left(1 - \rho_{x,t}\right) + \left(C_{l,x,t}^{Ca} - C_{l,x,t}^{Ca\ \prime}\right)\rho_{x,t} = 0 \tag{5-3}$$

In which, $C_{s,x,t}^{Ca}$ and $C_{l,x,t}^{Ca}$ is concentration in solid phase and in pore solution after reaching dissolution equilibrium respectively and satisfying $C_{s,x,t}^{Ca}$=C_s^{Ca} $(C_{l,x,t}^{Ca})$. $C_{s,x,t}^{Ca\ \prime}$ and $C_{l,x,t}^{Ca\ \prime}$ is concentration in solid phase and in pore solution before reaching dissolution equilibrium respectively. In the process of calcium releasing, the dissolution process is faster than the diffusion process, and it can be considered that the process of reaching dissolution equilibrium in leaching process is completed instantaneously. Considering the diffusion process and the dissolution process together, their change on C_s^{Ca}-C_l^{Ca} figure is shown in the supplementary figure in Figure 5-1.

Each point on the C_s^{Ca}-C_l^{Ca} figure represents a state. Points above the curve $C_{s,x,t}^{Ca}$=C_s^{Ca} $(C_{l,x,t}^{Ca})$ will gradually return to the equilibrium state through dissolution of solid phase, while points below the cure will return to the curve through precipitation. Whether it is dissolved or precipitated, calcium is conserved, that is the calcium content in solid phase decreases and the calcium ions in the liquid phase increase, which resulting point moves to the lower right corner on the C_s^{Ca}-C_l^{Ca} figure, such as 1' →1, 2' →2, and so on. During the diffusion process, the calcium ion concentration in the pore solution decreases while the calcium content in the solid phase remains unchanged, that is, point moves to the left horizontally such as 0→1', 1→2', and so on. The diffusion process and the dissolution process alternate, making the trajectory of the points appear jagged on the C_s^{Ca}-C_l^{Ca} figure, and the calcium in the solid phase is continuously lost, and this is an ideal picture of leaching process.

With the dissolution of calcium, the porosity of the sample also changes, which is mainly caused by the dissolution of calcium hydroxide and the decalcification of C-S-H. The change in porosity is therefore quantified by eq (5-4):

$$\Delta\rho^{Ca} = \frac{MW_{\mathrm{CH}}}{d_{\mathrm{CH}}}(C_{s,ini}^{Ca} - C_{s,x,t}^{Ca}) \tag{5-4}$$

In which, MW_{CH} is molar mass of calcium hydroxide, d_{CH} is density of calcium hydroxide. For the dissolution of portlandite and the decalcification of C-S-H gel, the release of calcium occurs simultaneously with the release of hydroxide ions, and their stoichiometry is Ca^{2+}: OH^- = 1:2, which makes it possible to consider the reduce of calcium concentration in solid phase all equivalent to the dissolution of portlandite.

5.2.3 Integrated description of SiTraM

After making many modifications on the diffusion coefficient, the differential equations describing this process become very complex, and it is difficult to obtain the analytical solution from the Fick's second Law. the more common solution is to calculate the numerical solution by discretization and difference method. Taking the discretization and modelling of diffusion in one dimension as an example, the model is shown in Figure 5-2:

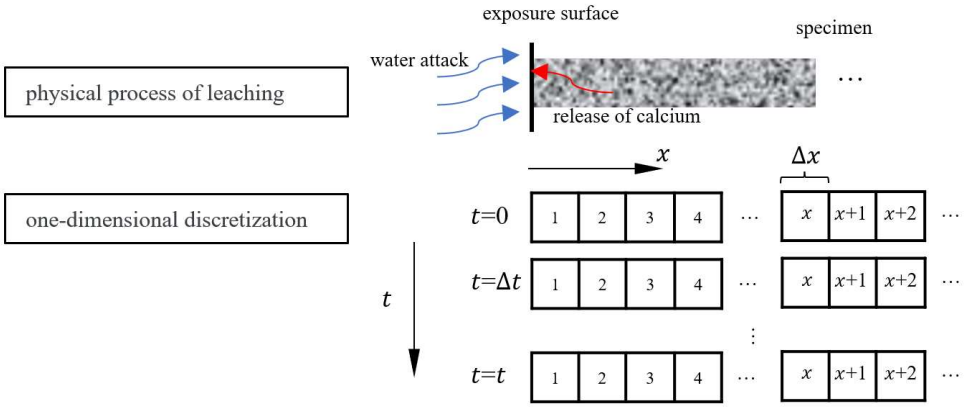

Figure 5-2 Discretization and modelling of diffusion in one dimension

From the Fick's second Law, concentration of calcium ion in pore solution in each cell can be calculated as eq (5-5):

$$C_{x,t+1} = C_{x,t} + D\left(\frac{\Delta t}{(\Delta x)^2}\right)[(C_{x+1,t} - C_{x,t}) - (C_{x,t} - C_{x-1,t})] \tag{5-5}$$

In which, Δt and Δx is time interval and position interval of sampling. $C_{x,t}$ is the concentration of cell at coordinate of x and time t. $[(C_{x+1,t} - C_{x,t}) - (C_{x,t} - C_{x-1,t})]$ is the second order difference of concentration.

Considering influence of mutual diffusion, D is replaced by D_{ij}, and eq (5-5) turns into:

$$C_{x,t+1}^{i} = C_{x,t}^{i} + \sum_{j=1}^{n_s} \left\{ D_{ij,x,t} \left(\frac{\Delta t}{(\Delta x)^2} \right) \left[\left(C_{x+1,t}^{i} - C_{x,t}^{i} \right) - \left(C_{x,t}^{i} - C_{x-1,t}^{i} \right) \right] \right\} \quad (5\text{-}6)$$

Considering influence of pore structure, eq (5-6) turns into:

$$C_{x,t+1}^{i} = C_{x,t}^{i} + \frac{\rho_{x,t}}{\tau_p} \sum_{j=1}^{n_s} \left\{ D_{ij,x,t} \left(\frac{\Delta t}{(\Delta x)^2} \right) \left[\left(C_{x+1,t}^{i} - C_{x,t}^{i} \right) - \left(C_{x,t}^{i} - C_{x-1,t}^{i} \right) \right] \right\} \quad (5\text{-}7)$$

SiTraM is roughly integrated into Figure 5-3:

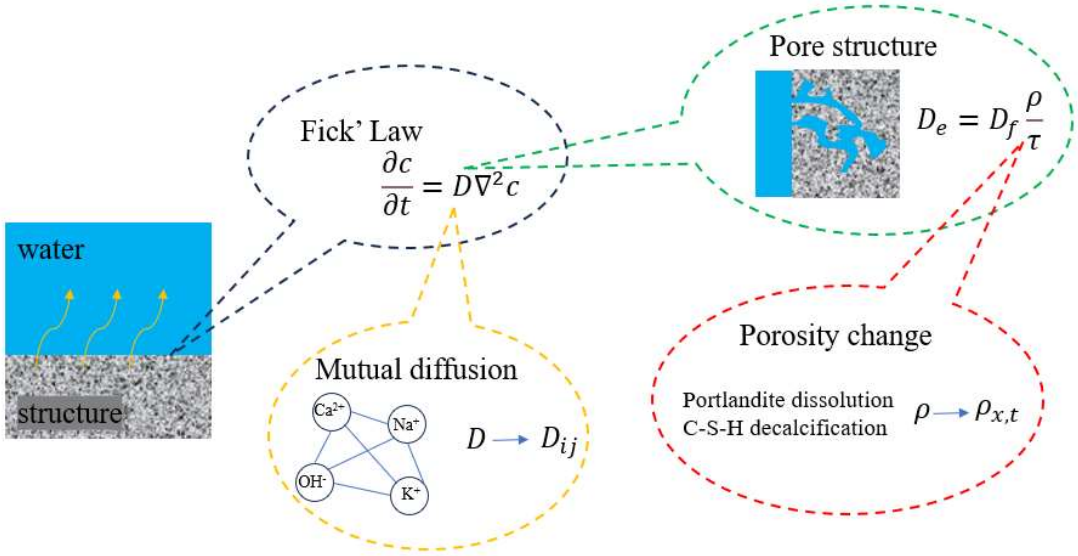

Figure 5-3 Simultaneous ion transport model (SiTraM)

5.3 EVALUATION OF CEMENT-BASED MATERIALS UNDER LEACHING

With SiTraM model, and image analysis data obtained from CHAPTER 4, we can conduct valuable discussions on the durability of cement-based materials under leaching process. Simulation of experimental specimens were first carried out in order to verify the rationality of the simulation process. Subsequent simulations of the concrete under leaching will provide useful data for durability evaluation.

5.3.1 Modeling of experimental specimens

(1) Plain hydrated cement paste

The SiTraM model involves the release of portlandite in the solid phase during leaching process, while one of the most intuitive outputs of the CT image is the dissolution front of portlandite. this gives us an idea to verify

the reliability of SiTraM model as well as the data obtained from CHAPTER 4, that is, to obtain the dissolution front of portlandite through simulation and compare it with the CT image. Section 4.2.3 shows the position of dissolution front for 5N specimen under different leaching period, and corresponding equivalent depth. Here we conducts two-dimension simulation based on single CT image. Figure 5-4 shows the discretization and modelling of plain cement paste (5N specimen).

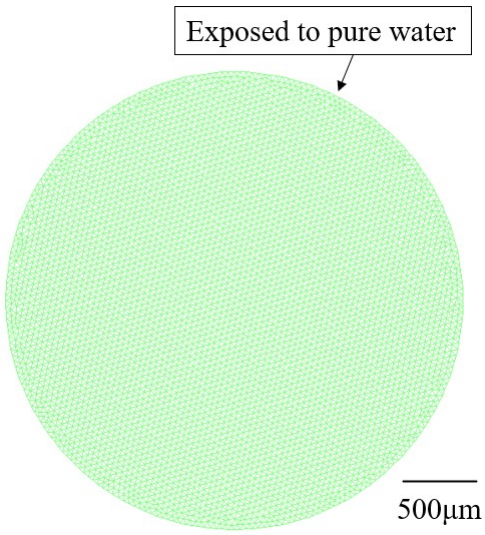

Figure 5-4 Discretization and modelling of plain cement paste under leaching

In the simulation, composition of cement paste, diffusion coefficient of calcium ion in bulk cement paste are required to determined. Oxide composition by mass of cement used in this research is 65.01 % CaO, 21.41 % SiO_2, 4.84 % Al_2O_3, 3.2 % Fe_2O_3, 1.08 % MgO and 2.02 % SO_3. The clinker composition can be estimated by applying Bogue equations, and calculated as 51.49 % C_3S, 25.41% C_2S, 7.41% C_3A and 9.74% C_4AF. When the water to cement ratio of specimen (here, 0.6), as well as the chemical composition of cement, are known, the portlandite content of hydrated cement paste can be calculated as follows:

$$2\ \underbrace{C_3S}_{228g/mol} + 7H \rightarrow C_3S_2H_4 + 3\ \underbrace{CH}_{74g/mol}$$

$$2\ \underbrace{C_2S}_{162g/mol} + 5H \rightarrow C_3S_2H_4 + \underbrace{CH}_{74g/mol}$$

$$M_{CH} = x \cdot C \cdot \frac{3 \times 74}{2 \times 228} + y \cdot C \cdot \frac{74}{2 \times 162}$$

In which, x and y are mass fraction of Alite (C_3S) and Belite (C_2S) in cement. M_{CH} is portlandite content in hydrated cement paste. C is mass of cement used per unit volume of hydrated cement paste.

Diffusion coefficient of calcium ion in bulk cement paste changes automatically governed by the SiTraM

model, and the initial diffusion coefficient of calcium ion in cement paste referred from Table 4-1, calculated diffusion coefficient of calcium ion of non-leached region was used. Initial diffusion coefficient of calcium ion and porosity of intact hydrated cement paste with different water to cement ratio were selected and given in table 5-1. The porosity of different specimen with different water to cement ratio was obtained by sampling on the corresponding CT images stack and conducting binary processing. As an example, Figure 5-6 shows sampling on the CT images stack of 5N0d, and each VOI is with size of 100 × 100 × 100. The average porosity of all sampled VOIs is considered to be the porosity of intact hydrated cement paste with water to cement ratio equal to 0.5.

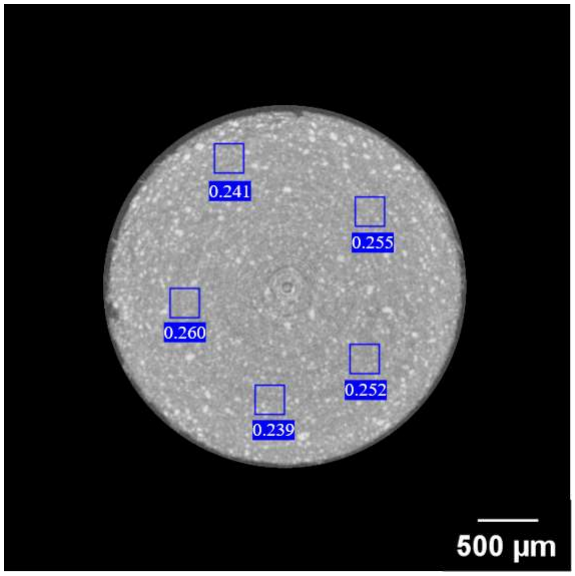

Figure 5-5 Sampling on 5N0d specimen and corresponding porosity

Table 5-1 Properties of intact hydrated cement paste

Intact hydrated cement paste (W/C = 0.5)	
Diffusion coefficient of calcium ion (cm^2/s)	1.17×10^{-8}
Porosity	0.249
Intact hydrated cement paste (W/C = 0.6)	
Diffusion coefficient of calcium ion (cm^2/s)	1.36×10^{-8}
Porosity	0.298

The simulated period is also consistent with the experiment, which is 7, 15, 60, and 120 days. Comparing the portlandite content in solid phase in simulation and the actual portlandite dissolution front can verify the reliability of the simulation method. Figure 5-6 shows simulation result of portlandite concentration in solid phase for 5N and 6N specimens.

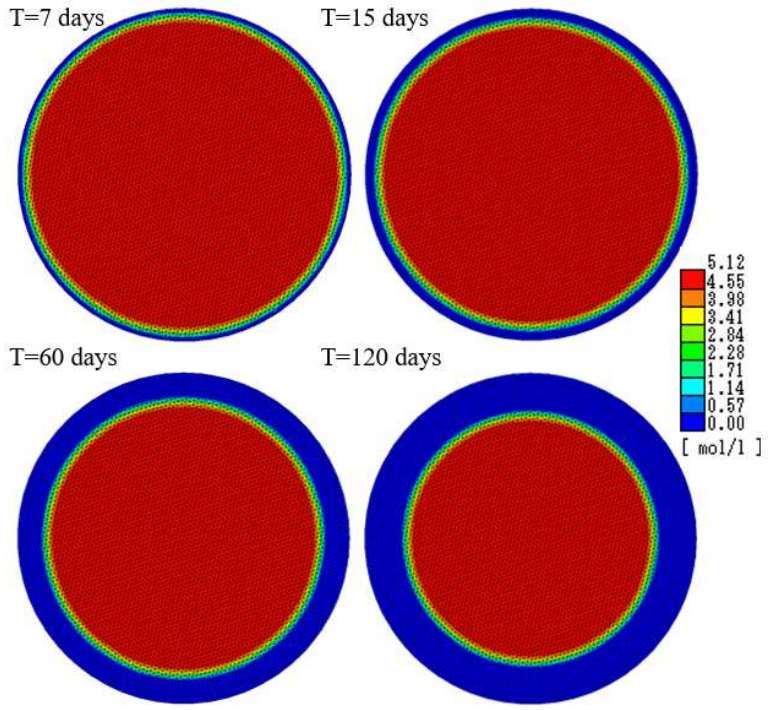

(a) W/C = 0.5

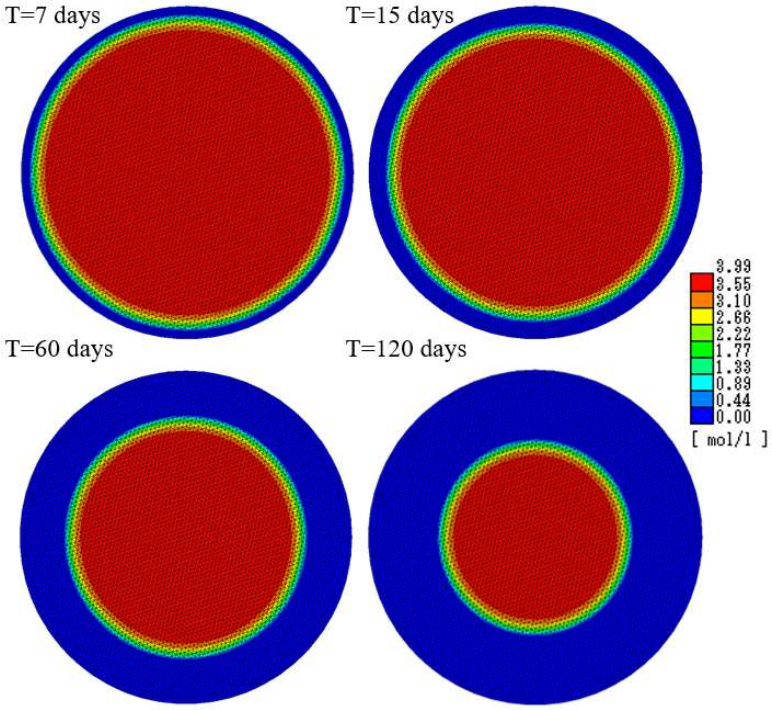

(b) W/C = 0.6

Figure 5-6 Simulation result of portlandite concentration in solid phase for 5N and 6N specimens

If we assume the position where the portlandite concentration is equal to half of the original concentration as the simulated portlandite dissolution front, depth of each simulated portlandite dissolution front can be obtained.

Figure 5-7 shows comparison of dissolution front depth between simulation and CT images. It can be seen that simulated dissolution front depth basically consistent with the equivalent depth, which reflects the reasonability of SiTraM model and the obtained images analysis data.

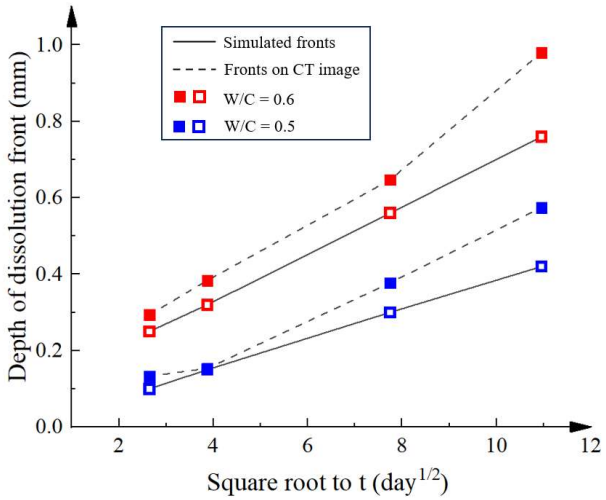

Figure 5-7 Comparison of dissolution front depth between simulation and CT images

Under the given assumption, simulation results are smaller than the experimental results, and the gap between simulation and experiment increases as time increases. Although the SiTraM model considers the influence of pore structure on the leaching process and quantifies changes in pore structure through quantifying change in porosity, changes in tortuosity are not included in the SiTraM model. This actually makes the SiTraM model's evaluation of leaching deterioration underestimated, which may be why the simulation results are lower than the experimental results.

(2) Aggregate containing specimen

Here, taking a specimen containing a limestone as aggregate with a water to cement ratio of 0.6 as an example (6LN60d specimen), retraces the path in section 4.3 to quantify the transport properties of non-leached region and ITZ. Then the obtained data and SiTraM model were used to simulate the entire process to verify the rationality of this method in simulating the influence of ITZ on leaching process. CT image of 6LN60d is shown in Figure 5-8, with the following marks: blue and yellow lines outline dissolution front of portlandite and aggregate profile respectively.

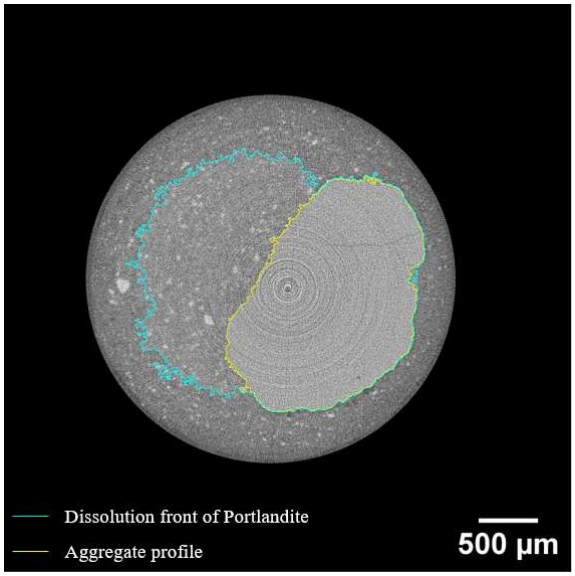

Figure 5-8 CT image of 6LN60d

In order to obtain the required input of SiTraM, VOIs were select from the stack, including region adjacent to the aggregate (VOI A) and region of non-leached region, or sound cement paste region (VOI B).

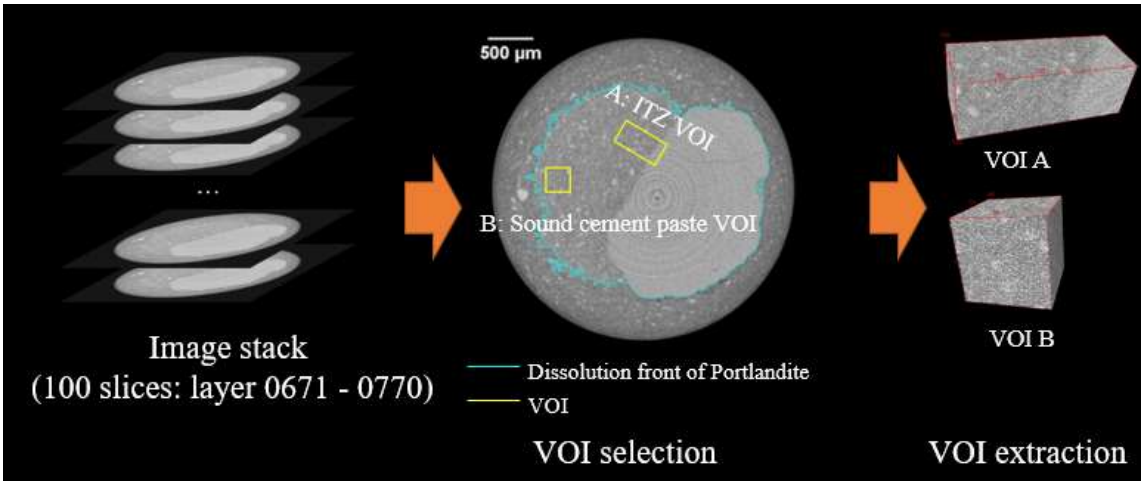

Figure 5-9 Extraction of VOIs

Extracting pore structure and preforming random walk simulation, as shown in Figure 5-10, transport properties, i.e., calculated diffusion coefficient of calcium ion, of sound cement paste and ITZ region are shown in Table 5-2.

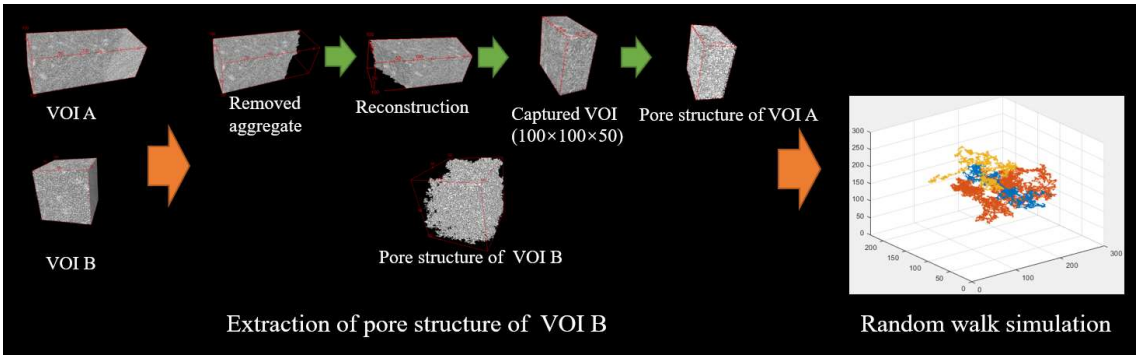

Figure 5-10 Extraction of pore structure and preforming random walk simulation

Table 5-2 Transport properties of sound cement paste and ITZ region

	Diffusion coefficient (cm^2/s)	Porosity
ITZ	3.69×10^{-7}	0.60
Sound cement paste	1.36×10^{-8}	0.30

Two-dimensional model was built on basis of single CT slice of 6LN60d specimen (layer 0720). Figure 5-11 shows discretization of 6LN60d.

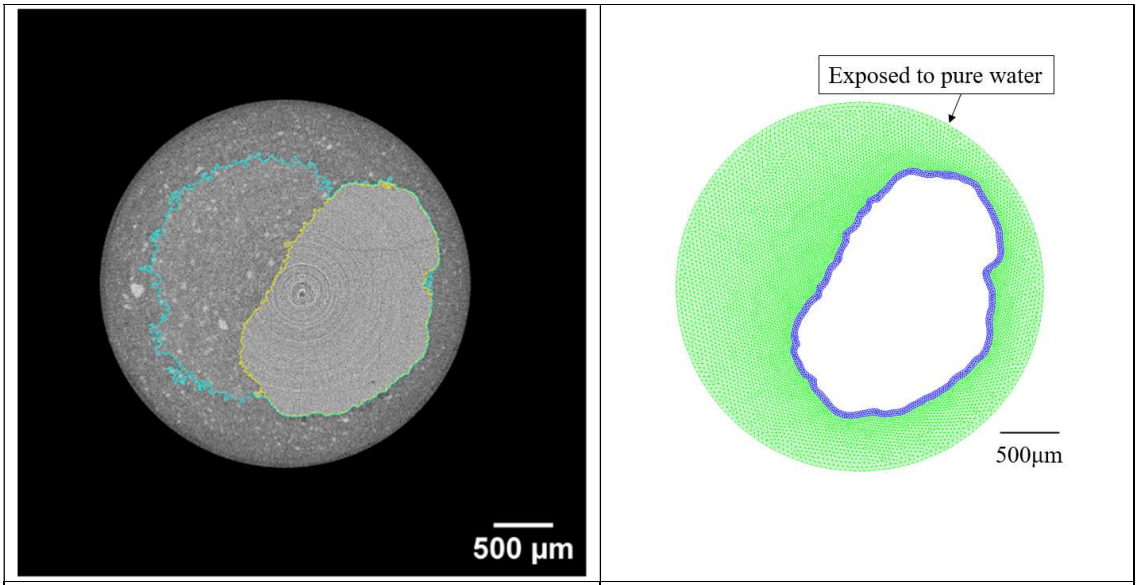

(a) single slice CT image (6LN60d layer:0720) | (b) two-dimensional model

Figure 5-11 Discretization of 6LN60d

Based on the obtained results, the input parameters of SiTraM are selected as shown in Table 5-3:

Table 5-3 Parameter selection of sound hydrated cement paste and ITZ region

Sound hydrated cement paste	
Diffusion coefficient of calcium ion (cm^2/s)	1.36×10^{-8}
Porosity	0.30
ITZ	
Diffusion coefficient of calcium ion (cm^2/s)	3.69×10^{-7}
Porosity	0.6
Portlandite content	70 % (base on the content of intact hydrated cement paste)
Thickness	70 μm

Simulation period was set as 60 days, and result of portlandite concentration in solid phase after 60 days leaching is shown in Figure 5-12. It can be seen that simulated dissolution front is very close to the actual dissolution front, which verifies the reliability of the image analysis data and SiTraM model.

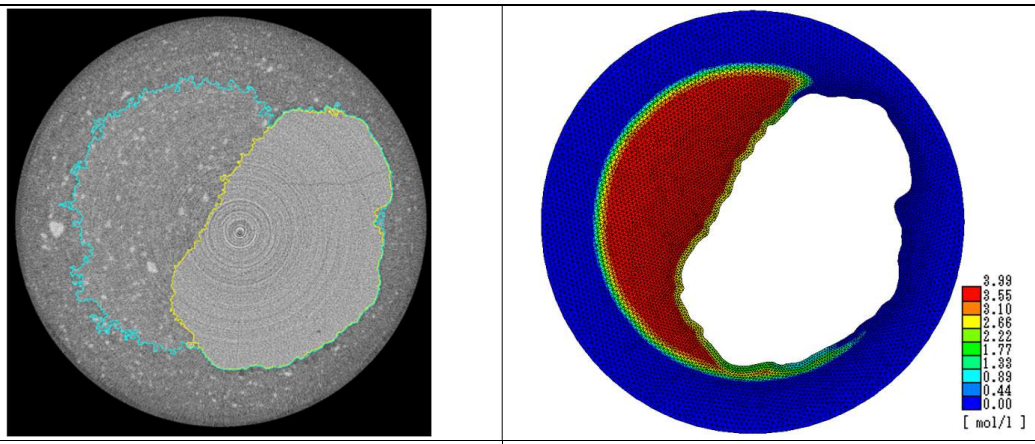

(a) Diffusion front from CT image (b) Portlandite concentration in solid phase

Figure 5-12 Comparison of dissolution front of portlandite in simulation and actual experiment

5.3.2 Modeling of concrete under 10 years leaching

In order to simulate the deterioration of concrete under leaching, we scanned an actual concrete section and established a multi-aggregate concrete section model, as shown in Figure 5-13. The left side of the model is assumed being exposed to water. Each aggregate in the model is surrounded by ITZ with a thickness of 70 μm. It should be noted that there is difference in portlandite content and porosity between the mortar phase in concrete and hydrated cement paste in aforementioned hardened cement paste. Moreover, under effect of fine aggregate, including dilution effect and tortuosity effect, the diffusion coefficient in mortar is also different from bulk cement paste. Previous research provides a method for estimating diffusion coefficients in mortars based on sand content [167] [168]. Table 5-4 shows parameter used in concrete simulation. The time node of outputting simulation result is 720 hours (one month), 3600 hours (five months), 7200 hours (ten months), 21600 hours (2.5 years), 43200 hours

(five years), 72000 hours (8 years and 4 months) and 90000 hours (around 10 years). Figure 5-14 shows simulation result of portlandite concentration in solid phase at different simulated time. It should be noted that the concentration of portlandite in mortar is lower than that in hydrated cement paste due to diluted effect of fine aggregate.

Table 5-4 Parameter selection of intact mortar and ITZ region

Sound mortar	
Diffusion coefficient of calcium ion (cm^2/s)	4.09×10^{-9}
Porosity	0.12
ITZ	
Diffusion coefficient of calcium ion (cm^2/s)	9.63×10^{-8}
Porosity	0.6
Portlandite content	70 % (base on the content of intact hydrated cement paste)
Thickness	70 μm

(a) Scanned concrete section

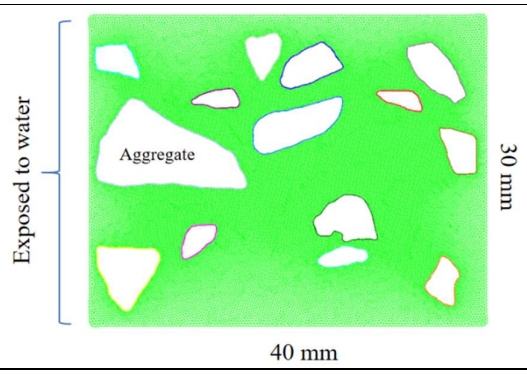

(b) Two-dimensional model

Figure 5-13 Discretization of concrete section

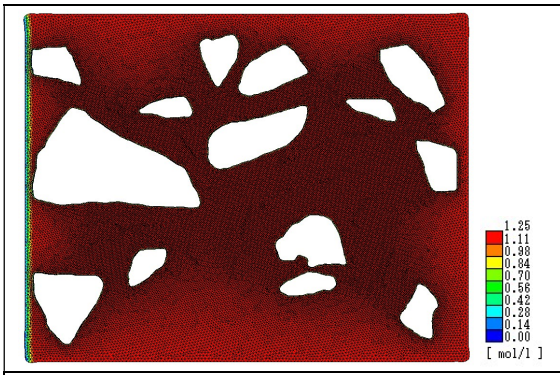

(a) 720 hours (one month)

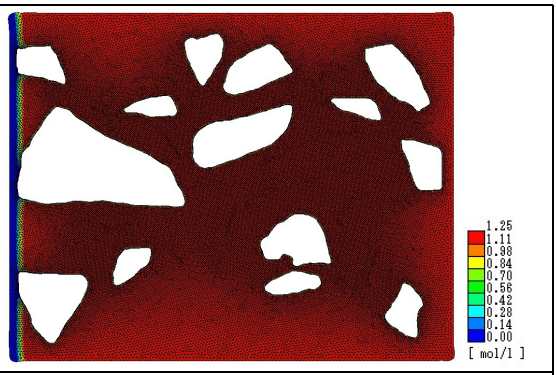

(b) 3600 hours (five months)

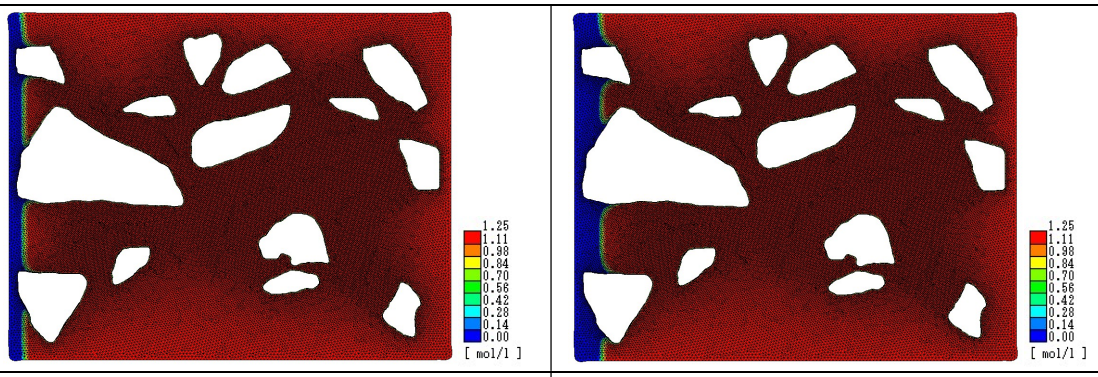

(c) 7200 hours (ten months)

(d) 21600 hours (2.5 years)

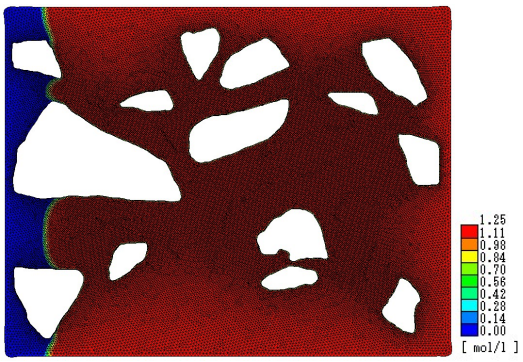

(e) 43200 hours (five years)

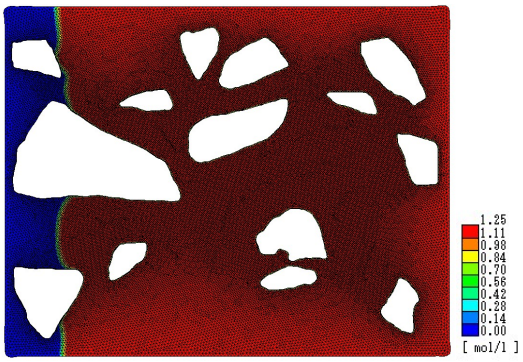

(f) 72000 hours (8 years and 4 months)

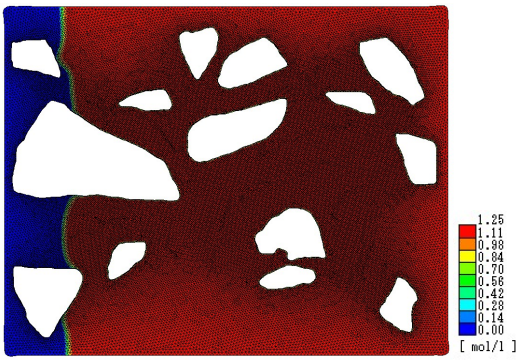

(g) 90000 hours (around 10 years)

Figure 5-14 Result of portlandite concentration in solid phase at different leaching period in concrete

Similarly, we take the position where the portlandite concentration in solid phase is equal to half of the initial concentration as the position of the dissolution front of portlandite, and focus the perspective near the aggregate, as shown on Figure 5-15. It can be seen that the dissolution front progresses basically parallel to the interval concrete but progresses deeper along edge of aggregate.

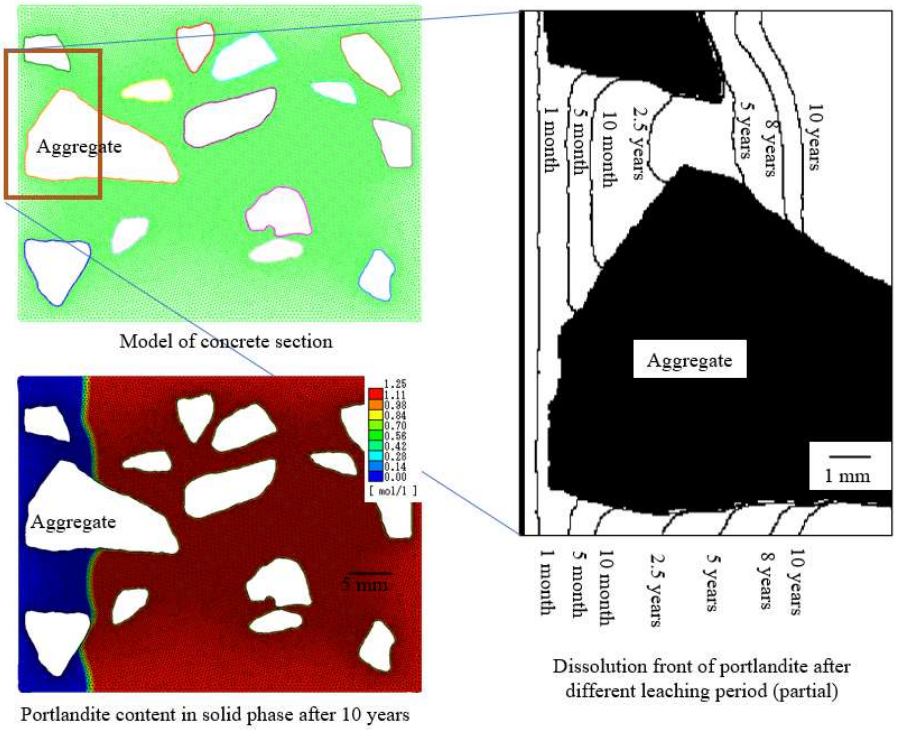

Figure 5-15 Progress of dissolution front near aggregate

Figure 5-16 shows progress rate of dissolution front in bulk mortar and under effect of ITZ. Part of model is selected, and the position of dissolution front near the aggregate (red line) as well as in bulk mortar (black line) under different leaching period were extracted. Result shows that after 10 years of leaching deterioration, depth of dissolution front in bulk mortar is around 6.2 mm, while for region under ITZ effect is around 7.2 mm.

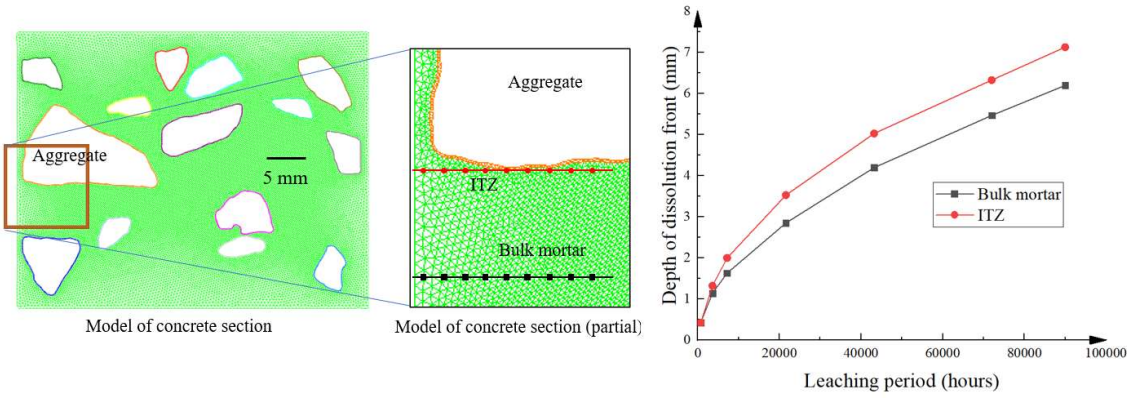

Figure 5-16 Progress of dissolution front in bulk mortar and under effect of ITZ

5.4 STRONTIUM ION DIFFUSING IN CONCRETE DURING LEACHING

In engineering practice, solvent that cause leaching deterioration may also contain other harmful components. In the background of Fukushima nuclear accident, water was continuously injected into the shell to cool the core after the accident. The cooling water in direct contact with the core will contain harmful substance such as cesium ion (Cs^{+}) and strontium ion (Sr^{2+}). Due to the presence of concentration gradients, these harmful substance will diffuse into the structure, and the diffusion depth of harmful substance is related to the treatment of concrete materials in the final demolition of nuclear power plants. To correctly evaluate the diffusion depth, the following factors need to be considered: on the one hand, diffusion process of harmful substance couples the leaching deterioration of concrete; on the other hand, carbonation of concrete structures in nuclear power plant during normal service periods before the accident may also affect the diffusion of harmful substance. Here, a one-dimensional model was built, and diffusion of strontium ion (Sr^{2+}) in hydrated cement paste was taken as an example to describe the evaluation method of the diffusion of harmful substance into the cement-based materials during leaching process. Moreover, basing on the result in previous part of this research, simplification, or improvement in two aspects has also been tentatively proposed. First is a simplification of the progress of dissolution front, and second is considering change in tortuosity.

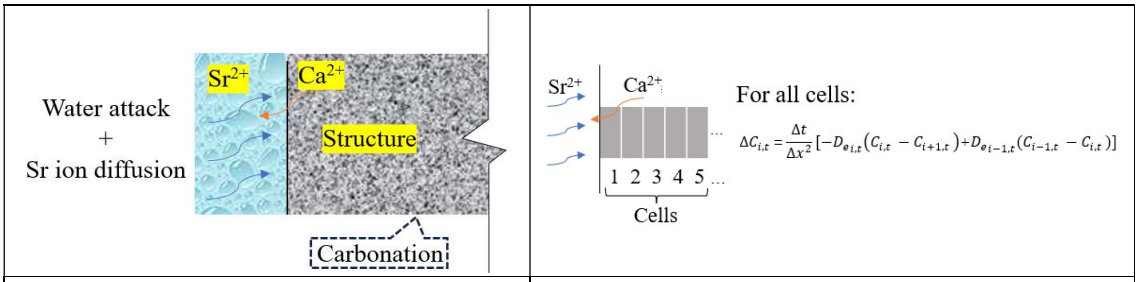

(a) Leaching and strontium ion diffusion | (b) discretization

Figure 5-17 Modeling of leaching and strontium ion diffusion occurring simultaneously

The evaluation model presented in this section is still based on Fick's Law. Figure 5-17 (a) shows a common picture of leaching and strontium ion diffusion occurring simultaneously. Carbonation of structure in normal service stage is also considered. While Figure 5-17 (b) shows the discretization of the model. The structure is divided into different cells. In each time step, ion diffusion occurs under the concentration gradient between the cell and the cell before and after it. Through difference method, change of ion concentration in each cell is calculated. Then the ion concentration in all cells are updated and the calculation of the next time step is performed.

Both experimental results and simulated results based on the SiTraM model show that the progress of depth of dissolution front is proportional to the square root of time. Therefore, model can be simplified by directly calculating the position of the dissolution front through the leaching period, dividing the leached region and non-leached region, and calculating the porosity change of each cell accordingly. Table 5-5 shows calculating formula of depth of dissolution front in specimen with water to cement ratio equal to 0.5, 0.6 and carbonated specimen.

For carbonated specimen, there is no dissolution front and according to analysis from section 4.2.3 , transport properties shows little difference after leaching for carbonated specimen.

Table 5-5 Evaluation of dissolution front (days, mm)

Specimen	W/C=0.5	W/C=0.6	Carbonated specimen
Depth of dissolution front	$d = 0.052\sqrt{t}$	$d = 0.084\sqrt{t}$	-

The consideration of changes in tortuosity during leaching process is an improvement to the SiTraM model. This research gave a method for evaluating transport properties through high-precision CT images and random walk simulation. However, it is impossible to perform computed tomography on every time interval of the specimen to evaluate transport properties. It should be noted that tortuosity of the pore structure has a subtle relationship with the porosity. It is assumed that the higher porosity means larger pore size and more connected pores, which usually means lower pore tortuosity. Previous research have given empirical formulas to describe the relationship between porosity and tortuosity in porous media [169], as shown in eq (5-8):

$$\tau = \rho^{-a} \tag{5-8}$$

In which, τ is tortuosity, ρ is porosity and a is a parameter.

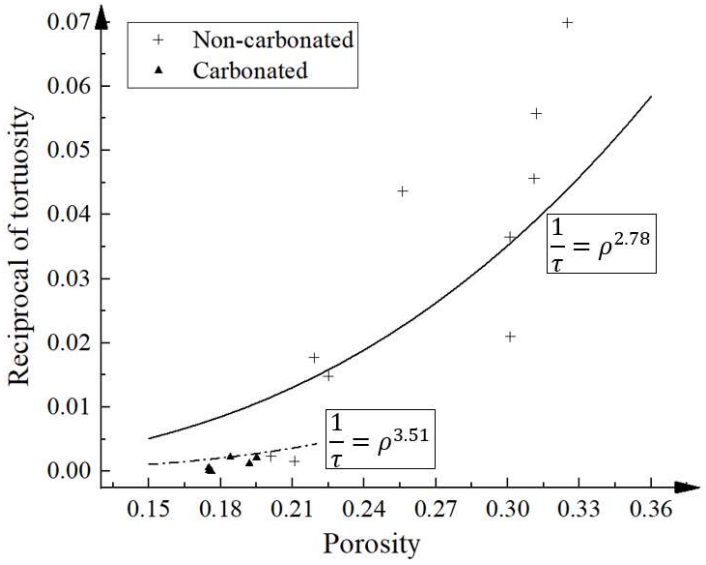

Figure 5-18 1⁄τ-ρ relationship from Random walk simulation

Using the transport properties data and porosity data obtained from section 4.3 , parameter a can be determined. Figure 5-18 shows determination of parameter a for both carbonated specimen and non-carbonated specimen. Due to the formation of calcite, carbonated samples may have different pore structure characteristics

from non-carbonated samples. When calculating parameter a, they are divided into two groups and calculated separately. It should be noted that the fitting results are actually not ideal. This is due to the uncertain relationship between porosity and tortuosity.

Numerical calculation simulates strontium ion (Sr^{2+} ion) diffusion process for 10-year in concrete under carbonation and following leaching deterioration. Water attack results in alteration of hydrated cement paste and Sr^{2+} ion diffusion occurs simultaneously. The model presented in this section can be integrated into Figure 5-19. One dimension model for Sr ion diffusion in concrete was developed governed by Fick's law. In each time interval, amount of diffusing Sr^{2+} ions between cells is calculated and concentration of Sr^{2+} ion in each cell is updated. Amount of released calcium is estimated as shown in CHAPTER 4 and porosity change of each cell is calculated. Sequential diffusion coefficient change of Sr^{2+} ion is calculated for each cell in accordance with pore structure change which is governed by the relationship between porosity and tortuosity. In the following time interval, diffusion of Sr^{2+} ion is calculated based on the updated parameters until time reach 10 years. Diffusion coefficient of Sr^{2+} ion in free liquid is 7.12×10^{-10} m^2/s, and the distribution coefficient is $K_d = 0.2$ [170]. Distribution coefficient quantifies the distribution of solute in different phase. Here, K_d evaluates the sorption and reaction between solid phase and Sr^{2+} ion.

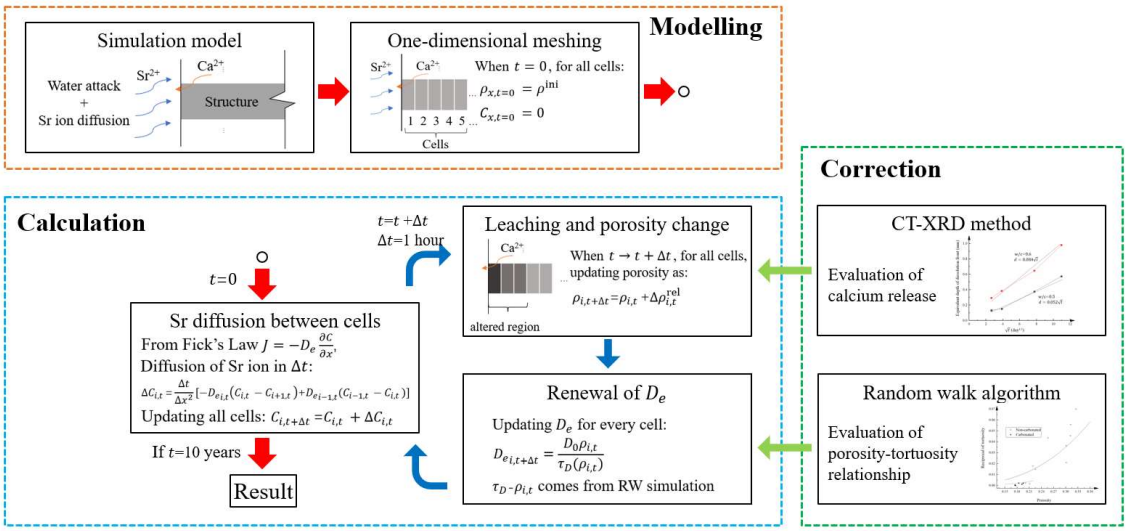

Figure 5-19 Schematic diagram of calculation

Result of simulation of simultaneous diffusion of Sr^{2+} ion is given in Figure 5-20. Condition A and B are non-carbonated structure with different water to cement ratio, while condition C and D are carbonated structure. Condition E simulates diffusion of Sr^{2+} not coupling factors of leaching deterioration and carbonation. For comparing different condition, the depth of the half concentration of Sr^{2+} ion is taken as the diffusion depth. Diffusion depth result of each condition is 15.6 mm, 19.7 mm, 9.9 mm, 13.8 mm, and 16.2 mm respectively. Diffusion depth progresses deeper for structure with higher water to cement ratio, because of higher porosity. For comparison between non-carbonated and carbonated structure, diffusion depth progress smaller in carbonated

structure. Portlandite is converted into calcite during carbonation process, which denser pore structure and restrict the diffusion of Sr^{2+} ion. It means that the carbonation of structure in Fukushima nuclear plant is benefit to the resistance to simultaneous diffusion of Sr^{2+} ion in leaching deterioration. For the effect of leaching deterioration, results from condition B and E show that diffusion depth progress deeper in structure under leaching. Not considering leaching impact, the diffusion of Sr^{2+} ion will be underestimated.

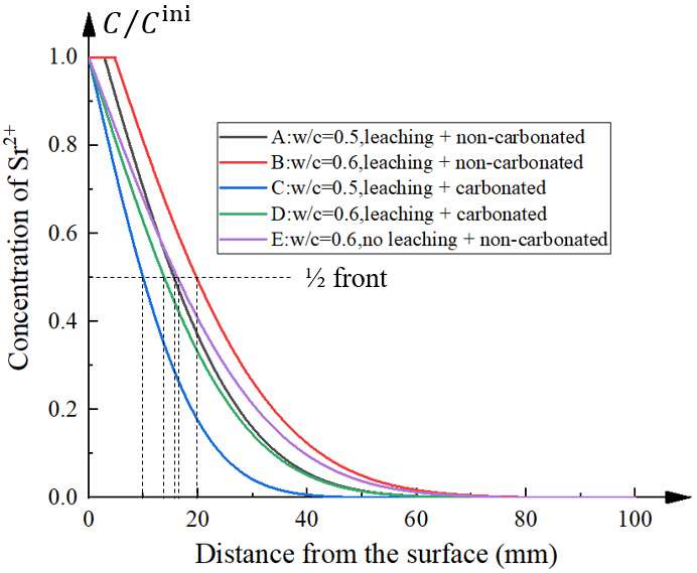

Figure 5-20 Concentration of Sr^{2+} ion after 10 years exposure

5.5 SUMMARY

This chapter firstly introduces simultaneous ion transport model (SiTraM), which considers the influence of mutual diffusion, the influence of pore structure on diffusion, and the influence of ion exchange between liquid and solid phase on pore structure. Subsequently, the image analysis data obtained from CHAPTER 4 were used as model input to simulate the experimental specimen. Simulation on plain hydrated cement paste specimen with water to cement ratio equal to 0.5 shows that simulated dissolution front depth basically consistent with the equivalent depth, which reflects the reasonability of SiTraM model and the obtained images analysis data. The phenomenon that the simulated result of dissolution front is smaller than experimental result may come from the limitation that SiTraM model does not consider the change of tortuosity. Simulation on specimen with single aggregate inside shows that it is reasonable to use the image reconstruction metho proposed in this research to quantify the transport properties of ITZ. Moreover, basing on SiTraM model, the simulation of concrete under leaching deterioration was also conducted. Result shows that after 10 years of leaching deterioration, depth of dissolution front in bulk mortar is around 6.2 mm, while for region under ITZ effect is around 7.2 mm.

During the leaching process, harmful components in the solvent will diffuse into the cement-based material at the same time. In order to evaluate this process, this chapter uses the diffusion of strontium ions as an example to establish a one-dimensional model. In this model, progress of dissolution front is simplified, and change in

tortuosity during leaching is also considered. The simulation results under different conditions such as different water to cement ratios, with or without carbonation, and whether the effect of leaching on Sr^{2+} ion diffusion is considered show that, lower diffusion speed was verified in lower water to cement ratio, carbonation process also slows down diffusion of Sr^{2+} ion, and if the effect of leaching deterioration was not considered, about 19% lower depth was underestimated.

CHAPTER 6 CONCLUSIONS

6.1 GENERAL CONCLUSION

In this research, leaching deterioration of cement-based materials was investigated, by using the integrated non-destructive CT-XRD method on tiny specimen of 3 mm in diameter and 6 mm in height. Compared with conventional research method, the CT-XRD method can investigate the natural leaching behavior within a relatively short period which made the research more effective. In addition, with the support of CT-XRD method, the pore structure of cement-based materials under the influence of leaching deterioration can be observed visually. Applying image processing techniques and random walk algorithm, the transport properties of different regions within specimens were quantified. Lastly, prediction of leaching deterioration of cement-based materials was conducted on basis of transport properties evaluated result.

Based on this study, general conclusions are summarized as follows:

Firstly, the application of integrated CT-XRD method on leaching related research was effective and reliable.

1) Using CT-XRD method to analyze the leaching behavior of non-carbonated tiny specimen up to 120 days in pure water showed that the leached region and non-leached region can be distinguished according to the dissolution of portlandite. It was also shown that the depth of the boundary between leached region and non-leached region, i.e., dissolution front of portlandite, was proportional to the square root of the immersion period, which is consistent with the results obtained by conventional methods.

2) The CT-XRD method also exhibited the potential in detecting effects of carbonation and seawater immersion. Analysis on carbonated specimen showed that the majority of portlandite was converted into calcite in the accelerated carbonation process, resulting in less calcium released from specimen during the leaching process and little change in transport properties. Carbonated specimen provided higher resistance to leaching. Analysis on seawater immersed specimens showed that the ionic environment-induced phase transition, such as the reformation of ettringite, the formation of Friede's salts and the formation of a surface brucite layer were revealed.

Secondly, impact of ITZ on leaching and transport properties of different region was evaluated.

3) Dissolution front of the portlandite was extracted for single aggregate containing specimen after 33 days leaching at both 20 ℃ and 80 ℃. Results showed that the dissolution front became deeper for higher temperatures, and the dissolution front basically remained circular. However, there is a significant inward invasion for the dissolution front where it intersects the aggregate profile, which indicated that the more porous ITZ promotes leaching deterioration.

4) Coupled CT image processing technique and random walk algorithm, the transport properties of leached region, non-leached region and ITZ were evaluated. The diffusion coefficient of calcium ion in the leached region was approximately 50 times larger than that of the non-leached region in the specimen under 20℃ leaching for 33 days and approximately 100 times larger than in the specimen under 80℃ leaching, while the diffusion coefficient of calcium ion in ITZ was about 10 times larger than that of the non-leached region.

Lastly, leaching deterioration was predicted based on the evaluated results of transport properties.

6) Prediction of portlandite dissolution of concrete exposed to water attack for 10 years using SiTraM model was conducted. Result showed that after 10 years of leaching deterioration, the depth of dissolution front in bulk mortar was around 6.2 mm, while for the region under impact of ITZ was around 7.2 mm.

7) In order to evaluate the impact of leaching deterioration on the diffusion of harmful substance in cement-based materials, one-dimensional diffusion model of Sr^{2+} ion that occurs simultaneously with leaching was developed. Result showed that the lower diffusion speed was verified in lower water to cement ratios while the carbonation process also slowed down the diffusion of Sr^{2+} ions. In case when the effect of leaching deterioration was considered, about 19 % larger depth of Sr^{2+} ions penetration was obtained.

6.2 RECOMMENDATIONS FOR FURTHER RESEARCH

6.2.1 More algorithms applicable in CT image data

This research applied a variety of image processing technologies and simulation algorithms on the basis of high-precision CT images, and obtains a series of convincing results, but this is not all that high-precision CT images can bring. Just in terms of extraction and analysis of pore structure, there is still a lot of room for improvement.

In this research, the extraction of pore space requires setting a threshold for binary process. However, a slight deviation in the threshold may lead to a huge change in the geometric structure of the pore space. The original unconnected pore clusters become the same connected pore cluster, which in turn affects the subsequent analysis. Developing better methods for extracting pore structure could improve related analytical methods.

The analysis of pore structure should not stop at parameters such as porosity and tortuosity. In the analysis of this research, it is actually assumed that the diffusion of ions in pores of different pore sizes is the same, and the influence of surface effects is ignored [171]. To study this involves analyzing the pore distribution, which requires new algorithms. In addition, the method used in this research to extract the pore structure is limited by the resolution of CT images and may not truly reflect the pore structure. At present, some researchers are trying to use the method of fractal mathematics for analysis [172][173], which can bring us new ideas.

6.2.2 Expansion and improvement of evaluated method

This research used obtained results of transport properties as input of model and make a benefited attempt to evaluate the deterioration of cement-based materials under leaching deterioration, which is also the intention of the study. However, the application is still limited, and the model is still rough. From the analysis of this research, there are two directions that need to be improved.

Studies of specimen leaching in seawater have shown that leaching in multiple ions environments can introduce reactions such as the formation of Friedel's salts, the conversion of brucite, and the reformation of

ettringite, which will affect the pore structure. How to incorporate these changes in simulations is one of the future focuses.

The change of porosity under leaching is relatively easy to assess, but the change in tortuosity is difficult to predict. The random walk algorithm used in this research can quantify the tortuosity, but it is not realistic to widely use it in simulation. How to better use porosity to predict changes in tortuosity is important.

6.2.3 Alteration of concrete with supplementary cementitious material (SCM) subject to leaching

In this research, the leaching behavior under the OPC system was studied using an originally developed transport properties analysis method. Due to durability requirements and the concept of green concrete, SCM materials are widely used in concrete. The addition of these materials causes cement-based materials to have different hydrated products, which will inevitably affect their behavior under leaching deterioration. The transport performance analysis method used in this research can also be applied to concrete with SCM materials, as a supplement mean of related research.

REFERENCE

[1] Global cement and concrete association. https://gccassociation.org/concretefuture/cement-concrete-around-the-world/. Accessed 10 October 2023.

[2] Chapman N, and Hooper A "The disposal of radioactive wastes underground." Proceedings of the Geologists' Association 123.1 (2012): 46-63.

[3] Yokozeki K, Watanabe K, Sakata N, and Otsuki. "Modeling of leaching from cementitious materials used in underground environment." Applied clay science 26.1-4 (2004): 293-308.

[4] Morton R J, and Struxness E G. "Ground disposal of radioactive wastes." American Journal of Public Health and the Nations Health 46.2 (1956): 156-163.

[5] de Larrard T, Benboudjema F, Colliat J B, Torrenti J M, and Deleruyelle F. "Concrete calcium leaching at variable temperature: Experimental data and numerical model inverse identification." Computational Materials Science 49.1 (2010): 35-45.

[6] Jain J, and Neithalath N. "Analysis of calcium leaching behavior of plain and modified cement pastes in pure water." Cement and Concrete Composites 31.3 (2009): 176-185.

[7] Haga K, Sutou S, Hironaga M, Tanaka S and Nagasaki S. "Effects of porosity on leaching of Ca from hardened ordinary Portland cement paste." Cement and concrete research 35.9 (2005): 1764-1775.

[8] Carde C, François R, and Torrenti J M. "Leaching of both calcium hydroxide and CSH from cement paste: Modeling the mechanical behavior." Cement and concrete research 26.8 (1996): 1257-1268.

[9] Carde C, and François R. "Effect of the leaching of calcium hydroxide from cement paste on mechanical and physical properties." Cement and Concrete Research 27.4 (1997): 539-550.

[10] Carde C, Escadeillas G, and François A H. "Use of ammonium nitrate solution to simulate and accelerate the leaching of cement pastes due to deionized water." Magazine of Concrete Research 49.181 (1997): 295-301.

[11] Jiang C, Jiang L, Tang X, Gong J, and Chu H. "Impact of calcium leaching on mechanical and physical behaviors of high belite cement pastes." Construction and Building Materials 286 (2021): 122983.

[12] Zhao H, Wu Z, Liu A, and Zhang L. "Numerical insights into the effect of ITZ and aggregate strength on concrete properties." Theoretical and Applied Fracture Mechanics 120 (2022): 103415.

[13] Erdem S, Dawson A R, and Thom N H. "Influence of the micro-and nanoscale local mechanical properties of the interfacial transition zone on impact behavior of concrete made with different aggregates." Cement and Concrete Research 42.2 (2012): 447-458.

[14] Jebli M, Jamin F, Garcia-Diaz E, El Omari M, and El Youssoufi M S. "Influence of leaching on the local mechanical properties of an aggregate-cement paste composite." Cement and Concrete Composites 73 (2016): 241-250.

[15] Hartwich P, and Vollpracht A. "Influence of leachate composition on the leaching behaviour of concrete." Cement and Concrete Research 100 (2017): 423-434.

[16] Kamali S, Moranville M, and Leclercq S. "Material and environmental parameter effects on the leaching of cement pastes: experiments and modelling." Cement and concrete research 38.4 (2008): 575-585.

[17] Stefanoni M, Angst U, and Elsener B. “Corrosion rate of carbon steel in carbonated concrete–A critical review.” Cement and Concrete Research 103 (2018): 35-48.

[18] Angst U, Moro F, Geiker M, Kessler S, Beushausen H, et al. “Corrosion of steel in carbonated concrete: mechanisms, practical experience, and research priorities–a critical review by RILEM TC 281-CCC.” RILEM Technical Letters 5 (2020): 85-100.

[19] Li L, and Wu M. “An overview of utilizing CO2 for accelerated carbonation treatment in the concrete industry.” Journal of CO2 Utilization 60 (2022): 102000.

[20] Rao N V, and Meena T. “A review on carbonation study in concrete.” IOP Conference Series: Materials Science and Engineering. Vol. 263. No. 3. IOP Publishing, 2017.

[21] von Greve-Dierfeld S, Lothenbach B, Vollpracht A, Wu B, Huet B, et al. “Understanding the carbonation of concrete with supplementary cementitious materials: a critical review by RILEM TC 281-CCC.” Materials and structures 53.6 (2020): 136.

[22] Van Gerven T, Van Baelen D, Dutré V, and Vandecasteele C “Influence of carbonation and carbonation methods on leaching of metals from mortars.” Cement and Concrete Research 34.1 (2004): 149-156.

[23] Garrabrants A C, Sanchez F, and Kosson D S. “Changes in constituent equilibrium leaching and pore water characteristics of a Portland cement mortar as a result of carbonation.” Waste Management 24.1 (2004): 19-36.

[24] Bye G C. Portland cement: composition, production and properties. Thomas Telford, 1999.

[25] Andersson K, Allard B, Bengtsson M, and Magnusson B. “Chemical composition of cement pore solutions.” Cement and Concrete Research 19.3 (1989): 327-332.

[26] Vollpracht A, Lothenbach B, Snellings R, and Haufe J. “The pore solution of blended cements: a review.” Materials and Structures 49 (2016): 3341-3367.

[27] Nixon P J, and Page C L. “Pore solution chemistry and alkali aggregate reaction.” Special Publication 100 (1987): 1833-1862.

[28] Yonezawa T, Ashworth V, and Procter R P M. “Pore solution composition and chloride effects on the corrosion of steel in concrete.” Corrosion 44.7 (1988): 489-499.

[29] Elsener B, and Rossi A. “Passivation of steel and stainless steel in alkaline media simulating concrete.” (2018): 365-375.

[30] Bertolini L, Elsener B, Pedeferri P, Redaelli E and Polder R B. Corrosion of steel in concrete: prevention, diagnosis, repair. John Wiley & Sons, 2013.

[31] Taylor H F W. Cement chemistry. Vol. 2. London: Thomas Telford, 1997.

[32] Buil M, Revertegat E, and Oliver J. “A model of the attack of pure water or undersaturated lime solutions on cement.” ASTM Special Technical Publication 1123 (1992): 227-241.

[33] Glasser L S D, Lachowski E E, Mohan K, and Taylor H F W. “A multi-method study of C3S hydration.” Cement and Concrete Research 8.6 (1978): 733-739.

[34] Taylor H F W, and Newbury D E. “Calcium hydroxide distribution and calcium silicate hydrate composition in tricalcium silicate and β-dicalcium silicate pastes.” Cement and concrete research 14.1 (1984): 93-98.

[35] Richardson I G. “The calcium silicate hydrates.” Cement and concrete research 38.2 (2008): 137-158.

[36] Mehta P K, and Monteiro P J M. Concrete: microstructure, properties, and materials. McGraw-Hill Education, 2014.

[37] Fick A (1855). “On liquid diffusion”. The London, Edinburgh, and Dublin Philosophical Magazine and Journal of Science. 10 (63): 30–39.

[38] Shafikhani M, and Chidiac S E. “Quantification of concrete chloride diffusion coefficient–A critical review.” Cement and Concrete Composites 99 (2019): 225-250.

[39] Tang L. “Concentration dependence of diffusion and migration of chloride ions: Part 1. Theoretical considerations.” Cement and concrete research 29.9 (1999): 1463-1468.

[40] Philibert J. “One and a half century of diffusion: Fick, Einstein before and beyond.” (2006).

[41] McNaught A D. Compendium of chemical terminology. Vol. 1669. Oxford: Blackwell Science, 1997.

[42] Gaboreau S, Grangeon S, Claret F, Ihiawakrim D, Ersen O, et al. “Hydration properties and interlayer organization in synthetic CSH.” Langmuir 36.32 (2020): 9449-9464.

[43] Sun J, Zhang W, Zhang J, and Hou D. “Molecular dynamics study the structure, bonding, dynamic and mechanical properties of calcium silicate hydrate with ultra-confined water: Effects of nanopore size.” Construction and Building Materials 280 (2021): 122477.

[44] Honorio T, Carasek H, and Cascudo O. “Water self-diffusion in CSH: Effect of confinement and temperature studied by molecular dynamics.” Cement and Concrete Research 155 (2022): 106775.

[45] Feldman R F, and Sereda P J. “A new model for hydrated Portland cement and its practical implications.” Engineering Journal 53.8-9 (1970): 53-59.

[46] Huang Q, Jiang Z, Gu X, Zhang W, and Guo B. “Numerical simulation of moisture transport in concrete based on a pore size distribution model.” Cement and Concrete Research 67 (2015): 31-43.

[47] Ma H, Hou D, Lu Y, and Li Z. “Two-scale modeling of the capillary network in hydrated cement paste.” Construction and Building Materials 64 (2014): 11-21.

[48] Garboczi E J. “Permeability, diffusivity, and microstructural parameters: a critical review.” Cement and concrete research 20.4 (1990): 591-601.

[49] Weiss W J, Spragg R P, Isgor O B, Ley M T, and Dam T V. “Toward performance specifications for concrete: linking resistivity, RCPT and diffusion predictions using the formation factor for use in specifications.” High Tech Concrete: Where Technology and Engineering Meet: Proceedings of the 2017 fib Symposium, held in Maastricht, The Netherlands, June 12-14, 2017. Springer International Publishing, 2018.

[50] Grathwohl P. Diffusion in natural porous media: contaminant transport, sorption/desorption and dissolution kinetics. Vol. 1. Springer Science & Business Media, 2012.

[51] Hertz H G. “Velocity Correlations in Aqueous Electrolyte Solutions from Diffusion, Conductance, and Transference Data. Part 1, Theory.” Berichte der Bunsengesellschaft für physikalische Chemie 81.7 (1977): 656-664.

[52] Felmy A R, and Weare J H. “Calculation of multicomponent ionic diffusion from zero to high concentration:

I. The system Na-K-Ca-Mg-Cl-SO_4-H_2O at 25 C." Geochimica et Cosmochimica Acta 55.1 (1991): 113-131.

[53] Felmy A R, and Weare J H. "Calculation of multicomponent ionic diffusion from zero to high concentration: II. Inclusion of associated ion species." Geochimica et Cosmochimica Acta 55.1 (1991): 133-144.

[54] Birnin-Yauri U A, and Glasser F P. "Friedel's salt, $Ca_2Al(OH)_6(Cl,OH)\cdot 2H_2O$: its solid solutions and their role in chloride binding." Cement and Concrete Research 28.12 (1998): 1713-1723.

[55] Neville A. "The confused world of sulfate attack on concrete." Cement and Concrete research 34.8 (2004): 1275-1296.

[56] Scrivener K L, Crumbie A K, and Laugesen P. "The interfacial transition zone (ITZ) between cement paste and aggregate in concrete." Interface science 12 (2004): 411-421.

[57] Prokopski G, and Halbiniak J. "Interfacial transition zone in cementitious materials." Cement and Concrete Research 30.4 (2000): 579-583.

[58] Constantinides G, Ulm F J. "The effect of two types of CSH on the elasticity of cement-based materials: Results from nanoindentation and micromechanical modeling." Cement and concrete research 34.1 (2004): 67-80.

[59] Gao Y, De Schutter G, Ye G, Tan Z, and Wu K. "The ITZ microstructure, thickness and porosity in blended cementitious composite: Effects of curing age, water to binder ratio and aggregate content." Composites part b: engineering 60 (2014): 1-13.

[60] Diamond S, and Huang J. "The ITZ in concrete–a different view based on image analysis and SEM observations." Cement and concrete composites 23.2-3 (2001): 179-188.

[61] Prentice I C, Farquhar G D, Fasham M J R, Goulden M L, Heimann M, et al. "The carbon cycle and atmospheric carbon dioxide." (2001).

[62] Šavija B, and Luković M. "Carbonation of cement paste: Understanding, challenges, and opportunities." Construction and Building Materials 117 (2016): 285-301.

[63] Winnefeld F, Leemann A, German A, and Lothenbach B. "CO_2 storage in cement and concrete by mineral carbonation." Current Opinion in Green and Sustainable Chemistry (2022): 100672.

[64] Ashraf W. "Carbonation of cement-based materials: Challenges and opportunities." Construction and Building Materials 120 (2016): 558-570.

[65] Papadakis V G, Vayenas C G, and Fardis M N. "A reaction engineering approach to the problem of concrete carbonation." AIChE Journal 35.10 (1989): 1639-1650.

[66] Black L, Breen C, Yarwood J, Garbev K, Stemmermann P, et al. "Structural features of C–S–H (I) and its carbonation in air—a Raman spectroscopic study. Part II: carbonated phases." Journal of the American Ceramic Society 90.3 (2007): 908-917.

[67] Dananjayan R R T, Kandasamy P, and Andimuthu R. "Direct mineral carbonation of coal fly ash for CO_2 sequestration." Journal of cleaner production 112 (2016): 4173-4182.

[68] Lo T Y, Tang W C, and Nadeem A. "Comparison of carbonation of lightweight concrete with normal weight concrete at similar strength levels." Construction and Building Materials 22.8 (2008): 1648-1655.

[69] Wang J, Xu H, Xu D, Du P, Zhou Z, et al. “Accelerated carbonation of hardened cement pastes: Influence of porosity.” Construction and Building Materials 225 (2019): 159-169.

[70] Ho D W S, and Lewis R K. “Carbonation of concrete and its prediction.” Cement and Concrete Research 17.3 (1987): 489-504.

[71] Cui H, Tang W, Liu W, Dong Z, and Xing F. “Experimental study on effects of CO2 concentrations on concrete carbonation and diffusion mechanisms.” Construction and Building Materials 93 (2015): 522-527.

[72] Rimmelé G, Barlet-Gouédard V, Porcherie O, Goffé B, and Brunet F. “Heterogeneous porosity distribution in Portland cement exposed to CO_2-rich fluids.” Cement and Concrete Research 38.8-9 (2008): 1038-1048.

[73] García-González C A, Hidalgo A, Andrade C, Alonso M C, Fraile, et al. “Modification of composition and microstructure of Portland cement pastes as a result of natural and supercritical carbonation procedures.” Industrial & engineering chemistry research 45.14 (2006): 4985-4992.

[74] Saillio M, Baroghel-Bouny V, Pradelle S, Bertin M, Vincent J, et al. “Effect of supplementary cementitious materials on carbonation of cement pastes.” Cement and Concrete Research 142 (2021): 106358.

[75] Han J, Liang Y, Sun W, Liu W, and Wang S. “Microstructure modification of carbonated cement paste with six kinds of modern microscopic instruments.” Journal of Materials in Civil Engineering 27.10 (2015): 04014262.

[76] Ngala V T, and Page C L. “Effects of carbonation on pore structure and diffusional properties of hydrated cement pastes.” Cement and concrete research 27.7 (1997): 995-1007.

[77] Collier N C. “Transition and decomposition temperatures of cement phases–a collection of thermal analysis data.” Ceramics-Silikaty 60.4 (2016).

[78] Durdziński P T, Dunant C F, Haha M B, and Scrivener K L. “A new quantification method based on SEM-EDS to assess fly ash composition and study the reaction of its individual components in hydrating cement paste.” Cement and Concrete Research 73 (2015): 111-122.

[79] Vargas P, Restrepo-Baena O, and Tobón J I. “Microstructural analysis of interfacial transition zone (ITZ) and its impact on the compressive strength of lightweight concretes.” Construction and Building Materials 137 (2017): 381-389.

[80] Mori D, and Yamada K. “A review of recent applications of EPMA to evaluate the durability of concrete.” Journal of Advanced Concrete Technology 5.3 (2007): 285-298.

[81] Mori D, Yamada K, Hosokawa Y, and Yamamoto M. “Applications of electron probe microanalyzer for measurement of Cl concentration profile in concrete.” Journal of Advanced Concrete Technology 4.3 (2006): 369-383.

[82] Grangeon S, Claret F, Lerouge C, Warmomt F, Sato T, et al. “On the nature of structural disorder in calcium silicate hydrates with a calcium/silicon ratio similar to tobermorite.” Cement and Concrete Research 52 (2013): 31-37.

[83] Haga K, Shibata M, Hironaga M, Tanaka S, and Nagasaki S. “Change in pore structure and composition of hardened cement paste during the process of dissolution.” Cement and Concrete Research 35.5 (2005): 943-950.

[84] Morgan I L, Ellinger H, Klinksiek R, and Thompson J N. “Examination of concrete by computerized

tomography.” Journal Proceedings. Vol. 77. No. 1. 1980.

[85] Vicente M A, González D C, Mínguez J, Tarifa M A, Ruiz G, et al. “Influence of the pore morphology of high strength concrete on its fatigue life.” International Journal of Fatigue 112 (2018): 106-116.

[86] Lu H, Peterson K, and Chernoloz O. “Measurement of entrained air-void parameters in Portland cement concrete using micro-X-ray computed tomography.” International Journal of Pavement Engineering 19.2 (2018): 109-121.

[87] Chae S R, Moon J, Yoon S, Bae S, Levitz P, et al. “Advanced nanoscale characterization of cement based materials using X-ray synchrotron radiation: a review.” International Journal of Concrete Structures and Materials 7.2 (2013): 95-110.

[88] Burlion N, Bernard D, and Chen D. “X-ray microtomography: Application to microstructure analysis of a cementitious material during leaching process.” Cement and Concrete research 36.2 (2006): 346-357.

[89] Xu K, Tremsin A S, Li J, Ushizima D M, Davy C A, et al. “Microstructure and water absorption of ancient concrete from Pompeii: An integrated synchrotron microtomography and neutron radiography characterization.” Cement and Concrete Research 139 (2021): 106282.

[90] Pavani H P, Tadepalli T, and Agarwal A K. “Estimation of porosity and pore distribution in Hydrated Portland cement at elevated temperatures using synchrotron micro tomography.” Journal of Advanced Concrete Technology 17.1 (2019): 34-45.

[91] Kim H T, Szilágyi V, Kis Z, Szentmiklósi L, Glinicki M A, et al. “Reconstruction of concrete microstructure using complementarity of X-ray and neutron tomography.” Cement and Concrete Research 148 (2021): 106540.

[92] Voltolini M, Marinoni N, and Mancini L. “Synchrotron X-ray computed microtomography investigation of a mortar affected by alkali–silica reaction: a quantitative characterization of its microstructural features.” Journal of materials science 46 (2011): 6633-6641.

[93] Scrivener K L, Füllmann T, Gallucci E, Walenta G, and Bermejo E. “Quantitative study of Portland cement hydration by X-ray diffraction/Rietveld analysis and independent methods.” Cement and Concrete Research 34.9 (2004): 1541-1547.

[94] Stutzman P E, Feng P, and Bullard J W. “Phase analysis of Portland cement by combined quantitative X-ray powder diffraction and scanning electron microscopy.” Journal of research of the National Institute of Standards and Technology 121 (2016): 47.

[95] Shaw S, Clark S M, and Henderson C M B. “Hydrothermal formation of the calcium silicate hydrates, tobermorite ($Ca_5Si_6O_{16}(OH)_2 \cdot 4H_2O$) and xonotlite ($Ca_6Si_6O_{17}(OH)_2$): an in-situ synchrotron study.” Chemical Geology 167.1-2 (2000): 129-140.

[96] Christensen A N, Jensen T R, and Hanson J C. “Formation of ettringite, $Ca_6Al_2(SO_4)_3(OH)_{12} \cdot 26H_2O$, AFt, and monosulfate, $Ca_4Al_2O_6(SO_4) \cdot 14H_2O$, AFm-14, in hydrothermal hydration of Portland cement and of calcium aluminum oxide-calcium sulfate dihydrate mixtures studied by in situ synchrotron X-ray powder diffraction.” Journal of solid state chemistry 177.6 (2004): 1944-1951.

[97] Claret F, Grangeon S, Loschetter A, Tournassat C, De Nolf W, et al. “Deciphering mineralogical changes and

carbonation development during hydration and ageing of a consolidated ternary blended cement paste." IUCrJ 5.2 (2018): 150-157.

[98] Rozière E, Loukili A, El Hachem R, and Grondin F. "Durability of concrete exposed to leaching and external sulphate attacks." Cement and Concrete Research 39.12 (2009): 1188-1198.

[99] Li L, Sagüés A A, and Poor N. "In situ leaching investigation of pH and nitrite concentration in concrete pore solution." Cement and Concrete Research 29.3 (1999): 315-321.

[100] Mackenzie F T, Duxbury A C, and Byrne R H. (2020). Seawater. Encyclopedia Britannica, 5.

[101] Sugiyama T, and Promentilla M A B. "Advancing Concrete Durability Research through X-ray Computed Tomography." Journal of Advanced Concrete Technology 19.6 (2021): 730-755.

[102] Bentz D P, Quenard D A, Kunzel H M, Baruchel J, Peyrin F, et al. "Microstructure and transport properties of porous building materials. II: Three-dimensional X-ray tomographic studies." Materials and Structures 33 (2000): 147-153.

[103] Hitomi T, Mita Y, Saito H, and Takeda N. "Observation of fine structure of mortar using X-ray CT images at SPring-8." Proceedings of Annual Conference of Japan Concrete Institute. Vol. 26. No. 1. 2004. (in Japanese)

[104] Helfen L, Dehn F, Mikulik P, and Baumbach T. "Three-dimensional imaging of cement microstructure evolution during hydration." Advances in Cement Research 17.3 (2005): 103-111.

[105] Gallucci E, Scrivener K, Groso A, Stampanoni M, and Margaritondo G. "3D experimental investigation of the microstructure of cement pastes using synchrotron X-ray microtomography (μCT)." Cement and Concrete Research 37.3 (2007): 360-368.

[106] Takahashi H, and Sugiyama T. "Application of non-destructive integrated CT-XRD method to investigate alteration of cementitious materials subjected to high temperature and pure water." Construction and building materials 203 (2019): 579-588.

[107] Takahashi H, and Sugiyama T. "Investigation of alteration in deteriorated mortar due to water attack using non-destructive integrated CT-XRD method." 11th fib International PhD Symposium in Civil Engineering, 2016. fib. The International Federation for Structural Concrete, 2016.

[108] Takahashi H. Study on the microscopic alteration of cementitious materials subjected to high temperature and water action using non-destructive integrated CT-XRD method. Diss. Hokkaido University, 2019.

[109] Kamitsubo H. "8 GeV synchrotron radiation facility project in Japan: JAERI-RIKEN spring-8 project." Nuclear Instruments and Methods in Physics Research Section A: Accelerators, Spectrometers, Detectors and Associated Equipment 303.3 (1991): 421-434.

[110] Sugiyama T, Hitomi T, and Kajiwara K. "Nondestructive integrated CT-XRD method for research on hydrated cement system." (2014).

[111] Thompson A C, Llacer J, Finman L C, Hughes E B, Otis J N, et al. "Computed tomography using synchrotron radiation." Nuclear Instruments and Methods in Physics Research 222.1-2 (1984): 319-323.

[112] Stock S R. "X-ray microtomography of materials." International materials reviews 44.4 (1999): 141-164.

[113] Hubbell J H, and Seltzer S M. Tables of X-ray mass attenuation coefficients and mass energy-absorption

coefficients 1 keV to 20 MeV for elements Z= 1 to 92 and 48 additional substances of dosimetric interest. No. PB-95-220539/XAB; NISTIR-5632. National Inst. of Standards and Technology-PL, Gaithersburg, MD (United States). Ionizing Radiation Div., 1995.

[114] Herman G T. Fundamentals of computerized tomography: image reconstruction from projections. Springer Science & Business Media, 2009.

[115] Promentilla M A B, Sugiyama T, Hitomi T, and Takeda N. "Characterizing the 3D pore structure of hardened cement paste with synchrotron microtomography." Journal of Advanced Concrete Technology 6.2 (2008): 273-286.

[116] Vincent L. "Morphological grayscale reconstruction in image analysis: applications and efficient algorithms." IEEE transactions on image processing 2.2 (1993): 176-201.

[117] Kohara S, Suzuya K, Kashihara Y, Matsumoto N, Umesaki N, et al. "A horizontal two-axis diffractometer for high-energy X-ray diffraction using synchrotron radiation on bending magnet beamline BL04B2 at SPring-8." Nuclear Instruments and Methods in Physics Research Section A: Accelerators, Spectrometers, Detectors and Associated Equipment 467 (2001): 1030-1033.

[118] Desgranges L, Grebille D, Calvarin G, Chevrier G, Floquet N, et al. "Hydrogen thermal motion in calcium hydroxide: $Ca(OH)_2$." Acta Crystallographica Section B: Structural Science 49.5 (1993): 812-817.

[119] Xiao J, Lv Z, Duan Z, and Zhang C. "Pore structure characteristics, modulation and its effect on concrete properties: A review." Construction and Building Materials 397 (2023): 132430.

[120] Iassonov P, Gebrenegus T, and Tuller M. "Segmentation of X-ray computed tomography images of porous materials: A crucial step for characterization and quantitative analysis of pore structures." Water resources research 45.9 (2009).

[121] Bentz D P, Mizell S, Satterfield S, Devaney J, George W, et al. (2002). "The visible cement data set." Journal of Research of the National Institute of Standards and Technology, 107, 137-148.

[122] Promentilla M A B, Sugiyama T, Hitomi T, and Takeda N. "Studies on pore structure characterization in hydrated cement system based on 3D micro-geometry technique." In: Proceedings of the JCI symposium on Durability Mechanism of Concrete Structures, Tokyo, Japan, Dec. 2007, 357-366.

[123] Hoshen J, and Kopelman R. "Percolation and cluster distribution. I. Cluster multiple labeling technique and critical concentration algorithm." Phys. Rev. B, (1976) 14, 34-38.

[124] Ikeda S, Nakano T, and Nakashima Y. (2000). "Three-dimensional study on the interconnection and shape of crystals in a graphic granite by X-ray CT and image analysis." Mineralogical Magazine, 64(5), 945-959.

[125] Fu J, Thomas H R, and Li C. "Tortuosity of porous media: Image analysis and physical simulation." Earth-Science Reviews 212 (2021): 103439.

[126] Shen L, and Chen Z. "Critical review of the impact of tortuosity on diffusion." Chemical Engineering Science 62.14 (2007): 3748-3755.

[127] Tjaden B, Brett D J L, and Shearing P R. "Tortuosity in electrochemical devices: a review of calculation approaches." International Materials Reviews 63.2 (2018): 47-67.

[128] Ghanbarian B, Hunt A G, Ewing R P, and Sahimi M. “Tortuosity in porous media: a critical review.” Soil science society of America journal 77.5 (2013): 1461-1477.

[129] Stauffer D, and Aharony A. Introduction to percolation theory. CRC press, 2018.

[130] Sugiyama T, Shimizu S, Ritthichauy W, and Tsuji Y. Determination of pore structure characteristic of mortar using a steady-state migration test. Journal of Materials, Concrete Structures and Pavements, Japan Society of Civil Engineers, 64 (767) (2004), pp. 227-238 (in Japanese)

[131] Nakashima Y, and Kamiya S. (2007). “Mathematica programs for the analysis of three-dimensional pore connectivity and anisotropic tortuosity of porous rocks using X-ray microtomography.” Journal of Nuclear Science and Technology, 44(9), 1233-1247.

[132] Codling E A, Plank M J, and Benhamou S. “Random walk models in biology.” Journal of the Royal society interface 5.25 (2008): 813-834.

[133] Sugiyama T, Promentilla M A B, Hitomi T, and Takeda N. “Application of synchrotron microtomography for pore structure characterization of deteriorated cementitious materials due to leaching.” Cement and Concrete Research 40.8 (2010): 1265-1270.

[134] Pearson K. “The problem of the random walk.” Nature 72.1865 (1905): 294-294.

[135] Kotani M, and Sunada T. “Spectral geometry of crystal lattices.” Contemporary Mathematics 338 (2003): 271-306.

[136] Tranter T G, Kok M D R, Lam M, and Gostick J T. “pytrax: A simple and efficient random walk implementation for calculating the directional tortuosity of images.” SoftwareX 10 (2019): 100277.

[137] Promentilla M A B, Sugiyama T, Hitomi T, Takeda N “Quantification of tortuosity in hardened cement pastes using synchrotron-based X-ray computed microtomography.” Cement and Concrete Research 39.6 (2009): 548-557.

[138] Ohkubo T. “Tortuosity based on anisotropic diffusion process in structured plate-like obstacles by Monte Carlo simulation.” Transport in porous media 72 (2008): 339-350.

[139] Sanjuán M A, Andrade C, and Cheyrezy M. “Concrete carbonation tests in natural and accelerated conditions.” Advances in Cement Research 15.4 (2003): 171-180.

[140] Galan I, Glasser F P, Baza D, and Andrade C. “Assessment of the protective effect of carbonation on portlandite crystals.” Cement and Concrete Research 74 (2015): 68-77.

[141] De Weerdt K, Justnes H, and Geiker M R. “Changes in the phase assemblage of concrete exposed to sea water.” Cement and Concrete Composites 47 (2014): 53-63.

[142] De Weerdt K, and Justnes H. “The effect of sea water on the phase assemblage of hydrated cement paste.” Cement and Concrete Composites 55 (2015): 215-222.

[143] Sun C, Chen J, Zhu J, Zhang M, and Ye J. “A new diffusion model of sulfate ions in concrete.” Construction and Building Materials 39 (2013): 39-45.

[144] Chen Y, Liu P, Zhang R, Hu Y, and Yu Z. “Chemical kinetic analysis of the activation energy of diffusion coefficient of sulfate ion in concrete.” Chemical Physics Letters 753 (2020): 137596.

[145] Perkins R B, and Palmer C D. “Solubility of ettringite ($Ca_6[Al(OH)_6]_2(SO_4)_3 \cdot 26H_2O$) at 5–75°C.” Geochimica et Cosmochimica Acta 63.13-14 (1999): 1969-1980.

[146] Buenfeld N R, and Newman J B. “The development and stability of surface layers on concrete exposed to sea-water.” Cement and Concrete Research 16.5 (1986): 721-732.

[147] Kurdowski W. “The protective layer and decalcification of CSH in the mechanism of chloride corrosion of cement paste.” Cement and Concrete Research 34.9 (2004): 1555-1559.

[148] Brett N H. “An X-ray investigation of the thermal decomposition of portlandite.” Mineralogical Magazine 37.286 (1969): 244-249.

[149] Choi Y S, and Yang E I. “Effect of calcium leaching on the pore structure, strength, and chloride penetration resistance in concrete specimens.” Nuclear Engineering and Design 259 (2013): 126-136.

[150] Basheer L, Kropp J, and Cleland D J. (2001). Assessment of the durability of concrete from its permeation properties: a review. Construction and building materials, 15(2-3), 93-103.

[151] Bernard F, and Kamali-Bernard S. “Numerical study of ITZ contribution on mechanical behavior and diffusivity of mortars.” Computational Materials Science 102 (2015): 250-257.

[152] Sun G, Zhang Y, Sun W, Liu Z, and Wang C. “Multi-scale prediction of the effective chloride diffusion coefficient of concrete.” Construction and Building Materials 25.10 (2011): 3820-3831.

[153] Zheng J J, and Zhou X Z. “Prediction of the chloride diffusion coefficient of concrete.” Materials and Structures 40 (2007): 693-701.

[154] Caré S. “Influence of aggregates on chloride diffusion coefficient into mortar.” Cement and Concrete Research 33.7 (2003): 1021-1028.

[155] Wu K, Han H, Li H, Dong B, Liu T, et al. “Experimental study on concurrent factors influencing the ITZ effect on mass transport in concrete.” Cement and Concrete Composites 123 (2021): 104215.

[156] Latour L L, Mitra P P, Kleinberg R L, and Sotak C H. “Time-dependent diffusion coefficient of fluids in porous media as a probe of surface-to-volume ratio.” Journal of Magnetic Resonance, Series A 101.3 (1993): 342-346.

[157] Ribeiro A C F, Barros M C F, Teles A S N, Valente A J M, Lobo V M M, et al. “Diffusion coefficients and electrical conductivities for calcium chloride aqueous solutions at 298.15 K and 310.15 K.” Electrochimica Acta 54.2 (2008): 192-196.

[158] Ollivier J P, Maso J C, and Bourdette B. “Interfacial transition zone in concrete.” Advanced cement based materials 2.1 (1995): 30-38.

[159] Maleki M, Rasoolan I, Khajehdezfuly A, and Jivkov A P. “On the effect of ITZ thickness in meso-scale models of concrete.” Construction and Building Materials 258 (2020): 119639.

[160] Hasebe H, Chimoto A, and Sugiyama T. “Evaluation of Interfacial Transition Zone in Concrete by Synchrotron Radiation Microtomography”, Proceedings of the 6th International Conference on Construction Materials (ConMat’20), pp.755-765, sept. 2020

[161] Saito H, Tsuji Y, and Kataoka H. “A Model for Predicting the Leaching Degradation of Cement Hydrate”

Concrete Research and Technology, 11.1 (2000): 51-59. (In Japanese)

[162] Nakarai K, Ishida T, Maekawa K, and Nakane S. “Calcium leaching modeling of strong coherency with micropore formation of porous media and ion phase equilibrium.” Doboku Gakkai Ronbunshu 69 (2005). (In Japanese)

[163] Takashi H, Takeda N, and Iriya K. “Calculation of calcium diffusion coefficient of cement hardenings using minute pore data.” Obayashi-Gumi Gijutsu Kenkyusho-Ho (2009). (In Japanese)

[164] Sugiyama T, Ritthichauy W, and Tsuji Y. “Simultaneous transport of chloride and calcium ions in hydrated cement systems.” Journal of Advanced Concrete Technology 1.2 (2003): 127-138.

[165] Sugiyama, T., Ritthichauy W, and Y. Tsuji. “Experimental investigation and numerical modeling of chloride penetration and calcium dissolution in saturated concrete.” Cement and Concrete Research 38.1 (2008): 49-67.

[166] Tang L. “Concentration dependence of diffusion and migration of chloride ions: Part 2. Experimental evaluations.” Cement and Concrete Research 29.9 (1999): 1469-1474.

[167] Bentz D P, Garboczi E J, and Lagergren E S. “Multi-scale microstructural modeling of concrete diffusivity: Identification of significant variables.” Cement Concrete and Aggregates, 20 (1998), 129-139.

[168] Yang C C, and Su J K. “Approximate migration coefficient of interfacial transition zone and the effect of aggregate content on the migration coefficient of mortar.” Cement and Concrete Research, 32(10) (2002), 1559-1565.

[169] Matyka M, Khalili A, and Koza Z. “Tortuosity-porosity relation in porous media flow.” Physical Review E 78.2 (2008): 026306.

[170] Johnston H M, and Wilmot D J. “Sorption and diffusion studies in cementitious grouts.” Waste Management 12.2-3 (1992): 289-297.

[171] Mitra P P, Sen P N, and Schwartz L M. “Short-time behavior of the diffusion coefficient as a geometrical probe of porous media.” Physical Review B 47.14 (1993): 8565.

[172] Wang G, Shen J, Liu S, Jiang C, and Qin X. “Three-dimensional modeling and analysis of macro-pore structure of coal using combined X-ray CT imaging and fractal theory.” International Journal of Rock Mechanics and Mining Sciences 123 (2019): 104082.

[173] Fu J, and Yu Y. “Experimental study on pore characteristics and fractal dimension calculation of pore structure of aerated concrete block.” Advances in Civil Engineering 2019 (2019).

Appendix A: INTERFERENCE CAUSED BY FIXED METHOD

In CT scanning, the specimen needs to be fixed on the stage and remain stable during the scanning process. To achieve this goal, we had tried two kinds of fixation methods during experiment. The first one is to wrap the specimen with the single-sided aluminum tape, then stuff it into the metal container, and finally place the metal container on the stage, as shown in Figure A-1. This method can fix the position and posture of the specimen in a more consistent way, which eliminates the need to adjust the position of specimen and avoids the tilt of specimen. Figure A-2 shows the CT image under the first fixation method (S6N28d). In which, the fixed structure (metal container and aluminum tape) can be clearly observed.

However, this fixation method brings certain interference in XRD measurement. Using this method will introduce interference from the aluminum tape when performing XRD measurements on the outer edge of the specimen. Figure A-3 shows point 1 and point 2 XRD data for S6N28d specimen. In which point 1 near edge of specimen while point 2 inside the specimen. XRD data of point 1 shows signal from aluminum, which obviously can only come from interference from the fixed structure (aluminum tape).

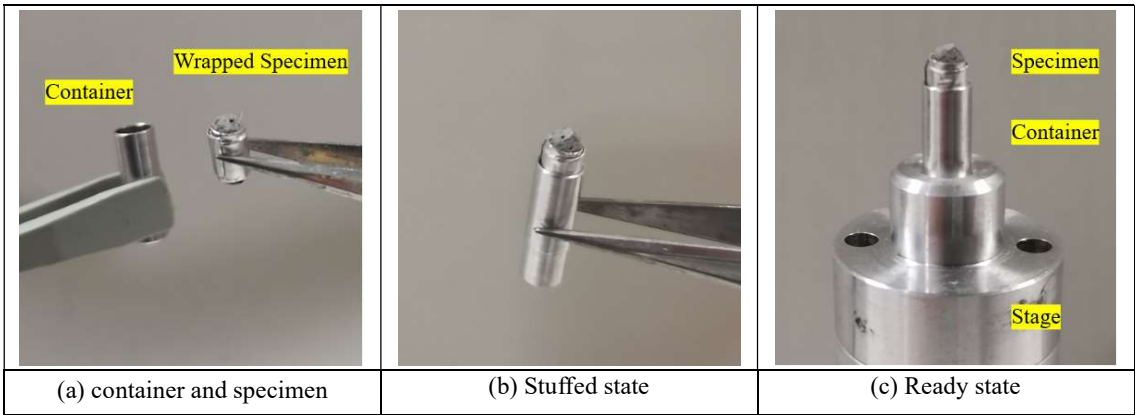

(a) container and specimen	(b) Stuffed state	(c) Ready state

Figure A-1 The first fixation method

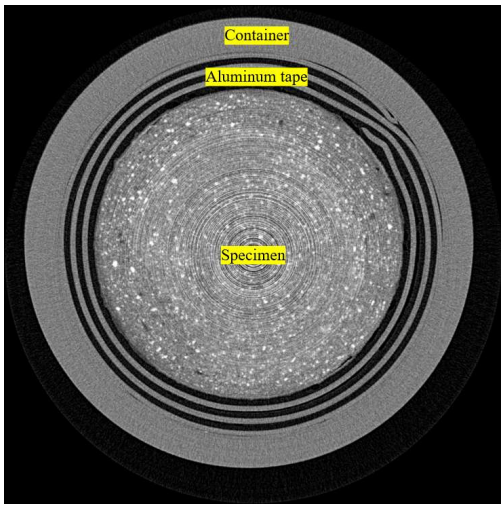

Figure A-2 CT image under the first fixation method (S6N28d, layer:0720)

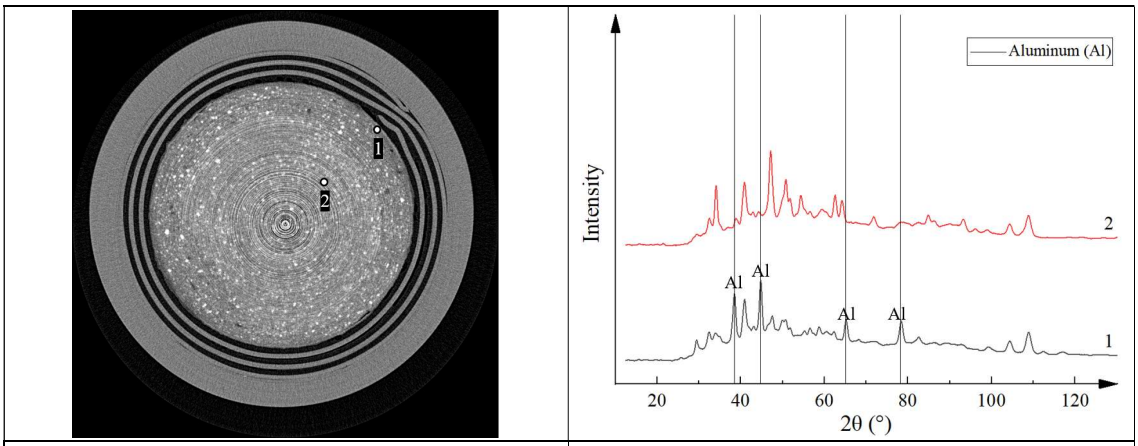

(a) Position of XRD data point (b) XRD data

Figure A-3 CT image under the first fixation method (S6N28d, layer:0720)

For some specimens, it is important to detect the phase composition at the outer edge of specimen, so it is necessary to eliminate this interference. The second fixation method used in this research is to paste the acrylic plate on the stage with glue, and then paste the specimen on the acrylic plate with the double-sided tape, as shown in Figure A-4. This fixation method increases the workload and inevitably leads to the possibility of specimen tilt, but it does eliminate interference signals. Figure A-5 shows point 1 and point 2 XRD data for S6N154d specimen. In which point 1 near edge of specimen while point 2 inside the specimen. XRD data of point 1 no longer shows interference signal from aluminum.

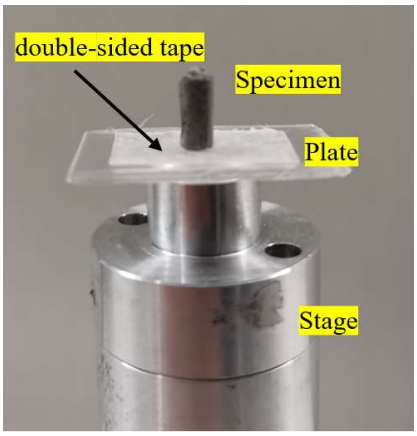

Figure A-4 The second fixation method

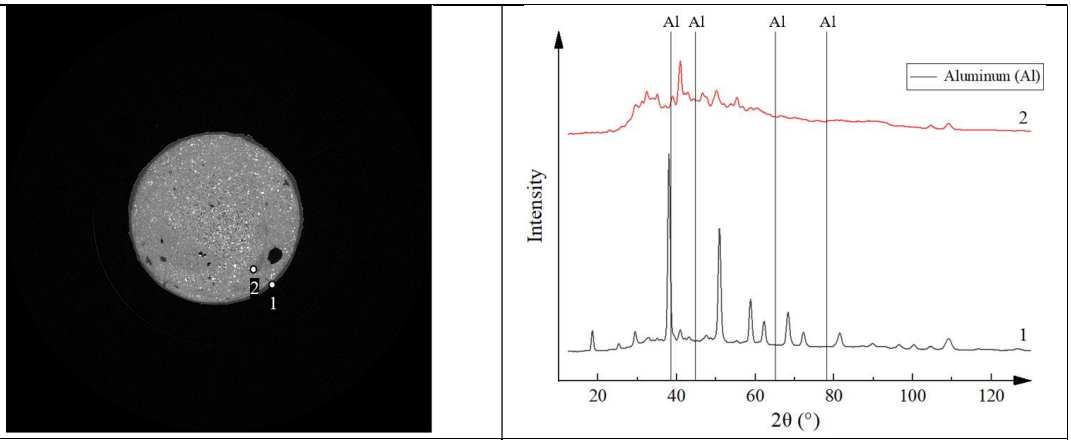

(a) Position of XRD data point | (b) XRD data

Figure A-5 CT image under the second fixation method (S6N154d, layer:0600)

Appendix B: IMPROVEMENTS OF IMAGE QUALITY

The reconstruction algorithm used in this research was improved for ring artifacts. A reconstruction algorithm is a mathematical method used to convert the acquired raw data into cross-sectional images of the scanned specimen. While a ring artifact in a CT image is a type of image distortion or artifact that appears as a circular or ring-shaped pattern in the reconstructed image. Ring artifact may result from malfunctioning of detector elements, inadequate calibration, or movement of specimen during scanning. Figure B-1 shows the artifact on the CT image of 6C120d specimen.

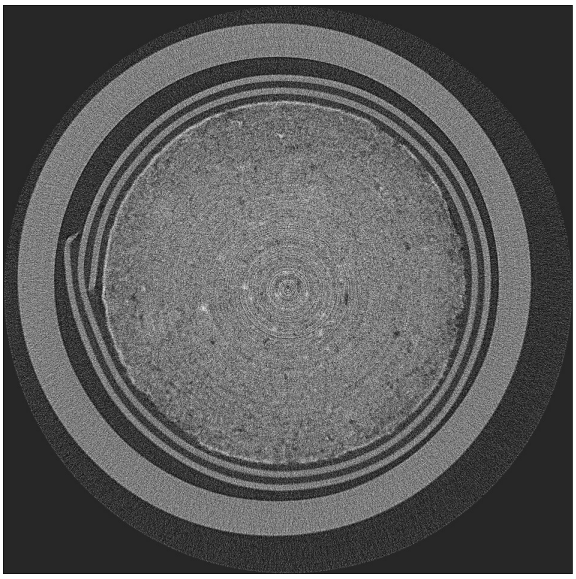

Figure B-1 Ring artifact showing on the CT image (6C120d)

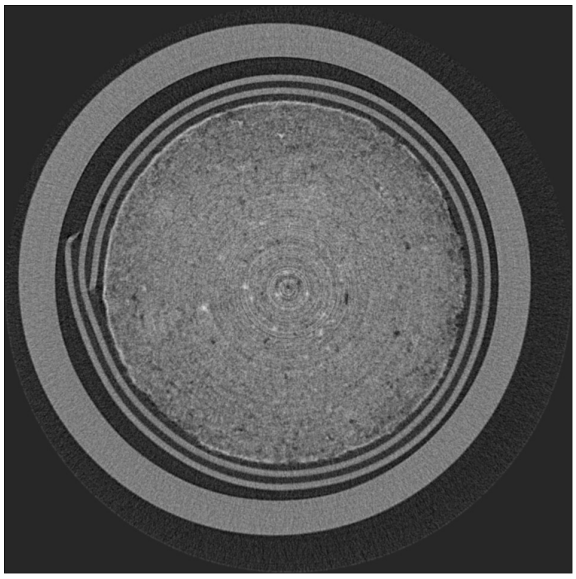

Figure B-2 Ring artifact and filtering process (Gaussian filtering. Sig=2.0)

Ring artifacts adversely affect the extraction of pore structure and will also affect subsequent analysis. It is necessary to eliminate effect of ring artifacts. However, ring artifacts is not a random noise, or white noise, so it cannot be eliminated by conventional filtering methods, as shown on Figure B-2. Ring artifacts appear differently as vertical lines on the sinogram depending on their characteristics. A continuous single ring artifact will appear as a continuous vertical line on the sinogram, single ring artifact with varying brightness will appear as vertical lines with varying brightness on the sinogram. According to this feature, we can make targeted adjustments to the sinogram to effectively eliminate ring artifacts. Figure B-3 shows CT image obtained from improved reconstruction method. In which, it can be seen that ring artifacts is eliminated.

Figure B-3 CT image obtained from improved reconstruction method